Growth and Spectroscopy of Ytterbium-Doped Sesquioxides

Dissertation

zur Erlangung des Doktorgrades
des Fachbereichs Physik
der Universität Hamburg

vorgelegt von
Volker Peters
aus Hamburg

Hamburg
2001

Abstract

V. Peters, *Growth and Spectroscopy of Ytterbium-Doped Sesquioxides*

The high-melting sesquioxides of scandium, yttrium, and lutetium are interesting laser host-materials because of their high thermal conductivity, strong Stark-splitting, and low phonon energies. Laser operation of sesquioxide crystals doped with various rare-earths has been demonstrated. Especially sesquioxides doped with trivalent ytterbium have shown very promising results in first high-power laser experiments.

In the course of this work several known crystal growth methods were optimized for the growth of bulk sesquioxide crystals. The heat-exchanger-method was adapted for the use at the high melting temperatures to be able to obtain larger single crystals of higher optical quality than with the growth methods used in the past. Scandia single crystals of several cubic centimeters in volume could be grown in first experiments by this method.

Sesquioxide crystals doped with various rare-earths as well as non-doped crystals were spectroscopically analyzed. Special emphasis was set on the identification of the electronic level structure of trivalent ytterbium in the two crystallographic symmetry sites C_2 and C_{3i}. Due to the strong electron-phonon coupling in ytterbium an unambiguous identification of electronic and vibronic levels by standard low temperature spectroscopy is not successful.

Measurements at high hydrostatic pressures of several GPa were used in a first attempt to distinguish between electronic and vibronic levels. This is possible since the phonons of the host lattice generally show a different reaction to pressure than the electronic levels. The experimentally observed line shifts, however, were not sufficient to make this distinction.

The study of exchange-coupled ytterbium pair-states proved more successful. Due to the reduced electron-phonon coupling for pair-transitions, measurements of the pair-absorption and -emission in the green spectral region allowed a clear determination of the electronic structure for ions in both symmetry sites. Since the cross-sections of the pair-transitions are very low, the spectra of various other rare-earths were measured to exclude transitions from rare-earths that appear as unwanted impurities in the raw chemicals.

Zusammenfassung

V. Peters, *Growth and Spectroscopy of Ytterbium-Doped Sesquioxides*

Die hochschmelzenden Sesquioxide des Scandiums, Yttriums und Lutetiums sind aufgrund ihrer hohen Wärmeleitfähigkeit, der großen Stark-Aufspaltung und ihrer geringen Phononenenergien als Wirtsmaterialien für Laserkristalle von Interesse. Laserbetrieb konnte in den Sesquioxiden mit zahlreichen Selten-Erd Dotierungen erzielt werden. Insbesondere dreiwertiges Ytterbium als Dotierung hat in ersten Hochleistungs-Laserversuchen äußerst vielversprechende Resultate gezeigt.

Im Rahmen dieser Arbeit wurden bekannte Kristallzuchtmethoden für die Zucht der hochschmelzenden Sesquioxide optimiert. Das HEM-Verfahren (Heat-Exchanger-Method) wurde an die hohen Schmelztemperaturen der Sesquioxide angepaßt, um die Herstellung größerer Einkristalle von höherer optischer Qualität als mit den bisher getesteten Methoden zu ermöglich. In ersten Zuchtversuchen konnten Scandiumoxid Einkristalle von mehreren Kubikzentimetern Volumen hergestellt werden.

Es wurden spektroskopische Analysen von Sesquioxiden mit verschiedenen Selten-Erd Dotierungen vorgenommen. Besonderer Wert wurde auf die Identifikation der elektronischen Niveaus des dreiwertigen Ytterbiums auf den beiden kristallographischen Plätzen mit C_2- und C_{3i}-Symmetrie gelegt. Die eindeutige Unterscheidung zwischen elektronischen und vibronischen Niveaus mit herkömmlicher Tieftemperatur-Spektroskopie ist bei Ytterbium aufgrund der starken Elektron-Phonon-Kopplung nicht möglich.

Zunächst wurde versucht mit Messungen bei hohen hydrostatischen Drücken im GPa Bereich zwischen elektronischen und vibronischen Niveaus zu unterscheiden. Dies ist prinzipiell möglich, da die Phononen des Wirtsgitters im allgemeinen anders auf Druck reagieren als die elektronischen Niveaus. Die beobachteten Linienverschiebungen reichten allerdings nicht aus, um eine Unterscheidung zu ermöglichen.

Erfolgreicher waren Messungen an Ytterbium-Paaren, die über Austausch-Wechselwirkung gekoppelt sind. Aufgrund der geringeren Elektron-Phonon-Kopplung bei Paarübergängen ermöglichten Messungen der Paar-Absorption und -Emission im grünen Spektralbereich eine eindeutige Bestimmung der Energieniveaus von Ionen auf beiden Kationenplätzen. Da die Übergänge zwischen Paar-Niveaus sehr schwach sind, wurden zahlreiche andere Selten-Erd Dotierungen vermessen, um Übergänge anderer Materialien, die als Verunreinigungen in den Ausgangsmaterialien vorkommen, ausschließen zu können.

Contents

Used Symbols and Abbreviations

Constants

a_0	Bohr radius
ϵ_0	Vacuum permittivity
c	Speed of light in a medium
c_0	Vacuum speed of light
e	Elementary charge
h	Planck constant
$\hbar$	$= h/2\pi$ Planck constant
k	Boltzmann constant
m_e	Electron mass

Variables

α	Absorption coefficient
β_{ij}	Branching ratio of an excited-state
ΔE	Various energy differences
ΔE_{phon}	Total $4f$-linewidth
ΔE^D	Single-phonon broadening of the $4f$-linewidth
ΔE^R	Raman broadening of the $4f$-linewidth
ΔE^{Orb}	Orbach broadening of the $4f$-linewidth
ΔE^{MR}	Multi-phonon-relaxation broadening of the $4f$-linewidth
ΔE^{Rad}	Natural $4f$-linewidth
ϵ	Emissivity
η	Slope efficiency of a laser
θ	Curie-Weiss temperature

ϑ_j	Spherical coordinate
κ	Isothermal compressibility
λ	Wavelength
μ_{ij}	Dipole-matrix-element
ν	Frequency
ξ	Phonon branch
σ_{abs}	Effective absorption cross-section
σ_{at}	Atomic transition cross-section
σ_{se}	Effective stimulated emission cross-section
σ_{ij}	Transition cross-section for $\lvert j \rangle \rightarrow \lvert i \rangle$
τ	Fluorescence lifetime
τ_{nr}	Non-radiative lifetime
τ_{rad}	Radiative lifetime
ϕ	Wave-function
φ_j	Spherical coordinate
Ψ_0	Wave-function of an ion in the central-field-approximation
$\hbar\omega_{\text{eff}}$	Effective phonon-enenergy
a	Strength of the electron-phonon-coupling
A	Normalizing factor
a, a^t	Construction and destruction operator of a phonon
A_{ij}	Einstein coefficient of spontaneous emission
B	Normalizing factor
B_{ij}	Einstein coefficient of stimulated emission
B_{ji}	Einstein coefficient of absorption
B_q^k	Adjustable parameters in crystal-field calculations
$\bar{B}_k$	Distance dependent crystal-field parameter
C_{DA}	Micro-parameter for donor-acceptor transfer
C_{DD}	Micro-parameter for donor-donor transfer
C_{FL}	Adjustment constant of the Füchtbauer-Ladenburg equation
C_i	Eigenfunctions for Hartree-Fock-method
$C_q^{(k)}$	Crystal-field tensor
d	Crystal thickness
d_n	Distance between two cations with respect to the coordination sphere
E_0	Energy-eigenvalue of an ionic state
E_I, E_{II}	Energy-levels of two exchange-coupled ions
E_i	Various energies
$f_{abs/em}$	Normalized line-shapes of the absorption- and emission-line
f_k	Boltzmann-factor of the state $\lvert k \rangle$
g_i	Degeneracy level of the state i

H_{12}	Hamiltonian for H_2
H_0	Hamiltonian in the central-field approximation
H_{ee}	Perturbation term for H_0; non radial-symmetric portion of the electron-electron interaction
H_{el-ph}	Perturbation term for H_0; electron-phonon interaction
H_{ex}	Exchange Hamiltonian
H_{so}	Perturbation term for H_0; spin-orbit-coupling
H_{cf}	Perturbation term for H_0; crystal-field
I	Various intensities
J	Total angular momentum quantum number
$\bar{J}$	Average exchange integral
J_{ij}	Exchange integral of i and j
j_i	Angular momentum quantum number of the ith electron
$\mathbf{j_i}$	Angular momentum vector of the ith electron
K_{12}	Average Coulomb interaction energy of H_2
K_{kq}	Geometrical factor of the crystal-field
L	Total orbital angular momentum quantum number
l_i	Orbital angular momentum quantum number of the ith electron
$\mathbf{l_i}$	Orbital angular momentum vector of the ith electron
m	Reduced mass of an atom
M_J	Magnetic quantum number of an ion $M_J = -J, -J + 1, ..., +J$
m_l	Magnetic quantum number of an electron $m_l = -l, -l + 1, ..., +l$
M_L	Magnetic quantum number of an ion $M_L = -L, -L + 1, ..., +L$
m_s	Spin quantum number $m_s = -\frac{1}{2}, +\frac{1}{2}$
M_S	Total spin quantum number of an ion $M_S = -S, -S + 1, ..., +S$
N	Number of electrons of an ion
$\mathbf{n}$	Number of a coordination sphere
n	Refractive index
n_d	Dopant concentration
n_i	principal quantum number of the ith electron
N_i	Population density of the state i
p	number of phonons needed for a non-radiative transition
P	Pressure
P_{abs}	Absorbed pump-power
P_{out}	Laser output-power

P_{4f}	Hartree-Fock wave function of a $4f$-state
$\mathbf{q}$	Wave-vector of a phonon
r_x	Various distances
$\mathbf{r}_x$	Various relative positions
$\mathbf{r_i}$	Position of the ith electron relative to the nucleus
R_{DA}	Donor-acceptor-distance
R_j	Distance of an ion to its ligand
R^L	Distance between ion and ligand
R_0^L	Reference distance for R^L
S	Total spin quantum number
$\mathbf{s_i}$	Spin-vector of the ith electron
t	Time
T	Various temperatures in Kelvin
t_k^L	Exponent of the distance dependence of $\bar{B}_k^L$
T_N	Neel-temperature
V	Volume
$V(x)$	Various potential energies
W_0	Empirical factor of W_{nr}
W_{DA}	Interionic transition-probability
$W_{a,n}$	Probability to find a ions in the nth coordination shell
W_p	Probability that an ion has at least one next neighbor of the same type
W_{nr}	Non-radiative relaxation-rate
Z	Atomic number
Z_i	Exponential parameters for Hartree-Fock-method
z_j	Coordination number for neighbor type j
$\mathbf{z}_n$	Coordination number for pairs types with respect to the coordination sphere n
Z_{multi}	Partition function of a manifold

Abbreviations

cw	Continuous wave
ESA	Excited state absorption
GSA	Ground state absorption
HEM	Heat-exchanger-method;
IOB	Intrinsic optical bistability;
LHPG	Laser-heated-pedestal-growth;
RE	Rare-earth;
SE	Stimulated emission

TM	Transition metal
YAG	Yttrium-Aluminum-Garnet; $Y_3Al_5O_{12}$
YbAG	Ytterbium-Aluminum-Garnet; $Yb_3Al_5O_{12}$
YLF	Yttrium-Lithium-Fluoride; $YLiF_4$
ZL	Zero-line; lowest energy electronic line of a manifold

1

Introduction

Trivalent ytterbium is known as a laser-active ion since 1965 [joh65]. However, its potential could not be fully utilized at the time due to the low pumping efficiency of ytterbium ions when using flashlamps. Over the past years a rising interest in ytterbium-doped systems can be noted. This can be mostly attributed to the rising availability and quality of laser diodes in the 900 - 940 nm wavelength range.

Trivalent ytterbium combines some unique spectroscopic and laser properties. It has only two manifolds within the bandgap of most dielectric crystals or glasses separated by approximately 10.000 cm^{-1}. This is interesting for the field of laser physics since the most effective loss processes like excited state absorption, upconversion, and cross-relaxation do not exist and multi-phonon relaxation is highly unlikely in an ideal ytterbium system. Furthermore the quantum defect of the main emission between 1010 and 1100 nm is very low due to the quasi-four-level scheme and the comparatively broad absorption lines are well suited for pumping with laser diodes. However in real crystals and glasses the presence of impurities can cause severe problems due to the fact that ytterbium can transfer its excitation energy excellently to many rare-earths and transition-metals [bol01]. Also the quasi-four-level scheme causes problems since the lower laser level is thermally populated and the laser reacts strongly to heating of the active channel.

From a spectroscopic point of view the seemingly simple energy level structure allows observation of weak effects, like pair transitions, that would be covered by other, much stronger electronic transitions in most ions. Also ytterbium has the strongest electron-phonon coupling of the rare-earths which allows a good observation of phonon-induced effects but on the other hand can make a clear determination of the actual electronic structure of the system very complicated. As already mentioned above it is very interesting for the study of energy-transfer pro-

cesses since only transfers from the one excited ytterbium manifold are possible.

The main application of ytterbium-doped laser systems today is in the field of materials processing. Yb:YAG lasers with cw[1]-output powers of several hundred Watts can be manufactured and are slowly replacing Nd:YAG systems for cutting, drilling, welding, and heat treatments of metals. The use of cw and quasi-cw lasers is, however, limited in terms of working precision. Therefore, there is also a great interest especially from the automotive industry to have high power mode-locked laser systems with pulse lengths in the picosecond to 100 fs regime. This will allow a substantially enhanced working precision, thus enhancing quality and cutting post-processing costs. Due to its broad emission lines ytterbium lasers are able to produce such short pulses. This, combined with the ability to use efficient diode pumping, has further strengthened the interest in ytterbium lasers in the past few years.

A highly important point for the design of ytterbium high-power lasers is the careful choice of the laser host material. Due to the sensitivity towards heating of the system, the thermal conductivity of the laser material should be as high as possible. Also the splitting of the energy levels should be large since this reduces the thermal population of the lower laser level. The sesquioxides of scandium, yttrium, and lutetium meet these requirements; all three, but especially scandia, have a strong crystal field and therefore a large Stark-splitting and exhibit thermal conductivities that are, in the case of ytterbium-doped lutetia, nearly twice as high as that of Yb:YAG. Another point, which is especially important for the use with the successful thin-disk-laser concept [gie94], is the high possible ytterbium-dopant concentration of lutetia. Due to the small difference in the ionic radii the distribution coefficient of ytterbium in lutetia is near unity. This allows the use of very thin, highly doped crystal disks that still absorb a high percentage of the pump energy. First tests with Yb:Sc$_2$O$_3$ and Yb:Lu$_2$O$_3$ have shown very promising results with 124 W of output power at 250 W pump power in the case of scandia and 23 W for 54 W of pump power with lutetia. Furthermore the sesquioxides are interesting for the study of strongly proximity dependent effects, such as pair transitions or energy transfer processes, due to their low interionic distances and high cation densities.

The production of high quality bulk samples of these sesquioxides, however, is complicated by the high melting temperatures of these materials in the range above 2400 C. Established growth methods for high quality oxide crystals such as the Czochralski- or Bridgman-method could only be used up to 2050 C until a few years ago and methods for high temperature crystal growth, such as the Verneuil-, floating-zone-, or skull-melting-method, yield either small single crystals or low optical quality. Until very recently the success in growing the high

---

[1]continuous wave

melting sesquioxides was limited to single crystals of 1 cm^3 volume and moderate optical quality.

One aim of this work was to establish a growth method that would allow the reproducible production of large scale, high quality sesquioxide crystals. For this purpose the heat-exchanger-method was adapted for use at the melting temperatures of the sesquioxides above 2400 C. Secondly intensive spectroscopic research has been carried out with ytterbium-doped sesquioxides in order to securely identify the energy level scheme of the ytterbium ion and to gain some initial insight in Yb-dimer effects, which are exceptionally strong in the sesquioxides due to the small interionic distances and the high achievable dopant concentrations.

This introduction is followed by a description of the crystallographic and physical properties of the sesquioxides. Chapter 3 gives an overview on the growth of sesquioxide crystals including the newly tested growth methods and an evaluation of the obtained crystal qualities. The next two chapters address some theoretical and technical aspects that are necessary for understanding the spectroscopic investigations in chapter 6. Chapter 7 presents the thin-disk-laser experiments and simulations that were performed at the Institut für Strahlwerkzeuge in Stuttgart using ytterbium-doped sesquioxides and the values of the identified electronic levels.

2

Yttria, Scandia, Ytterbia, and Lutetia

The physical properties of the sesquioxides have been subject to numerous studies since the early sixties. Some crystallographic studies go back as far as 1928 [zac28, pau30]. Due to various inconsistencies between different literary sources, additional measurements with newly grown sesquioxide crystals were necessary to reach clarity in ambiguous cases and establish not yet published properties.

In this chapter the material properties important for this work are presented. Additional data can be found in the theses of E. Mix and L. Fornasiero [mix99, for99]. A summary of the most essential values is given in table 2.1.

2.1 Crystallographic Properties

The sesquioxides can occur in several crystallographic structures depending on the cation radius, the temperature, or pressure [hoe66, rot60, pie74]. At room temperature the sesquioxides of scandium, yttrium, ytterbium, and lutetium form a cubic C-type structure, also known as bixbyite. This structure is stable up to the melting point except for yttria, which changes to a hexagonal high-temperature phase slightly below the melting point. A phase transition to the monoclinic B-type structure occurs at high pressures of 25 kbar in the case of Y_2O_3, 40 kbar for Lu_2O_3, and 130 kbar at 1000 C for Sc_2O_3 [pie74].

The bixbyite structure belongs to the space group $Ia\bar{3}$ (T_7^h) [pau30] (see figure 2.1). The unit cell contains 16 formula units with 32 cations. The lattice constant is in the range of 10 Å depending on the cation; the cation densities of around

	Sc_2O_3	Y_2O_3	Yb_2O_3	Lu_2O_3	YAG
dopants[1]	RE, TM	RE, TM	RE, TM	RE,TM	RE, TM
melting point [C]	≈2430	2430	≈2430	≈2450	1930
lattice	cubic	cubic	cubic	cubic	cubic
space group	T_h^7	T_h^7	T_h^7	T_h^7	O_h^{10}
site symmetries	C_2, C_{3i}	C_2, C_{3i}	C_2, C_{3i}	C_2, C_{3i}	D_2, C_{3i}, S_4
coordination numbers	6	6	6	6	8; 6; 4
density of RE-cation sites [10^{20} cm^{-3}]	335.5	268.7	281.3	285.2	138
lattice constant [Å][2]	9.844 9.857	10.603 10.602	10.439 10.433	10.391	12.00
eff. ion-radius of the ion replaced by RE-dopant [Å]	0.75	0.90	0.87	0.86	1.02
transparency range [µm]	0.22-8	0.23-8	0.26-?	0.23-?	0.18-6
refractive index @ 1050 nm	1.965	1.89	-	1.91	1.815
eff. phonon energy for RE-dopants [cm^{-1}]	<625[3]	430	-	<430	700
thermal conductivity non-doped (at 30 C) [$\frac{W}{mK}$]	16.5	13.6	-	12.5	11.0
doped with 3% Yb (at 30 C)	6.6	7.7	-	11.0	6.8
Mohs-hardness	<6.8	6.8	-	≈7	8.5

Table 2.1: Material properties of the sesquioxides in comparison to YAG [kam90, pie74, nig67, mcd66, lis98, lis98b, hoh99, web82, bar57, hur68, win81]

3×10^{22} cm^{-3} are very high compared to many other compound crystals (see table 2.1). Scandia has the highest cation density of the examined oxides followed by lutetia and ytterbia. Yttria has the lowest cation density.

The bixbyite structure contains two cation symmetry sites, both coordinated six-fold with oxygen. A unit cell contains 24 sites of C_2-symmetry and 8 sites of C_{3i}-symmetry (see figure 2.1(b)). The two-fold axes of the C_2 sites are oriented parallel to the [100] directions, the three-fold axes of the C_{3i} sites are parallel to [111]. Furthermore the crystals have a cleavage plane parallel to the {111} - plane [sch70b].

The atomic positions for yttria are given in table 2.2. The values given here differ from those in the original publication by Pauli [pau30] due to some changes made to the International Tables of Crystallography in 1952. The original values applied to the symmetry operations in modern issues of the International Tables create a slightly different structure. It has to be noted that some articles published in the past (e. g. [koe71]) used this incorrect structure for calculations which led

---

[1]RE: rare-earths; TM: transition metals

[2]different values can be found in literature
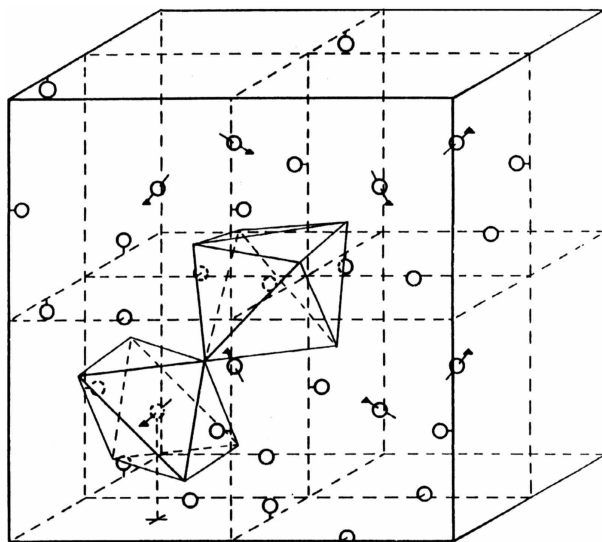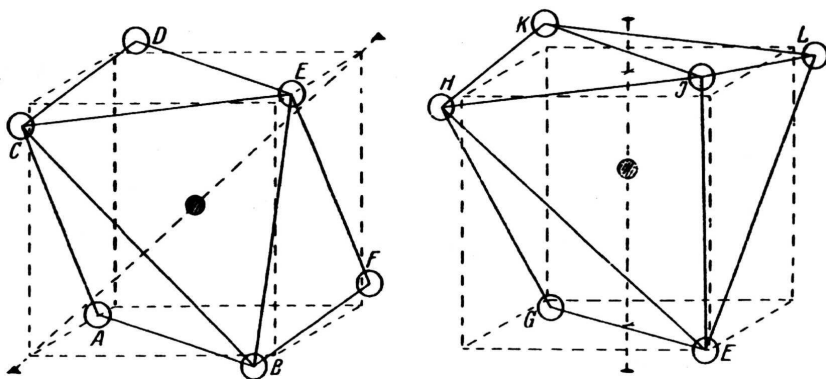
[3]estimated from infrared-absorption-spectra [mcd66]

(a) Unit cell; C_2: ○, C_{3i}: ⚡

(b) The two cation-sites; left: C_{3i}, right: C_2

Figure 2.1: Crystallographic structure of Bixbyit [pau30]
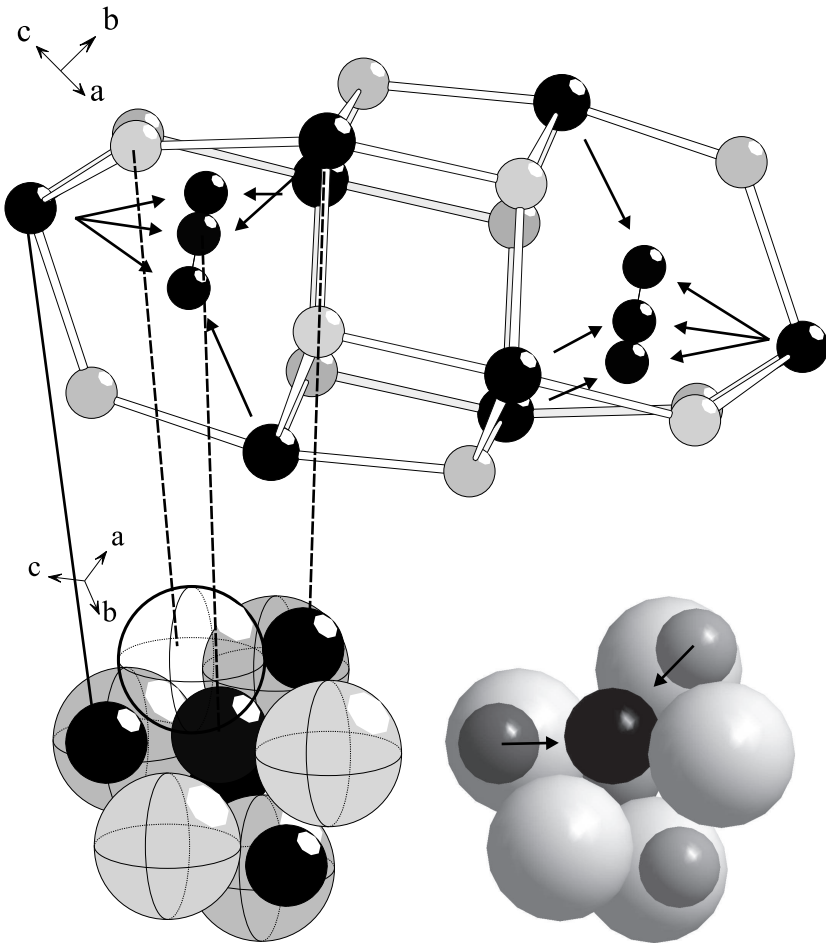
Figure 2.2: Top: Partial view of the unit cell of Er(0.4%):Sc$_2$O$_3$ viewed along to the [101] - axis. The arrows indicate the possible shifts of the erbium ions from the scandium-sites. Bottom: Position of one shifted erbium-ion in the interstitial lattice site viewed along [1$\bar{1}$1]. The oxygen vacancy near the erbium-ion is marked by a transparent oxygen-ion (left); light gray: oxygen, dark gray/horizontal grating: RE in C$_{3i}$ site, medium gray/vertical grating: RE in C$_2$ site; black: shifted Er ions

Atom	Sym.	Ox.	Wyckoff number	X	Y	Z
O	-	-2.000	48e	0.14161(5)	0.13104(5)	-0.09503(6)
Y	C_2	3.000	24d	0.25000	0.2854(1)	0.00000
Y	C_{3i}	3.000	8a	0.00000	0.00000	0.00000

Table 2.2: Atomic positions for Y_2O_3 [and01]

to small errors.

Dopant ions are incorporated in both symmetry sites into the crystal [man63, for69, mix99]. It can be assumed that both symmetry sites are statistically populated and no clustering of dopant ions occurs in bulk crystal growth, however no experimental proof of this has been given up to now. In yttria and lutetia ytterbium ions are currently assumed to replace the host ions in the same location due to their similar ionic radii of 0.90 Å for yttrium, 0.86 Å for lutetium, and 0.87 Å for ytterbium. Scandium on the other hand has a much smaller ionic radius of 0.75 Å which means that incorporated rare-earth ions substantially stretch the surrounding lattice. This leads not only to very small distribution coefficients (see appendix A) and small maximum dopant concentrations [pet98, for99] but also to a shift of the dopant ion from the original lattice position. This shift was first observed by K. Anduleit employing the X-ray holographic method described by Szöke in [szo93, szo97] with Er:Sc_2O_3. In Er:Sc_2O_3 the erbium ions appear to be shifted by 2 Å from the C_{3i}-site along the [111]-axes or from the three closest C_2-sites to an interstitial lattice site (indicated by arrows in figure 2.2 top and bottom left) [and01]. An oxygen vacancy is probably located at the oxygen position closest to the shifted erbium ion which creates the necessary space for the erbium ion with a radius of 0.89 Å (see figure 2.2 bottom). In thermodynamical equilibrium the number of oxygen vacancies in the crystal is sufficient to support shifts of dopant ions up to doping levels of a few percent. Charge compensation is provided by cation vacancies which appear in the same amount [kit83]. The resulting lowered site symmetry of the dopant ions can be correlated to the otherwise unexplained short radiative lifetime of the erbium energy levels in scandia compared to the other sesquioxides. For the $^4S_{3/2}$ level a lifetime of 13.7 µs in scandia were measured, for Er:Y_2O_3 73.4 µs and Er:Lu_2O_3 66.0 µs [pet98]. It has to be checked whether this shift of lattice positions only appears in scandia or maybe also in lutetia and yttria doped with the larger rare-earths e. g. cerium or praseodymium. In the case of ytterbium-doped scandia it is currently not known if the dopant ions are shifted in the lattice. The measured lifetimes (see section 6.1.2) do not indicate such a shift.

n	pair-type					
	C_2-C_2		C_2-C_{3i}		C_{3i}-C_{3i}	
	z_n	d_n	z_n	d_n	z_n	d_n
1	4	0.331	6	0.329	6	0.500
2	4	0.381	6	0.379	12	0.707
3	2	0.500	12	0.599	8	0.866
4	4	0.505	12	0.628	6	1.000
5	4	0.570	6	0.757	24	1.118
6	4	0.600	6	0.780	24	1.225
7	4	0.629	6	0.802	12	1.414
8	4	0.656	6	0.824	30	1.500
9	6	0.659	12	0.907	24	1.581
10	6	0.707	12	0.927	24	1.658

Table 2.3: Coordination numbers z_n of the different pair types and cation-cation distances d_n of the coordination shells n in units of the lattice constant

Due to their high cation density cooperative processes (see section 4.2) are very likely in the sesquioxides. There are three types of neighboring pairs: C_2 - C_2, C_2 - C_{3i}, and C_{3i} - C_{3i}. In contrast to the single ions the combined ions of a pair do not have any higher symmetry. This has a major effect on the selection rules and transition strengths (see section 4.2). The three pair types and their local surroundings in the crystal are depicted in figure 2.3. In the C_2 - C_2- and C_2 - C_{3i}-pairs the rare-earth ions share two neighboring oxygen ions each, and in the C_{3i} - C_{3i}-pair the ions do not share any oxygen ions. Also, the C_2 - C_2- and C_2 - C_{3i}-pairs have very small distances of only $0.3a_0$ between the cations, whereas the C_{3i} - C_{3i}-pair has a distance of $0.5a_0$.

The existence of a dopant ion introduces a local distortion to the crystal lattice if the size of the dopant significantly differs from that of the host [kiz96]. This can introduce a change to the crystal field acting on other dopant ions nearby, thus changing the energy level structure of the dopant ion. Also exchange coupling, the main interaction causing pair effects, is known to reach out over a distance of approximately 9 Å in sesquioxides [heb70, koe71]. It is therefore not sufficient to concentrate only on nearest neighbor pairs to explain all features visible in the spectroscopic measurements [heb76, pla76]. The interionic distances with respect to the lattice constant and coordination numbers for the first ten coordination shells are listed in table 2.3. The probability W to find a certain number of ions a in the
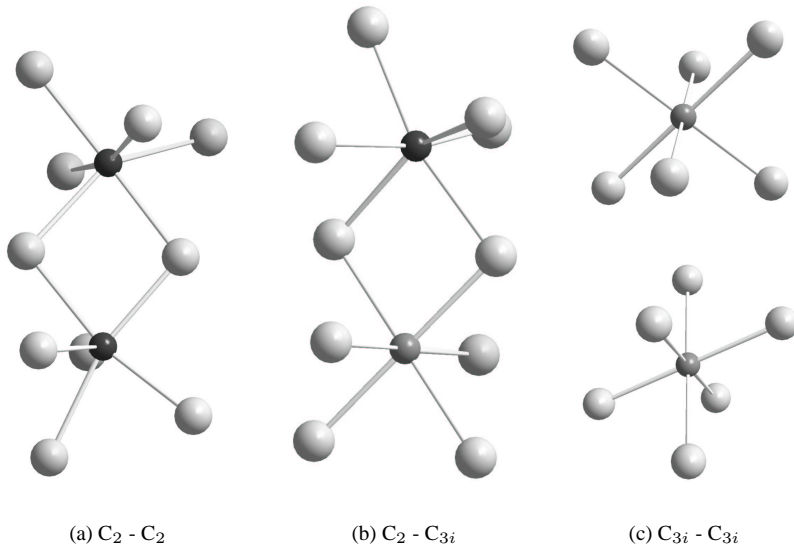
(a) C_2 - C_2 (b) C_2 - C_{3i} (c) C_{3i} - C_{3i}

Figure 2.3: The three types of cation pairs in cubic sesquioxides; light gray: oxygen, medium gray: RE in C_{3i} site, dark gray: RE in C_2 site

n^{th} coordination shell but not closer at a given dopant concentration c is given by:

$$W_{a,n}(c) = \left(\prod_{q=0}^{a-1} (z_n - q)c \right) (1-c)^{z_n - a + \sum_{l=0}^{n-1} z_l} \tag{2.1}$$

with the normalization condition:

$$W_{0,n}(c) + \sum_{q=1}^{z_n} W_{q,n}(c) = 1 \qquad \text{with} \qquad W_{0,n}(c) = (1-c)^{z_n + \sum_{l=0}^{n-1} z_l} \tag{2.2}$$

Unfortunately, due to the large number of possible ion combinations a dominant pair type can only be found for dopant concentrations above 50%. In this case dopant ions with the maximum number z_1 of dopant ions in the first coordination shell become dominant. At lower concentrations at least five to ten pair combinations of ions from several coordination spheres for each pair type are equally probable, so that a clear correlation between a certain spectral phenomenon and a corresponding pair interaction is essentially impossible.

	Sc_2O_3	Y_2O_3	Yb_2O_3	Lu_2O_3
IR-ab-sorption [cm^{-1}] [pie74, sch70b]	635	120, 312, 343, 390, 405, 468, 561	132, 341, 388, 405, 490, 573	125, 133, 309, 337, 350, 390, 405, 495, 580
IR-trans-mission [cm^{-1}] [mcd66, blo72]	-	120, 173, 183, 197, 241, 312, 343, 390, 405, 468, 561	90, 125, 132, 304, 341, 388, 405, 490, 573	90, 125, 133, 182, 309, 337, 350, 390, 405, 495, 580
Raman-lines [cm^{-1}] [sch70, hen99]	*109*, *194*, *226*, 258, 278, *325*, 357, *364*, *396*, **423**, 434, *499*, *527*, 630, 672	*109*, *135*, *167*, 199, *226*, *322*, *336*, **383**, 436, *474*, *597*	99, 121, 279, 305, 358, 420, 443, 621	*102*, *109*, *124*, 140, 177, *227*, 352, **396**, 458, *503*, *618*
$E_{P,eff}$ [cm^{-1}] [wes92]	419.9	405.9	-	-

Table 2.4: Phonon energies [mcd66, sch70b, blo72, pie74, hen99]. Strong Raman phonons: italic, very strong: bold; Partial identifications of the lines can be found in [sch70b]

An important figure for the treatment of pair processes is the probability that an ion has at least one nearest neighbor of a certain type, which is given by:

$$W_p(c) = \sum_{a=1}^{z_n} W_{a,n}(c) = z_n c^2 (1-c)^{\sum_{l=0}^{n-1} z_l} \tag{2.3}$$

2.2 Phonons

Lattice vibrations have substantial effects on a laser crystal. They take a major part in the transport of heat through the crystal and also affect the spectroscopic properties of the active ion. Multi-phonon-relaxation can cause high transfer rates between energetically close electronic levels, and phonon assisted energy transfer helps to convey energy from a donor-ion to an acceptor-ion with non-resonant

energy levels. The coupling between electronic $4f$-levels and phonons in trivalent ytterbium is the strongest of the trivalent rare-earths. Transitions between combinations of electronic and phononic levels, also called vibronic levels, play an important role in Yb spectroscopy, since they appear as strong as electronic transitions in the absorption and emission spectra. The knowledge of the phonon dispersion in the host crystal can help to identify the features observed in the spectra.

Unfortunately no complete sets of dispersion curves, measured by neutron scattering, have been published. Infrared transmission and absorption measurements as well as Raman-scattering experiments can only cover a small portion of the full dispersion relation. Table 2.4 shows the values of recent measurements and data taken from literature. The values will be used for identification of the electronic Stark-levels later in this work. The effective phonon-energies $E_{P,eff}$ are calculated using the temperature dependance of the europium $^5D_0$ emission and denote the average phonon energy of coupling phonons in multi-phonon relaxation processes [wes92].

The phonon energies in the sesquioxides are small compared to other oxides. The effective phonon energies for scandia and yttria are slightly above 400 cm^{-1} which is comparable to the effective phonon energies in fluoride hosts such as YLF. YAG has an effective phonon energy of approximately 700 cm^{-1}.

2.3   Thermal Conductivity

The thermal conductivity in insulator crystals is mainly caused by lattice vibrations. Local heating of the crystal leads to a population of phononic states which dissipate through the crystal lattice. The heat conductivity is limited by phonon scattering at the sample surfaces, surface defects, lattice defects, and impurities, as well as umklapp-processes depending on the sample temperature [ash76].

The thermal conductivity of yttria was first measured by Klein and Croft [kle67] to be $27 \frac{W}{mK}$. This extraordinarily high value, however, could not be reproduced with the crystals grown in Hamburg. The values measured with the new crystals are given in table 2.5. In the undoped case scandia has the highest thermal conductivity of $16.5 \frac{W}{mK}$, lutetia with $12.5 \frac{W}{mK}$ the lowest of the sesquioxides. In case of ytterbium-doping the thermal conductivity of scandia however is strongly reduced to less than half of its original value. Nearly the same effect can be seen for undoped and Yb-doped yttria. Lutetia exhibits only a slight decrease in thermal conductivity to $11.0 \frac{W}{mK}$ when doped with ytterbium. This can be explained by the fact that ytterbium and lutetium have very similar masses and ionic radii. The ytterbium-doping provides only a small disturbance to the crystal lattice and

	30 C	50 C	60 C	70 C	80 C	90 C	100 C
Sc_2O_3	[16.5]	15.5	14.9	14.4	13.9	13.6	13.3
Nd(0.1%):Sc_2O_3	11.6	11.3	-	11.9	-	-	10.5
Yb(2.8%):Sc_2O_3	6.6	6.4	-	6.5	-	-	6.3
Y_2O_3	[13.6]	12.8	12.4	12.0	11.6	11.2	10.8
Nd(0.5%):Y_2O_3	9.2	8.9	-	8.7	-	-	8.7
Yb(2.7%):Y_2O_3	7.7	7.4	-	7.2	-	-	6.8
Lu_2O_3	[12.5]	12.2	11.9	11.6	11.2	10.8	10.3
Nd(0.5%):Lu_2O_3	[11.1]	11.0	11.0	10.8	10.6	10.3	10.0
Yb(2.7%):Lu_2O_3	[11.0]	10.8	10.7	10.6	10.3	10.1	9.8
YAG	11	-	-	9.2	-	-	8.4
Yb(5%):YAG	6.8	-	-	6.3	-	-	6.0
Yb(10%):YAG	6.5	-	-	6.1	-	-	5.8

Table 2.5: Thermal conductivities of doped and undoped sesquiox-
ides in $\frac{W}{mK}$ in comparison to YAG [lis98, lis98b, hoh99].
Values in [ ] are estimated. Due to the higher cation density
in sesquioxides the Yb(2.x%):RE_2O_3 crystals are compa-
rable in Yb ion density to the Yb(5%):YAG sample.

therefore affects the phonon scattering only slightly. The thermal conductivity
of Yb-doped lutetia is more than 50% higher than that of Yb-doped YAG which
makes lutetia a very promising host system for ytterbium based laser systems.

2.4 Optical Properties

2.4.1 Transparency Range

The absorption-edge spectra of non-doped sesquioxides were measured by the
method described in section 5.1. The spectra are shown in figure 2.4. The used
samples were polished to about 100 µm in thickness to allow the measurement of
the strong absorption in this region. The absorption-edge can be identified by the
steep rise of absorption at 210 nm for scandia, 230 nm for lutetia and yttria, and
260 nm for ytterbia. The rather long absorption-edge wavelength of ytterbia can
be explained by a ligand-metal charge-transfer transition of the Yb^{3+}-ion. Mix
observed a rise of this absorption with rising ytterbium-concentration in sesquiox-
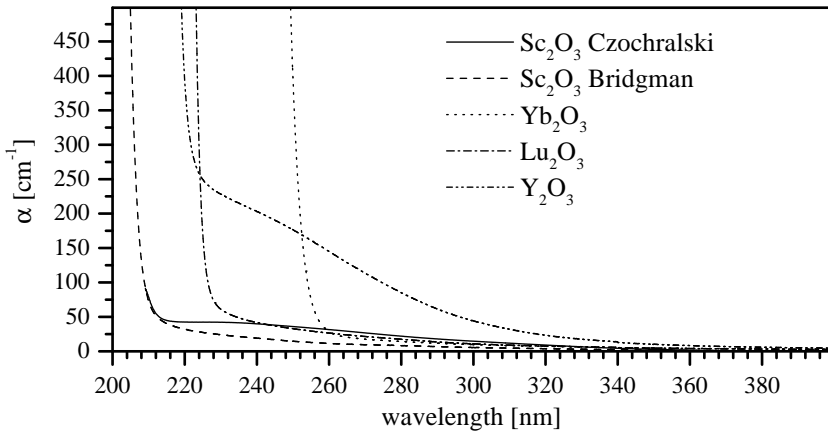ide crystals [mix99]. A similar absorption behaviour was also observed in garnets

Figure 2.4: Absorption spectrum of undoped sesquioxides

by Pieterson et al. [pie00].

Some samples show an additional broad absorption band between the absorption edge and 350 nm. These absorption bands have been observed earlier by Tippins in scandia and were thought to be intrinsic for the material since they could not be removed or changed by annealing after growth [tip66, pet98]. Recent measurements with scandia-crystals grown by the Bridgman-method reveal that the strength of the additional absorption band depends on the manufacturing process. Higher quality crystals do not show this absorption, which indicates that it is caused by formation of color centers due to certain defects that occur during the crystal growth by the Verneuil- and Czochralski-method. However, the underlying mechanism has not been studied up to now.

In the infrared region the transparency range of bulk material has only been measured for yttria. Nigara measured absorption coefficients of 30 - 70 cm^{-1} in the region around 9 - 10 μm [nig67]. Heitmann observed similar spectra with thin layers of yttria and scandia on KBr [hei73].

2.4.2 Photodarkening

The term photodarkening applies to the formation of color centers in materials after irradiation with light. Experiments with Eu:Y_2O_3 powder by Künzler et al. showed a decrease of the europium $4f$ transition intensities after 100 h broadband UV irradiation with a mercury lamp [kue92]. Experiments with undoped bulk sesquioxides have revealed several different unidentified luminescence cen-
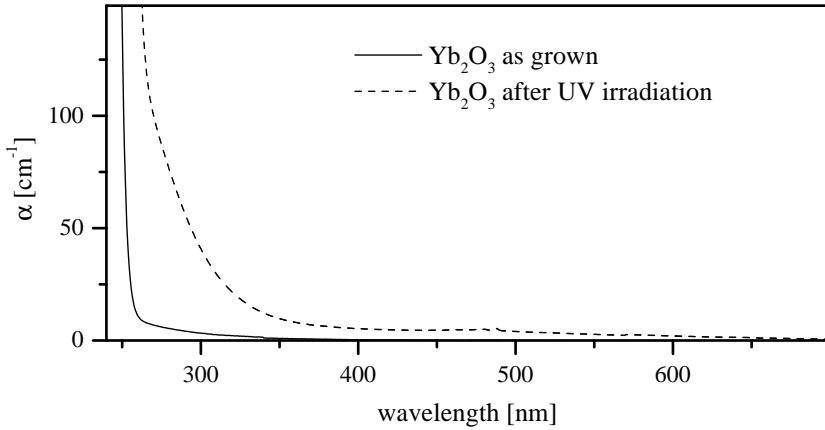
Figure 2.5: Absorption spectrum of Yb_2O_3 before and after UV-irradiation

ters with strongly overlapping excitation and emission bands. Excitation of the strongest visible absorption band feature around 240 nm caused the fast formation of light-brown color centers after a few minutes of irradiation in all four tested sesquioxides. The absorption spectrum of irradiated ytterbia is shown in figure 2.5. A broad additional absorption between the absorption-edge of ytterbia and 700 nm is clearly visible. The discolorations disappear completely after storing the crystals at room temperature for several days. Until now it is not known what kind of color center is formed under UV irradiation in these materials.

3

Crystal Growth

The use as a laser material requires crystals of exceptionally high optical quality. Low optical quality of the active laser medium results in poor laser performance or no laser oscillation at all. Crystal losses can be caused by inclusions like gas bubbles or precipitates, strain induced birefringence or lattice defects like grain boundaries. Another important point is the homogenous distribution of the dopant ions. Inhomogeneities can cause irregular heating of the crystal and therefore inhomogeneous thermal lensing up to the destruction of the crystal due to local thermal expansion. All of the defects mentioned above can be considerably reduced by careful choice of the growth method and growth parameters.

Due to the high melting points of the sesquioxides above 2400 C special consideration has to be given to the substances near the hot melt like crucible or insulation materials. Established growth methods have to be adapted for use at high temperatures to allow for controllable growth conditions.

Several growth methods for the high melting sesquioxides that have been applied in the past will be presented and evaluated in the first part of this chapter. The used crystal growth systems and the choice of crucible and insulation materials for the growth of oxide crystals above 2400 C will also be discussed. The focus of this chapter is on the Bridgman- and HEM- methods which yielded the best results of the tested growth methods. The last part of this chapter describes the various defects observed in the grown crystals and suggests strategies to circumvent these problems in the growth process.

More detailed discussions of certain aspects of the preparation of sesquioxide crystals may be found in the theses [pet98, mix99, for99]. Elaborate descriptions of and numerous references on all described methods except for the HEM technique can be found in the book of K. T. Wilke [wil88].

The growth experiments presented in this work focus on the manufacturing of scandia and lutetia. Yttria exhibits a phase transition from the hexagonal high temperature phase to the cubic room temperature phase slightly below its melting point. This phase transition causes strong stress in the grown crystals and therefore lower the crystal quality. Scandia and lutetia do not exhibit such a phase transition and the quality of the grown crystals is substantially better. Since yttria exhibits no outstanding spectroscopic features no further growth experiments were made with this material (see [pet98, mix99, for99] for previous results).

3.1 Growth Techniques for High Melting Oxides

3.1.1 Growth Methods without Crucible

The crystal growth methods described in this section have in common that the problem of high temperatures is avoided by not bringing the melt in contact with substances other than the original material itself and the surrounding atmosphere, which can be any inert or oxidizing gas mixture in the case of the sesquioxides.

Verneuil- or Flame-Fusion-Technique

When crystals are grown by the Verneuil- or flame-fusion-method the starting material, ground to a fine powder, is dropped through a flame or glow discharge onto a seed crystal. The chemicals are molten while passing through the flame and re-crystallize on the surface of the seed crystal. Due to the irregular application of the molten material and the high cooling rates, the risk of forming inclusions in the growing crystals is very high. Also the crystals usually exhibit strong thermal stress. Therefore it is very complicated to grow large single crystals of high optical quality by this method.

Sesquioxide crystals have been grown by the Verneuil-method since the late fifties [bar57, lef62]. Most published spectroscopic data since that time have been measured using crystals grown by this method. Also the first laser operation of sesquioxide crystals has been achieved using these early crystals. The first published sesquioxide laser is Eu:Y_2O_3 by Chang in 1963 [cha63] and the first Nd:Y_2O_3 laser was presented by Hoskins in 1964 [hos64].

Scull-Melting

This method employs a water cooled crucible to hold the starting material. The chemicals are heated directly by an induction coil. Since most powder materials cannot be heated directly by induction at low temperatures small pieces of metal

are added to start the heating process. The molten zone does not reach the crucible walls due to the water cooling of the crucible. A crust of solid polycrystalline material remains between the molten zone and the crucible. This ensures that the melt does not reach any other substances thus removing the problem of finding suitable crucible and insulation materials. The crystallization is started by slowly lowering the temperature. Due to the contact to the surrounding solid material the crystallization starts in many places simultaneously which leads to many small single crystals that usually exhibit strong thermal stress. To produce larger single crystals by this method, a very large amount of starting material has to be used. The efficiency of this method is therefore very low. However, the scull-melting-method has been successfully used to grow crystals of very high melting substances such as UO_2 and ThO_2 with melting points of 2878 C and 3400 C [her81]. It has also been used to grow various sesquioxide crystals by Aleksandrov et al. [ale78] and is currently used to grow zirconia as synthetic gemstone.

Floating-Zone-Technique

The floating-zone-method requires starting materials in the form of sintered rods. The rod is fastened on a vertically movable mount. The tip of the feed rod is then heated by a focused lamp, laser (LHPG[1]), or an induction coil until a small molten drop appears at the tip. A seed crystal or pulling rod is then brought into contact with the molten zone and the crystal is grown from this droplet. The feed and pulling rod have to be constantly adjusted at different rates to ensure a constant size and shape of the molten zone and a constant diameter of the grown crystal. The maximum diameter of the grown crystals is limited by the type of heating and the viscosity of the melt. In the case of sesquioxides the diameter using the LHPG-method is limited to less than 2 mm. Despite the small crystal diameters this method can be used to grow crystal-fibers which can also be used as laser materials when the optical quality of the surface is good enough to allow waveguiding. It is also interesting since the method is very fast and needs only a very small amount of starting material. The grown crystals usually have adequate quality for spectroscopic investigations and are free of impurities from crucible or insulation materials.

The high melting sesquioxides have first been grown by this method by Gasson in 1970 [gas70]. In the course of this work small samples of ytterbia were grown by this method in order to compare the amount of impurities already existing in the starting materials to that in the crystals grown from a crucible.

---

[1]Laser-heated-pedestal-growth

3.1.2 Growth Methods with Crucible

Crystal growth techniques that use a crucible generally allow the growth of larger, compared to floating-zone methods, or higher quality crystals, compared to the Verneuil-method. This is mainly due to the fact that the crystallization conditions can be controlled substantially better than with those methods that do not use a crucible.

Czochralski- and Nacken-Kyropoulos-Technique

The Czochralski-method is probably the most widely used crystal growth method at this time. It is successfully used for the growth of single crystal metals, semi-conductors, and insulators. It allows to use a fairly high percentage of the starting materials while achieving very high quality crystals. The maximum size of the grown crystals is basically limited only by the size of the used crucible. Silicon single crystals are currently grown under industrial conditions up to a diameter of 22 inch [sil01]; YAG crystals are commercially available up to 3 inch diameter [fee01].
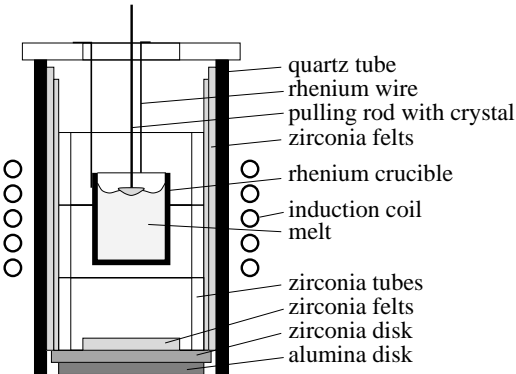

- quartz tube
- rhenium wire
- pulling rod with crystal
- zirconia felts
- rhenium crucible
- induction coil
- melt
- zirconia tubes
- zirconia felts
- zirconia disk
- alumina disk

Figure 3.1: Insulation setup for Czochralski growth of the high melting sesquioxides

An open crucible, usually made of metal or graphite, is placed in an insulation setup and the starting material is molten by resistive or inductive heating (compare fig. 3.1). The heating is reduced again until the melt is only slightly above its recrystallization point. Then a seed crystal or pulling rod is dipped into the melt and some material crystallizes onto the seed. Due to the heat transfer through the pulling rod the crystallization continues until an equilibrium between the heat delivered from the crucible wall and that transferred through the pulling rod is reached. The isothermal plane between the growing crystal and the melt, the so called interface, is now stabilized. The pulling rod is then pulled up at a rate of typically 0.1 - 6 $\frac{mm}{h}$ and further material crystallizes onto the grown crystal. The diameter of the growing crystal can be controlled by adjusting the temperature of

the crucible which, in turn, regulates the shape and dimension of the solid-liquid interface. In oder to ensure mono-crystalline growth, a seed crystal needs to be selected in the first stage of the growth. When the pulling rod is dipped into the melt, crystallization starts in many places on the tip of the rod. A single seed can be selected by growing the crystal at a small diameter of one or a few millimeters during the first 5 to 10 mm of growth. During this time the fastest growing seed usually outgrows the other seeds and forms the interface alone and provides a single crystal interface. When a single crystal seed is used instead of a simple pulling rod, the seed selection is generally not necessary.

The crystals grown by this method usually have low mechanical stress and show a very high optical quality due to the fact that the growing crystal has no contact to the crucible, and the thermal gradients can be accurately controlled to avoid stress through thermal deformation.

Experiments to grow the high melting sesquioxides by the Czochralski-method have been made at our institute between 1996 and 1998. After a crucible/insulation combination had been found that could withstand the high growth temperatures (see fig. 3.2.2), experiments with rare-earth-doped and non-doped sesquioxides were made. However only small crystals of 5 - 15 mm in diameter and 3 - 5 mm in length could be obtained. After a few millimeters of growth, the crystals lost contact to the melt. This behaviour could not be encountered by lowering the heating power, which led to growth of fin-like structures. These problems can be explained by the high emissivity of the sesquioxides at melting temperature of 0.6 to 0.8 [mcm68]. Since the energy transport at high temperatures is dominated by radiation, the high absorption of the growing crystal leads to a pile-up of heat at the interface and the crystallization stops. An in-depth description and discussion of the Czochralski-growth-experiments and the occurring problems can be found in [pet98, mix99, for99].

The problems can be circumvented partly by using the Nacken-Kyropoulos-method. This method is similar to the Czochralski-method in the beginning. After a short period of growth according to the Czochralski-method the pulling process is stopped and the crystal is left in contact to the melt while the system is slowly cooled. The grown crystal acts as a seed for the crystallization of the melt in the crucible. Unfortunately this method cannot prevent the formation of other parasitic seed crystals at the surface and the crucible wall, which leads to the formation of several single crystals. Furthermore there is no room to compensate for changes of the material volume during crystallization and cooling after the surface of the melt has solidified. This leads to strong thermal stress and cracked crystals. Nevertheless the size and quality of the sesquioxide crystals grown by this method were substantially better than those grown by the Czochralski-method.

Flux-Growth

A way to circumvent the high growth temperatures of the sesquioxides is to find a suitable solvent (flux) for the materials. By mixing the crystal material with the solvent the melting point is lowered which allows the use of crucible materials that would not withstand the melting temperatures of the solute. The crystal growth itself is similar to the Czochralski-method, and is often referred to as top-seeded solution growth (TSSG). A typical limitation of this method is that the amount of solute that can be solved in the flux at a given temperature is limited. During growth the amount of solved material in the flux decreases and when a certain concentration is reached the crystal growth has to be stopped to avoid the crystallization of other phases or the flux itself. Therefore the maximum crystal size that can be obtained is limited unless the solute concentration is kept constant by feeding more solute to the flux during growth. Another drawback of this method is the low crystallization rate. Usually crystals can only be grown at rate of well below 1 $\frac{mm}{h}$. Furthermore, there is very often a certain amount of flux included in the growing crystal which limits the obtainable quality.

Scandia has been successfully grown by the flux-method from a PbO-V_2O_5 flux at temperatures around 1300 C by Chen et al. [che90]. Recent experiments by L. Fornasiero, using an alumina flux, did not yield better results than those obtained by the Czochralski-method since the melting temperature was lowered only slightly [for99].

Bridgman-Technique

The Bridgman-method is a gradient freezing technique. The crucible is placed in a temperature gradient so that the middle of the bottom is the coldest point of the system. The crucibles used with this method are usually conically shaped. A seed crystal can be placed at the bottom of the crucible to ensure mono-crystalline growth or a certain crystallographic growth axis. After the raw material is molten the crucible is lowered through the temperature field and crystallization starts from the bottom up. In the case of conical crucibles parasitic crystallization from the crucible walls can be avoided in most cases. In contrast to the Nacken-Kyropoulos-method crystals with rather low thermal stress can be produced by the Bridgman-technique, since there are no problems with volume changes during solidification of the melt. Some thermal stress is of course induced near the crucible walls due to different thermal expansion coefficients of the crystal and crucible material.

The Bridgman-method has been successfully used to grow large sesquioxide boules with single crystals up to about 1 cm^3 volume [pet98, mix99, for99].
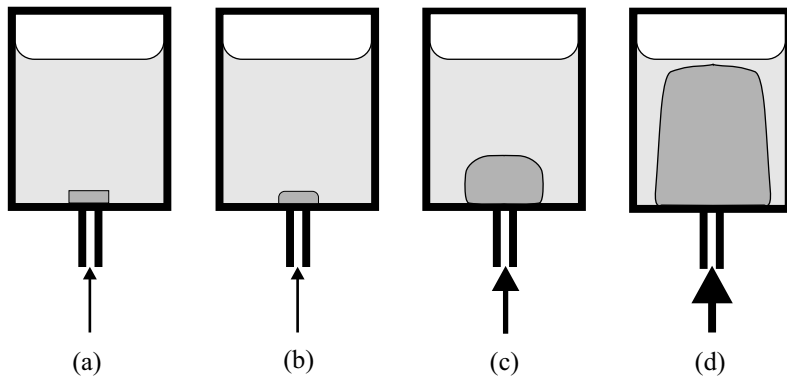
Figure 3.2: Scheme of crystallization by the HEM-method; a) melting of the starting material; b) lowering of the gas flow to partly melt the seed crystal; c) crystallization at medium gas flow; d) crystallization at high gas flow before the heating power is reduced

Heat-Exchanger-Method (HEM)

The HEM-technique is derived from the Bridgman-method. Instead of lowering the crucible through a temperature gradient the crucible is kept in an isothermal insulation setup. The crystallization is performed by a controlled flow of cooling gas through a heat exchanger at the center of the bottom of the crucible (see fig. 3.2) [sch70, vie74, del80]. At the beginning of the growth run the material is heated at a low gas flow until a seed crystal, placed on the bottom of the crucible, is partially remolten. Then the gas flow is increased and the crystallization starts from the seed into the melt. Since the temperature of the crucible walls remains unchanged, the growing crystal cannot reach the walls until the end of the growth process which prevents secondary nucleation and ensures very low strain in the crystal. At the end of the growth process the heating power is reduced and the crystal comes into contact with the crucible walls. HEM is successfully utilized for the growth of large sapphire crystals. By this method more than 95% of the melt can be converted into high quality single crystalline material.

First experiments to grow the high melting sesquioxides using this method were made in 2000 and the results are presented below.

3.2   Experimental Setup

3.2.1   Growth Systems

The melting temperatures of the sesquioxides of above 2400 C can be reached in a crystal growth apparatus in several ways. The material can be heated either by a flame, an arc, a focused lamp, or a laser beam or inductively with a radio frequency coil. Crystal growth methods that employ a crucible usually require inductive or resistive heating.

At our institute three crystal growth systems are available for high temperature use. One fiber growth system using the LHPG-method and two Czochralski systems that were used in the Czochralski-, Nacken-Kyropoulos-, Bridgman-, and HEM- experiments.

The LHPG system is heated by a 25 W cw CO_2-laser type Ultra Lasertech PX3500 and a 90 W Nd:YAG laser type Rofin-Sinar RSY90Q. The beams are focused on a pressed rod of the starting material by a ZnSe lens and polished copper mirrors. Two drivers are available to control the translation and rotation of the feed and the pulling rod [lak99].

The Czochralski-systems differ mainly in size of the usable crucibles. Both are powered by high frequency generators manufactured by Hüttinger. The small system, constructed by Heraeus, for crucibles up to 22 mm in diameter has a radio frequency generator with a maximum of 10 kV output voltage at a frequency of 200 kHz and 35 kW maximum output power. The water cooled induction coil has an inner diameter of 45 mm and 5 turns. The generator power and the pulling rod translation and rotational speed are controlled manually in this setup. The temperature control is given by a one-color pyrometer looking through a viewing port down on the crucible from the top of the growth chamber. This system is mainly used for testing purposes and to grow crystals for spectroscopic investigations because the required amount of raw material is low and crystals of medium quality can usually be grown in less than one day.

The large growth system is manufactured by Crystalox. It has also a generator with a maximum of 10 kV output voltage at a frequency of 400 kHz and 36 kW maximum output power. The induction coil used for the high-temperature experiments has an inner diameter of 110 mm and 7 turns. This system can be used with crucibles up to 45 mm in diameter which can be filled with 150 to 300 g of chemicals. The use of this large setup is more costly and time consuming than the use of the small setup. However, the crystal quality is considerably better when large crucibles are used since the growing crystal has more space and time to develop an inclusion-free mono-crystalline structure. Furthermore, the temperature gradients are lower in a large crucible than in a small one which reduces the formation of
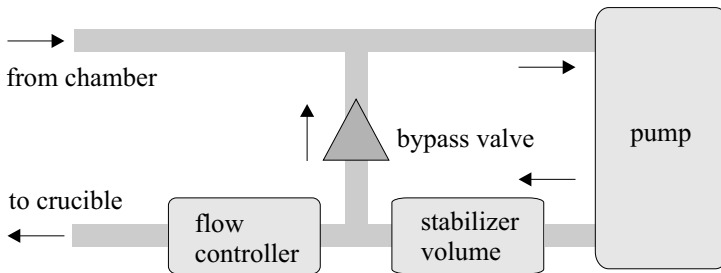
Figure 3.3: Scheme of the gas flow system

stress and birefringence in the crystal. The original setup allows semi-automatic control of the generator power and manual control of the pulling rod. Also a one-color pyrometer is installed at the top of the growth chamber. Furthermore a weighing-system for the crucible is present to allow an automatic diameter control of the growing crystal when using the Czochralski-method.

The original system has been improved by installation of a new computerized controller for the generator power. A two-color pyrometer, pointed towards the center of the bottom of the crucible, was added for the Bridgman- and HEM-methods to gain more accurate control of the system parameters and give feedback to the power controller. It also allows to compensate for changes in the insulation efficiency in repeated growth experiments, once the correct bottom temperature of the used crucible at the melting point of the chemicals is known. It therefore simplifies the reestablishment of certain growth conditions even with changed or degraded insulation materials. This is especially important for the HEM experiments where the melting point of the material has to be met with an accuracy of better than 10 C. Another enhancement for the HEM-method was the installation of a closed-cycle gas-flow system as shown in figure 3.3. The growth atmosphere is pumped out of and back into the chamber and blown against the bottom of the crucible. The used pump is an oil-free membrane pump type Leybold-Heraeus DI-VAC 2.4L with a maximum flow of 35 $\frac{1}{\min}$. The gas flow is adjusted by a computer controlled gas flow regulator type Unit UFC3101 with a control range of 1.5 to 200 $\frac{1}{\min}$. Between the pump and the regulator, a chamber with a volume of approximately 2 l was added to stabilize the intermittent output of the pump. Since the pump is not able to work against high output pressures a bypass valve had to be installed to keep the pump working under constant pressure and flow conditions.

3.2.2   Crucible and Insulation Materials

The high melting points of yttria and scandia restrict the choice of possible crucible materials. The crucible has to remain stable at temperatures well above the melting point of the crystal and, of course, must be resistant against chemical reactions with the melt. Experiments with several crucible materials, for example tungsten, rhenium, and carbon revealed that rhenium fulfills all these requirements to the greatest extent. Rhenium is sensitive to oxidizing atmospheres but sufficiently resistant to melts of Al_2O_3 and rare-earth oxides. The melting point of rhenium is approximately 3180 C. The crucibles with an outer diameter of 45 mm were fabricated by Heraeus by hot isostatical pressing of rhenium powder of well defined grain size. Subsequently, the material is sintered at 2500 C for several hours. The crucible is then brought into its final shape by grinding. The densities of the workpieces manufactured by this technique exceed 90% of the density of the massive material. Another large diameter crucible that was used solely for the HEM-experiments was galvanically manufactured by Engelhard-Clal. This crucible had a density of nearly 100% of massive rhenium which proved favorable for the growth experiments. Up to now no negative impact through possible impurities in this crucible from the manufacturing process has been noted.

Since no insulation material could be found that is stable in direct contact with the crucible at the required temperatures, the crucible needs to be completely surrounded by gas (see fig. 3.1). The outer insulation is made up of a quartz tube lined with zirconia felt mats. The bottom of the setup is also covered with zirconia felt to reduce the radiation losses from the bottom of the crucible. The insulation scheme depicted in figure 3.1 is slightly varied for the Bridgman- and HEM-techniques. A detailed description of this and other tested insulation setups for the growth of sesquioxides can be found in [for99, mix99].

3.2.3   Growth Atmosphere

The growth atmosphere used in the experiments has to comply with several different demands. On the one hand, the growth of oxide materials suggests the use of oxygen in the growth atmosphere but, on the other hand, the used rhenium crucibles are extremely sensitive to slight amounts of oxygen. Furthermore, the atmosphere has to inhibit disruptive discharges from the induction coil to the insulation setup. The best growth atmosphere up to now is 0.01% O_2, 10-15% H_2 and 85-90% N_2 at 1 bar pressure. The nitrogen protects the system from glow discharge. At higher pressures of 2-5 bar argon or helium can also be used instead of nitrogen. The large amount of hydrogen is needed to stabilize the crucible against the oxide melt inside. If a smaller amount of hydrogen is used, rhenium is slowly dissolved in the melt and forms metallic inclusions during crystallization. The hy-

drogen also binds oxygen released from the melt which results in the formation of color centers in the growing crystal due to oxygen deficiency. The color centers can be removed by annealing the crystals in air at 1000 C for several days. The after growth annealing is no longer necessary when a very small amount of oxygen is added to the atmosphere and the cooling rate after crystallization is lowered. By cooling the grown crystal down to approximately 2000 C in 4-5 hours the color centers can be completely removed in a crystal volume of about 25 cm^3.

3.3   Crystal Growth by the Bridgman-Method

Since no real Bridgman-growth facilities were available, the existing Czochralski-machines were slightly altered to allow growth by the Bridgman-method. The used setup is depicted in figure 3.4. The crucible is placed in a cage made of rhenium wire which is attached to the pulling mechanism of the Czochralski-apparatus. This allows rotation and vertical movement of the crucible. The crucibles used were modified Czochralski-crucibles. A small hole of 2 to 3 mm diameter was eroded into the bottom of the crucible and a tube was welded against the bottom. The seed crystal was placed in this tube. The insulation setup was similar to that used for the Czochralski-

Mo-rod
crucible support:
W-rods with Al$_2$O$_3$-wraping
Re-rods
quartz tube
Al$_2$O$_3$-hoop
zirconia felts

Re-plate
Re-cross
Re-plate
Re-crucible with melt
seed crystal
zirconia felt
zirconia mesh
Al$_2$O$_3$-ring
zirconia felt
Al$_2$O$_3$-disk

Figure 3.4: Insulation setup for Bridgman growth of the high melting sesquioxides

experiments. There were less zirconia felts used on the bottom of the setup to allow a higher cooling rate of the crucible bottom and to get additional space for lowering the crucible down from the induction coil. The crucible was covered
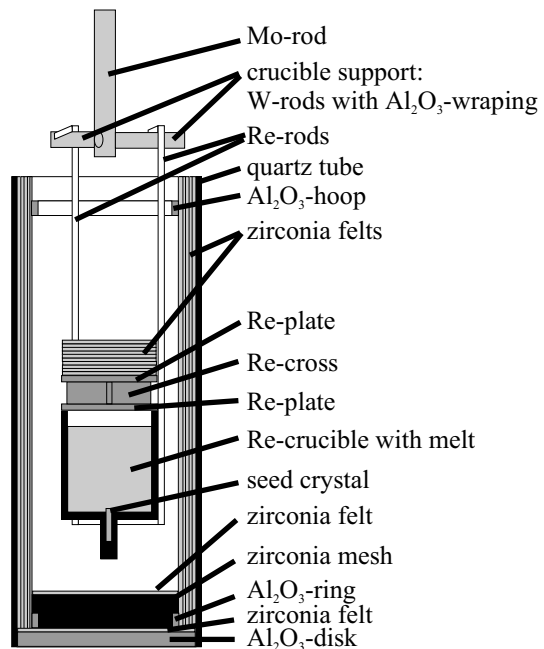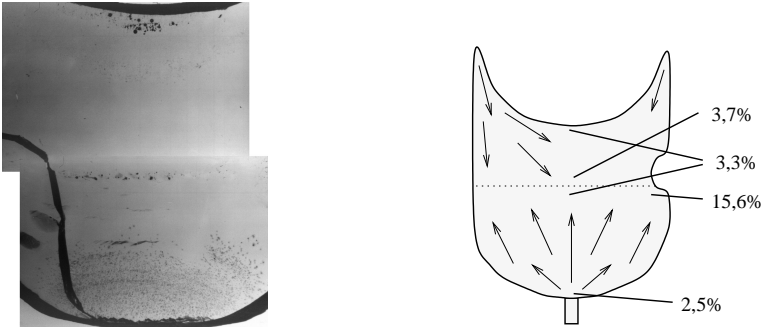
Figure 3.5: left: cross section of an Er:Sc$_2$O$_3$ crystal grown by the Bridgman-method; $\varnothing \approx$18 mm; right: reconstruction of the growth process according to rising erbium concentrations.

with a rhenium disk and zirconia felts to reverse the temperature gradient in the crucible as required for growth by the Bridgman-method.

Due to the rectangular cross-section of the crucible parasitic nucleation from the bottom of the crucible could not be inhibited. Another drawback of the used setup was that the crucible could not be fully lowered out of the induction field and therefore the crystal growth could only be partly accomplished by the Bridgman-method. The full use of the Bridgman-method would have required conical crucibles and more space for vertical movement of the crucible, both of which would have caused severe additional costs and substantial changes to the used growth setups. Therefore, the experiments presented here can only be regarded as first tries towards growing the high melting sesquioxides by the Bridgman-method leaving numerous possibilities for improvement and optimization.

The first sesquioxide crystal grown by the Bridgman-method was Er:Sc$_2$O$_3$. It was grown in a 19 mm diameter crucible that could be lowered about 1 cm from the induction coil. The progress of the crystal growth could be reconstructed by measuring the erbium concentration throughout the crystal. Since erbium has a distribution coefficient below unity in scandia (see appendix A) a rise of the erbium concentration means that this particular part of the crystal grew later in the growth process. Crystallization started, as intended, at the bottom of the crucible around the seed crystal and continued to grow upwards about 1 cm. After that the downward motion of the crucible was stopped and the heating power was reduced. This had the effect that now crystallization started also from the surface of the melt downwards. The plane where growth from the bottom and the top met can be seen
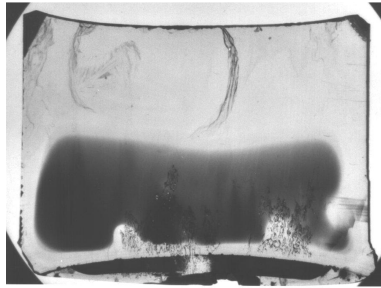
Figure 3.6: Bridgman Nd:Y_2O_3; $\varnothing \approx 38$ mm. The dark patch in the
lower half of the crystal is due to color centers that were
not fully removed by annealing

in the crystal as a layer of bubbles and inclusions due to the contraction of the melt
during crystallization. Here the highest erbium concentrations were measured.

Figure 3.6 shows a Nd:Y_2O_3-crystal grown by the Bridgman-method in a
40 mm diameter crucible. Unfortunately the starting material was not fully molten,
so a thin layer of ceramics remains near the bottom of the crucible. Despite this
obvious mistake the crystal shows only a little distortion when viewed under a
microscope and appears to be mostly mono-crystalline.

This underlines the high potential of the growth of sesquioxides by the
Bridgman-method. The average single crystal size reached throughout several
growth experiments [pet98, for99, mix99, moh00] was in the cm^3 regime and the
achieved crystal quality was substantially better than that reached with the previ-
ously tested methods. If an optimized growth facility and crucible/insulation setup
is used, a further increase of crystal size and quality can be expected.
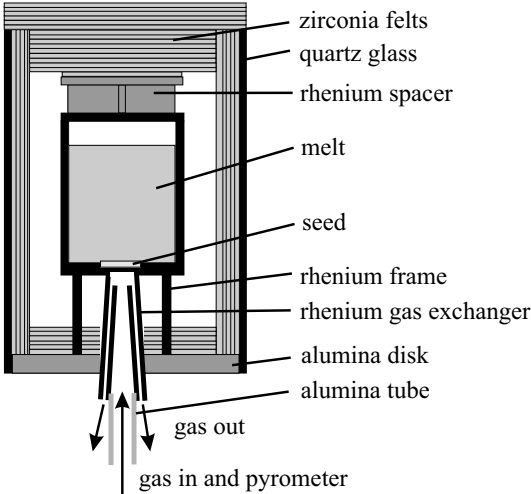
3.4   Crystal Growth by the Heat-Exchanger-Method

The insulation scheme for growth by the HEM-technique is depicted in figure 3.7. The crucibles used had a rectangular cross-section with two circular deepenings in the crucible bottom; one on the inside with 18 mm diameter and one on the outside with 10 mm diameter. The deepening at the inside provides space for a seed crystal of about 18 mm diameter and 1 - 2 mm thickness; that at the outside is needed to provide a stable connection to the rhenium heat-exchanger.

zirconia felts
quartz glass
rhenium spacer
melt
seed
rhenium frame
rhenium gas exchanger
alumina disk
alumina tube
gas out
gas in and pyrometer

Figure 3.7: Insulation setup for HEM

The insulation setup consists again of a quartz-tube lined with zirconia felts. The crucible is supported by a rhenium frame placed on a disk of high temperature resistant alumina. The alumina disk is also covered by several layers of zirconia felt. The crucible is covered with a rhenium disk and zirconia felts to obtain a nearly isothermal temperature distribution within the insulation setup. Due to the completely closed insulation setup the heating power needed to reach melting temperature is reduced to about 65 - 70% of the power needed with the Czochralski- or Bridgman-setups. This allows the use of zirconia felts without additional stabilization since the shrinking of the felt mats is strongly reduced due to the lower temperature of the outside crucible walls. The insulation setup can be reused for 3 - 5 growth experiments.

A conical rhenium tube fitting into the deepening in the outer crucible bottom is used as the heat-exchanger. The inner part of the tube is the gas inlet, small eroded channels in the wall of the tube form the gas outlet. The inlet is connected to a high temperature alumina tube which, in turn, is fixed to a steel tube leading to the pump. Since the system temperature is measured through the gas exchanger the crucible bottom temperature which corresponds to the melting point of the chemicals inside needs to be determined for each crucible. The temperature gradient through the bottom is in the range of 250 K for the used crucibles.

(a) bottom

(b) 2 mm up

(c) 4 mm up

(d) 8 mm up

Figure 3.8: Sc_2O_3 sample grown without seed and cut into horizontal slices; $\varnothing \approx 18$ mm; the polycrystalline structure formed after 4 mm of vertical growth is continued throughout the rest of the boule
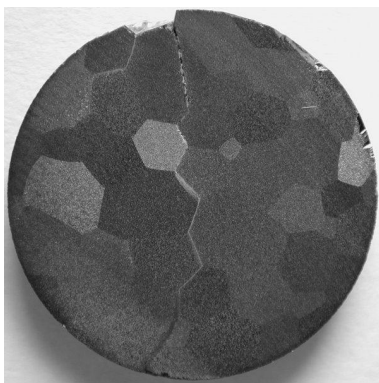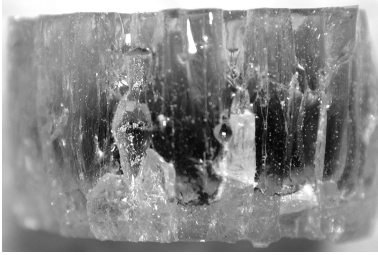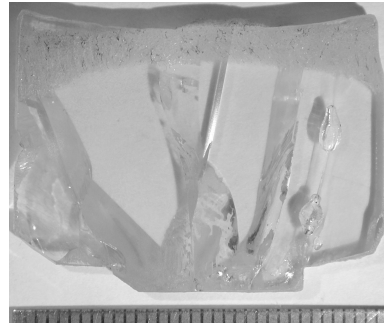
(a) With seed but not fully molten; ∅ ≈18 mm

(b) Without seed and fully molten starting material; ∅ ≈38 mm

Figure 3.9: Scandia crystals grown by HEM

The growth experiments were started by heating the crucible at various generator powers and cooling down again to determine the required power for melting the oxide material. The difference between the temperature measured by the pyrometer and the melting temperature of the oxide material gave the temperature gradient in the bottom. After the temperature gradient of the crucible bottom had been determined, the gas flow was added to the experiments. The gas flow was increased from approximately $2 \frac{1}{\min}$ to maximum within one hour; then the generator power was reduced to zero over a period of 1.5 hours. During the first growth experiments, that were carried out without a seed, the starting material was not fully molten and a ceramical layer of powder remained at the position of the seed. One of these crystal boules cut into horizontal slices is shown in figure 3.8. Figure 3.8(a) clearly shows the powder at the bottom of the crucible. About 2 mm up in the boule very small poly-crystals and many bubbles can be seen. This indicates that the material in this region was fully molten but still had a very high viscosity; so, the gas in the pressed starting material could not rise to the surface. 4 mm up in the boule the single crystals have become substantially larger and no more inclusions and gas bubbles are visible. In this part the starting material was fully molten and crystallization has advanced from many seeds initially to a small number of monocrystals. Basically the same picture can be found 8 mm up from the bottom near the surface, this means the crystals which were formed within the first 4 mm continued to grow throughout the rest of the crystal. This indicates that the used gas cooling had the desired effect and the growth method as such worked with the

used setup.

The following experiments were carried out using poly-crystalline seeds of 18 mm diameter and 2 mm thickness. The first crystal grown with a seed (figure 3.9(a)) showed some gas bubbles above the seed indicating that the melt was not hot enough at the beginning of the growth or was not kept long enough at melting temperature. It was cooled down to room temperature from melting point within 2 hours. This short time was sufficient to remove the color centers throughout most of the crystal.

In the next try the crucible bottom temperature was raised slowly by approximately 30 K compared to the temperature in the last try. This caused the seed crystal to melt which resulted in a quick rise of the bottom temperature of 80 K and therefore allowed the exact determination of the melting point. The gas flow was again increased to maximum within 1 hour and then the generator power was reduced over a span of 4 hours. The resulting crystal is shown in figure 3.9(b). It is completely free of visible color centers and consisted of only seven large single crystals, one of which had a volume of approximately 4 - 5 cm^3. The optical quality of this crystal was substantially better than that of all crystals grown before (see also section 3.5.3).

With these first results the HEM-technique appears to be very well suited for the growth of large, high quality bulk sesquioxides. The complex part is to determine the correct growth parameters. After this part is done the complete growth process can repeatedly run fully computer controlled and is therefore suitable for industrial application. Furthermore the method is easily scalable and can be set up in only slightly adapted Czochralski-facilities. The further optimization of the growth parameters and the use of mono-crystalline seeds should allow at least the growth of 25 - 30 cm^3 single crystals with excellent optical quality in the available growth system.

3.5 Defects

Defects in laser crystals can critically affect the performance of a laser system; it is therefore important to identify the occurring defects and to find methods to avoid them. This section deals with the defects most common in the grown crystals. An in depth study of the crystallographic defects in sesquioxides like twinning and stacking faults can be found in the works of C. Boulesteix [bou82].

3.5.1 Metallic Inclusions

Metal precipitates in a crystal are extremely harmful for laser operation. A small particle absorbs all pump and laser power reaching it and transforms it directly into
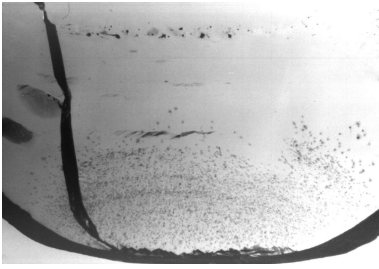
(a) Bridgman-Er:Sc$_2$O$_3$-crystal with tungsten precipitates in the area around the seed
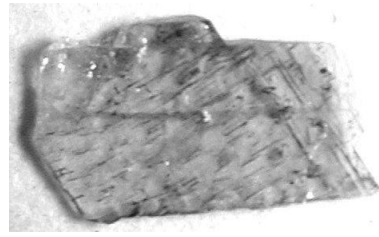
(b) Bridgman-Sc$_2$O$_3$-crystal with string-like rhenium precipitates (width 8 mm)

Figure 3.10: Metallic inclusions in grown sesquioxide crystals

heat. This can lead to the destruction of the crystal in the worst case if the local thermal expansion is too strong. Metallic inclusion therefore need to be completely avoided.

In early growth experiments tungsten wires were used near and at the edge of the crucibles as spacers. These wires partly disappeared during the growth process. Part of the material was found to be dissolved in the melt (see section 3.5.4) and more could be found as small metallic particles in the grown crystals, mainly in the volume that crystallized in the beginning of the growth process (see figure 3.10(a)). Of course, if no tungsten is used near the crucible the formation of these particles does not happen.

Another type of metallic inclusions can be found if more than 0.05% O$_2$ are present in the growth atmosphere. Above this oxygen concentration rhenium is dissolved in the melt and forms thin dendrite structures in the crystals (see figure 3.10(b)). Also larger rhenium precipitates and even droplets of several mm in diameter can be found at the bottom of the crucible.

3.5.2 Color Centers

The color centers that can be seen in sesquioxide crystals grown in strongly reducing atmosphere can be attributed to trapped electrons in oxygen vacancies, so called F-centers. The oxygen from the melt is emerging by the surrounding hydrogen. The amount of oxygen remaining in the melt is not sufficient for the growing crystal which leads to the formation of the color centers during growth. The ab-
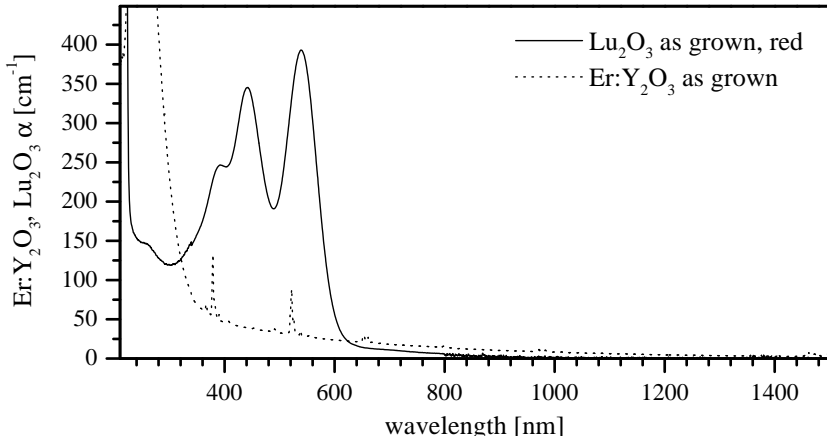
Figure 3.11: Absorption spectra of color centers in Y_2O_3 and Lu_2O_3

sorption spectra of the color centers in sesquioxides are shown in figure 3.11. The color centers in yttria show a featureless broad absorbtion between the UV and near IR. The crystals appear brown to black in color. Scandia exhibits a basically identical absorption band. Lutetia, on the other hand, shows four absorption bands between 200 and 650 nm, giving the crystals a strong red color.

The formation of color centers during growth is probably the reason for the poor performance of the Czochralski-method. Okano et al. observed a growth behaviour of $LiTaO_3$ similar to that of the high melting sesquioxides when color centers were present in the growing crystal [oka94].

The color centers can be fully removed from the grown crystals by diffusion of oxygen into the crystals [ber68]. Smaller crystals can be fully annealed in air at 1000 C within a few days. To efficiently decolorize large crystal volumes higher temperatures are needed to speed up the process. As mentioned in section 3.2.3 the color centers can be efficiently removed during the cool-down period of the growth if a small amount of oxygen is present in the growth atmosphere.

3.5.3 Stress-Induced Birefringence

Mechanical stress in the crystals can be caused during growth time by the contact to other materials with different thermal expansion coefficients like the crucible or even other crystals growing in different crystallographic directions. It can also appear during cooling due to phase transitions of the crystal. This mechanical stress, often referred to as thermal stress, causes slight local variations of the density in
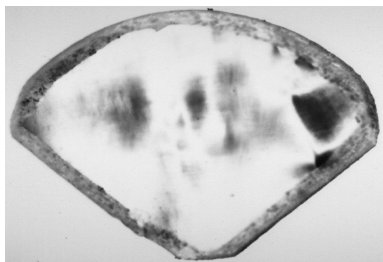
(a) Czochralski-
Er(15%):Lu$_2$O$_3$; width 6 mm
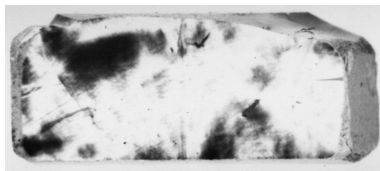
(b) Nacken-Kyropoulos-
Er(3%):Lu$_2$O$_3$; width 9 mm

(c) Bridgman-Sc$_2$O$_3$; width 8 mm
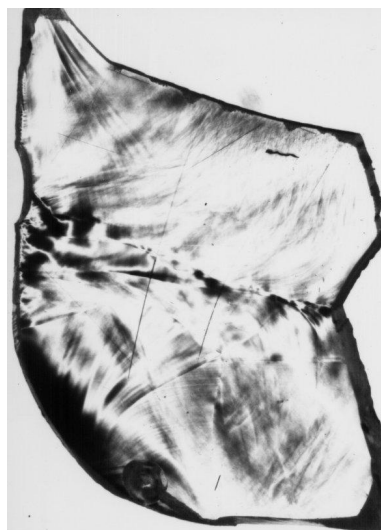
(d) Bridgman-
Er:Sc$_2$O$_3$; width 18 mm

Figure 3.12: Crystals grown by the indicated methods between
crossed polarizers (inverted images)

Figure 3.13: left: HEM-Sc$_2$O$_3$; right: Bridgman-Nd:Y$_2$O$_3$ between crossed polarizers (width 38 mm both; inverted images)

the crystal. This leads to birefringence which can be observed by viewing the crystal between crossed polarizers. The higher the contrasts and the more structured the crystals appear, the stronger is the mechanical stress.
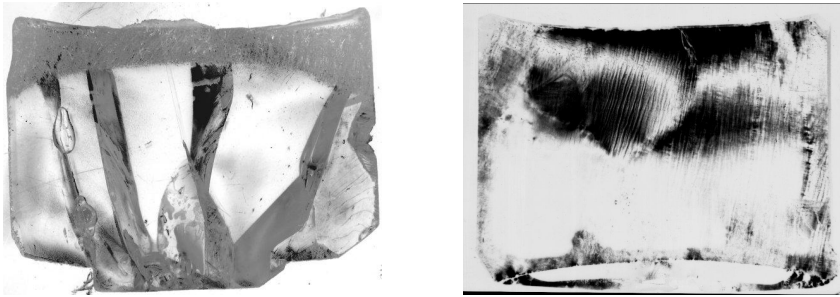
This has severe effects on a laser. Since the induced changes in density are usually highly non-isotropic and variations appear on a micrometer scale, light cannot be transmitted straight through the crystal. Slight deviations from the propagation direction destabilize the resonator and lead to a loss of output power. It is therefore necessary to reduce mechanical stress as much as possible during the growth.

Figures 3.12 and 3.13 show crystals grown by several methods between crossed polarizers. The crystals grown by the Czochralski- and Nacken-Kyropoulos-technique show strong birefringence. It has to be noted that the Nacken-Kyropoulos-crystal was about 3 mm thick, whereas the Czochralski-crystal had a thickness of less than 400 μm. The Nacken-Kyropoulos-crystal is therefore a little better in quality than the Czochralski crystal. As a result the crystal in 3.12(b) showed laser operation in one area near the middle of the crystal with crystal losses of about 3% per round trip [pet98] which is about a factor of 10 to 50 more than in commercially available YAG crystals.

The crystals grown by the Bridgman-method generally exhibit less birefringence than those grown by the Czochralski- and Nacken-Kyropoulos-technique. The undoped scandia crystal in figure 3.12(c) has only very low visible stress. When the crystals are doped, however, stress is induced due to the fact that the dopant usually has a distribution coefficient below unity and is pushed away from the growth interface which leads to striations perpendicular to the growth direction as can be seen in the center of the lower half of figure 3.12(d). In this crystal additional stress was induced by the fact that the the crystal was partly grown from

the bottom and partly from the top. The plane where the two growing crystals touched at the end of the growth process is clearly visible as an area of strong birefringence. Even though the $Er:Sc_2O_3$ crystal grown by the Bridgman-technique does not look better than the crystals grown earlier, there are usually larger areas of good optical quality in crystals grown by this method. The crystal losses per round trip in a laser resonator are typically in the range of 1% for crystals grown by the Bridgman-method.

Figure 3.13 (left) shows the large scandia crystal grown by the HEM-technique without seed (see also figure 3.9(b)). It has to be noted that this crystal was grown within a very short period of only 1 hour. Considering this, the optical quality is excellent. It exhibits only large uniform areas of slowly changing density. Smaller structures can be seen only towards the edges of the crystal. The areas free of birefringence are substantially larger than in crystals grown by the Bridgman-method over periods of several days. Considering the quality of this crystal, the HEM-technique appears to be the most promising method to grow the high melting sesquioxides with high optical qualities.

An example for the problems caused by a phase transition of the crystal is shown in figure 3.13 (right). As mentioned in the introduction to this chapter yttria performs a phase transition from the hexagonal high temperature phase to the cubic room temperature phase slightly below the melting point. The effect on the crystal can clearly be seen between crossed polarizers. The crystal shows very small structures of high contrast which indicate a very low crystal quality.

3.5.4 Impurities

Crystals always contain a certain amount of impurities. These impurities are brought in either by the starting materials or the growth setup, i. e. mostly by the crucible and the insulation materials, less often by the growth atmosphere. It has to be differentiated between impurities that have effects on the spectroscopic properties of the crystal and those that do not. Impurities that have no impact on the spectroscopic properties are usually acceptable as long as they do not interfere with the crystal growth. The other group can be very harmful to a laser system for instance by providing efficient non-radiative decay channels for excitation energy or absorption of the fluorescence light.

Due to its high energy migration rates trivalent ytterbium, especially at high concentrations, is extremely sensitive to luminescence quenching. Studies with $Yb:Sc_2O_3$ and $Yb_3Al_5O_{12}$ have shown the severe effects of small amounts of certain rare-earths and transition metals, divalent Ytterbium (see figure 6.7), and other impurities, which have not been identified yet, on the Yb-fluorescence lifetime and quantum efficiency [bol01, mue01].

The used rare-earth starting materials had a purity of 4N (99.99%) for testing purposes and 5N (99.999%) for growing spectroscopy and laser samples. The given purities refer to the purity among the rare-earths; non-rare-earth impurities may occur up to 1% (weight) in the starting material. All the rare-earth impurities are usually present in roughly the same amounts, varying slightly between production batches [nor96, all99, sta99]. The main non-rare-earth impurities are Ca (20 - 250 ppmw), Cl (20 - 5700 ppmw), Si (10 - 40 ppmw), and Ba (0 - 40 ppmw), all of which have no apparent effect on the ytterbium system. The total effect of the impurities in the starting materials can be seen in the measured lifetime of Yb_2O_3 crystals (see section 6.1.2). The intrinsic lifetime of the ytterbium ion of about 800 µs for low concentrations is shortened to 67 µs for 5N Yb_2O_3.

The rhenium crucibles produced by Heraeus are made from rhenium powder, which contains about 9 ppmw iron, 6 - 20 ppmw molybdenum, and 2 - 3 ppmw chromium [her01]. In the production process tungsten and probably more chromium are added in an unknown amount. Yb_2O_3 crystals grown from these crucibles contain a chromium concentration of 50 - 70 ppmw [koe00]. The lifetime of the Yb-fluorescence is further shortened to about 15 µs. Concerning the galvanically manufactured crucibles made by Engelhard-Clal no data on impurities are available at the present moment. Aside from the impurities in the rhenium source material the manufacturing process probably induces remains of the used galvanic fluxes, which are various salts. Till now tests with $Yb_3Al_5O_{12}$ crystals grown from these crucibles have shown no negative effects, but further tests with Yb_2O_3 and chemical analyses are necessary to evaluate the quality of these crucibles.

The insulation near the crucible is made up of zirconia felt mats produced by Zircar Zirconia, Inc. These consist of zirconia and several substances used to bind the felt and stabilize the mats. A chemical analysis has shown no signs of zirconia incorporation in the crystals grown in the insulation setups described above [koe00]. If zirconia is brought into direct contact with the hot crucible, however, zirconia dissipates into the melt and can be found in the grown crystals [koe00]. As a consequence, zirconia stabilizes divalent ytterbium which leads to a drastic decrease in quantum efficiency in the crystal [mue01].

4

Theoretical Aspects

This chapter will introduce the basic theoretical background for the experiments presented in this work. A generalized look on the field of rare-earth spectroscopy, not including the high-pressure and dimer systems, can be found in the book of Henderson and Imbusch [hen89]. This chapter starts with an introduction to the energy level structure of trivalent rare-earth ions and describes the changes introduced when the ion is placed in a crystal field and when the crystal is brought in a high pressure environment. Also the special case of localized ion pairs in a crystal is introduced. After that the role of lattice vibrations in the rare-earth spectra and the energy transfer processes occurring in the examined crystal systems will be discussed. The special properties of the ytterbium ion will be presented in the last part of this chapter.

4.1   Single Rare-Earth Ions

The term rare-earth (RE) usually refers to the elements lanthanum (atomic no. 57) through lutetium (atomic no. 71) also known as lanthanides and the chemically similar elements scandium (atomic no. 21) and yttrium (atomic no. 39) [gre87]. The following discussion however will only address the lanthanides.

The electron configuration of the lanthanides is $[Xe]^1(4f)^n(5d)^x(6s)^2$ with $x = 1$ in the case of lanthanum ($n = 0$), gadolinium ($n = 7$), and lutetium ($n = 14$) and $x = 0$ and $n = 2$ through $n = 14$ for cerium through ytterbium. In ionic crystals the rare-earths are usually incorporated as stable trivalent ions. The electron configuration for the trivalent lanthanides is $[Xe](4f)^{n+x-1}$. Divalent

---

[1][Xe] represents the electron configuration of the noble gas xenon

rare-earths can appear in crystals with divalent lattice sites. They can also appear if local charge compensation is provided by crystal defects such as F-centers in the sesquioxides and garnets or by the presence of quadrivalent co-dopants in the crystal [kap62, loh69].

The spectroscopic properties of the trivalent rare-earths are dominated by transitions from $4f$ states to $4f$ and $5d$ states. Due to the completely filled $5s$ and $5p$ shell the $4f$ states are well shielded from influences of the crystal field [bur62, ray63, ste66]. This results in a low variation of the $4f$-states in different local environments and narrow transition line-widths compared to those observed in transition metals, divalent rare-earths, and RE^{3+} $5d$-states [hen89]. The strength of the shielding decreases with rising atomic numbers [ste66, erd72].

The radius of the $4f$ wave-function and the radius of the trivalent ion decreases throughout the lanthanide row due to the stronger attraction of the electrons by the nucleus [fre62]. This lanthanide contraction has some effects when the ion is located in a crystal-field. Smaller ions generally are less affected by the crystal-field of a host material than larger ions in the same host due to the larger distance of the main part of the $4f$-wave-function to the electrostatic field of the neighboring ions [blo66, ray63, ste66, erd72].

The $4f$-shielding and the lanthanide contraction influence the strength of the electron-phonon-coupling in the rare-earths. The strength of the electron-phonon-coupling for several rare-earths has been determined by Ellens by measuring the linewidths of electronic transitions and the intensities of vibronic sidebands [ell97, ell97b, ell96]. It is rather strong for the elements in the beginning and the end of the lanthanide row and weaker for those in the middle. Furthermore the effects of hydrostatic pressure decrease through the lanthanide row due to the lanthanide contraction.

4.1.1   The Free Ion

In order to calculate the energy level scheme of the rare-earth ions, the Hamiltonian of the system must be determined and the Schrödinger equation must be solved [mes90]. Since no analytical solution can be found for systems with more than one electron, the system is first reduced to a radial, effective central field without electron-electron interaction in the so-called central-field approximation. The resulting Hamiltonian H_0 is then corrected with additional perturbation terms for the non-radial Coulomb-interaction between the electrons H_{ee} and the spin-orbit coupling of the electrons H_{so}. Further corrections for configurational-, spin-spin-, orbit-orbit-, and hyperfine-interaction are ignored since their influence is small compared to the crystal field interaction which will be introduced later.

In the central-field approximation the Hamiltonian of a N-electron system is

$$H_0 = \sum_{i=1}^{N} \left(-\frac{\hbar^2}{2m_e} \Delta_{r_i} + V(r_i) \right) \tag{4.1}$$

with $(\hbar^2 \Delta_{r_i}/2m_e)$ the kinetic-, and $V(r_i)$ the potential-energy of the ith electron at the distance r_i from the nucleus. This Hamiltonian can be separated and the solution Ψ_0 of the time-independent Schrödinger-equation with the energy-eigenvalues E_0

$$H_0 \Psi_0 = E_0 \Psi_0 \tag{4.2}$$

is the product of the eigenstates of the single-electron wave-functions $|n_i l_i m_l m_s >$:

$$\Psi_0 = \prod_{i=1}^{N} |n_i l_i m_l m_s > . \tag{4.3}$$

n_i denotes the principal quantum number and l_i the orbital angular momentum of the ith electron. The energy-eigenvalues depend only on n_i und l_i. In this model the magnetic-quantum-numbers m_l and spin-quantum-numbers m_s are degenerate.

According to the Pauli-exclusion-principle, the total wave-function Ψ_0 has to be completely anti-symmetric, since two electrons cannot share the same single-particle-state. This can be ensured by building the total-wave-function from single-particle-wave-functions as a Slater-determinant.

A self-consistent central-potential can be determined iteratively by the Hartree-Fock-method. Starting with a chosen potential the calculated potentials converge by successive iteration with the Hartree-Fock-equations towards the self-consistent potential $V(r)$ of the system.

The first perturbation term is the non-radial portion of the Coulomb-interaction H_{ee} between the individual electrons

$$H_{ee} = \sum_{i<j=1}^{N} \frac{e^2}{(4\pi\epsilon_0)|\mathbf{r_i} - \mathbf{r_j}|} - \sum_{i=1}^{N} \left(\frac{Ze^2}{(4\pi\epsilon_0)r_i} - V(r_i) \right) \tag{4.4}$$

with the elementary charge e, the atomic number Z, the vacuum permittivity ϵ_0, and the distance $|\mathbf{r_i} - \mathbf{r_j}|$ between the electrons in question. The influence of the electron-electron-interaction causes a splitting of the $4f^n$-state in distinct LS-levels, where the total orbital angular momentum is $L = |\mathbf{L}|$, with $\mathbf{L} = \sum_i \mathbf{l_i}$,

and $S = |\mathbf{S}|$ is the total spin with $\mathbf{S} = \sum_i \mathbf{s_i}$. The resultant wave-functions are described with the quantum numbers L, S, M_L, and M_S. The energy splitting of the LS-terms is typically in the order of 10^4 cm^{-1}.

The second necessary perturbation term of the central-field approximation is the spin-orbit-interaction

$$H_{so} = -\sum_{i=1}^{N} \frac{1}{2m^2 c_0^2} \cdot \frac{1}{r_i} \cdot \frac{dV(r_i)}{dr_i} \cdot (\mathbf{l_i s_i}). \tag{4.5}$$

c_0 denotes the vacuum speed of light, $\mathbf{l_i}$ the orbital angular momentum, and $\mathbf{s_i}$ the spin-vector.

The further splitting of the energy levels depends on the coupling of the electrons. If the spin-orbit-interaction is weak in comparison to H_{ee}, the LS- or Russel-Saunders-approximation is valid. In this case the total orbital angular momentum and the total spin are coupled to form the total angular momentum $J = L + S$. The influence of the spin-orbit-interaction leads to a splitting of the LS-terms into J-manifolds. In the case of very heavy elements the spin-orbit-interaction is strong and the angular momentums of the electrons $\mathbf{j_i} = \mathbf{l_i} + \mathbf{s_i}$ are coupled together to the total angular momentum $\mathbf{J} = \sum_i \mathbf{j_i}$. In the case of the lanthanides the influence of both perturbation terms is of comparable magnitude. Here the intermediate coupling is valid. The eigenstates are linear combinations of several LS-states of the same total angular momentum J. The state is named after the LS-state with the strongest influence. This leads to the point that different ^{2S+1}L-manifolds can energetically overlap in their J-components. The total angular momentum J, however, remains to be a good quantum number. The eigenstates are designated after the quantum numbers L, S, and J. These $^{2S+1}L_J$-states are $(2J+1)$-fold degenerate in M_J [hen89]. A detailed discussion of the intermediate coupling can be found in the books by Sobelman [sob79] and Condon and Shortley [con51]. The energetic splitting of the $^{2S+1}L_J$-terms is typically in the range of 10^3 cm^{-1}.

4.1.2   Rare-Earth Ions in a Crystal Field

When an ion is incorporated into a crystal lattice it is subject to the electrostatic field of the neighboring ions, also called ligands. The crystal-field potential can be introduced as an additional perturbation term to the free-ion Hamiltonian. In the one-electron approximation the potential can be written as:

$$H_{cf} = \sum_{k,q} B_q^k C_q^{(k)}. \tag{4.6}$$

	Hamiltonian	Interaction	Quantumnumbers	Energy splitting	Degeneracy	Term denotation	ΔE [cm^{-1}]
free-ion	H_0	eff. centr. field potential	n, l, m_l, m_s	n, l	$2(2l+1)$	n, l (s, p, d, f)	$10^4 - 10^5$
	H_{ee}	Coulomb-repulsion of $4f$ elec.	n, L, S, M_L, M_S	$L(S)$	$(2L+1) \times (2S+1)$	^{2S+1}L	10^4
	H_{so}	spin-orbit-coupling	n, L, S, J, M_J	J	$(2J+1)$	$^{2S+1}L_J$	10^3
crystal-ion	H_{cf}	electrostatic field of the ligands	n, L, S, J, M_J	M_J	2-fold Kramers[2]	-	10^2

Table 4.1: Term-splitting of $4f$-electrons in rare-earths

The $C_q^{(k)}$ are tensor operators, whose matrix elements can be calculated exactly, and the crystal-field parameters B_q^k are adjustable parameters [goe96].

The crystal-field has two effects on the energy-level structure of the free-ion: It induces a red-shift on the free-ion levels, which is called nephelauxetic effect and can be explained by a reduction of the free-ion parameters [jor77]. The second effect of the crystal-field on the free-ion is the lifting of the M_j-degeneracy of the $^{2S+1}L_J$-manifolds. This Stark-splitting of the manifolds is usually in the order of some 100 cm^{-1}. According to the Kramers-theorem all levels of every ion with an uneven number of electrons have to be twofold-degenerate. This Kramers-degeneracy is a consequence of the time-reversal invariance and causes the $^{2S+1}L_J$-manifolds of ions with an uneven number of electrons to split only into $(2J+1)/2$ Stark-levels, whereas the manifolds of ions with an even number of electrons are split into $(2J+1)$ levels [mes90].

The crystal-field parameters B_q^k include all the structural information of the local environment of an ion. The superposition model [bra67] makes an attempt to separate intrinsic parameters from the geometrical factors. The one-electron crystal-field parameters are written as:

$$B_q^k = \sum_j \bar{B}_k(R_j)K_{kq}(\vartheta_j, \varphi_j). \tag{4.7}$$

$\bar{B}_k$ is an intrinsic parameter and depends only on the distance R_j and the type of ligand located at $(R_j, \vartheta_j, \varphi_j)$. K_{kq} is a geometrical factor that includes the information about the local environment. Usually only the first ligand shell is used for the calculations, while the influence of higher ligand shells are neglected. This

---

[2]only if n is uneven

model allows an analysis and easier comparison of the crystal-field in similar host materials or monotonically changing local environments, such as crystals under hydrostatic pressure.

4.1.3 The Crystal-Field at High Hydrostatic Pressure

When a crystal is exposed to hydrostatic pressure its volume is decreased according to the isothermal compressibility of the material:

$$\kappa = -\frac{1}{V}\left(\frac{\partial V}{\partial P}\right)_T.$$

(4.8)

This compression causes a shift of the ligands of an active ion, thus changing the crystal-field. In many cases the shift is a symmetric shift of the ligands towards the center ion, that does not affect the symmetry of the system. In some cases, however, the local symmetry is changed or a pressure related phase-transition occurs, which leads to more drastic changes of the optical spectra. A detailed description of the effects of pressure on various systems can be found in the articles by Th. Tröster [tro01] and K. Bray [bra01].

   The first effect of pressure on the crystal-field is the strengthening of the nephelauxetic effect which leads to a further red-shift of the electronic levels. A quantitative study of the nephelauxetic effect in several crystal systems using various theoretical models is given in [tro01].

   The second effect of pressure is the change of the Stark-splitting of the manifolds. In contrast to the nephelauxetic effect, which always induces a red-shift, the Stark-splitting can become both larger and smaller depending on the active ion and the host crystal. This is due to the fact that the Stark-splitting is strongly dependent on the local symmetry of the ligands. If no changes to the local symmetry are induced, the Stark-splitting will become larger with increasing pressure. Other systems, like Pr:LaOCl, show a decrease of the Stark-splitting under pressure, which can be attributed to changes in the local symmetry that lead to an overall decrease of the crystal-field strength even though the interaction strength of the ion with its ligands monotonically increases with pressure [bun98].

   As long as no major geometrical changes are caused by the applied pressure, the pressure induced shift of the ligand-ions towards the active-ion can be described by the dependence on the ligand distance of the superposition model parameter $\bar{B}_k$:

$$\bar{B}_k^L(R^L) = \bar{B}_k^L(R_0^L)\left(\frac{R_0^L}{R^L}\right)^{t_k^L}.$$
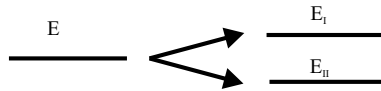
(4.9)

Figure 4.1: Davydov splitting

The parameters $\bar{B}_k^L(R_0^L)$ and t_k^L depend on the system under consideration and R_0^L is an arbitrarily chosen reference distance. The connection between the applied pressure and the change of R^L is given by the compressibility of the material. Structural changes to the system under pressure need to be included in the geometrical factor K_{kq}.

4.2 Dimer Systems

If two ions are placed close to each other in a crystal, additional effects on the spectroscopic properties occur. Due to the overlap of the electron-wave functions of the optically active electron shells the two ions form a pair that needs to be treated as a single dimer system or molecule in terms of quantum mechanics. The main cause for this behaviour is the Coulomb-interaction of the electrons of the two ions, referred to as exchange interaction. A theoretical and experimental study of dimer systems can be found in [ovs87].

4.2.1 Exchange- and Super-Exchange-Coupling

When two atoms or ions are brought close together and their electron shells overlap, electrons can be exchanged between the two atoms. Since the wave functions of the coupled atom system need to fulfill Pauli's exclusion principle, the two single atoms cannot have identical energy levels. The coupled system shows a splitting of all single atom energy levels into two levels E_I and E_{II} (Davydov-Splitting, see figure 4.1) [mor65]:

$$E_I = A^2(K_{12} + J_{12}) \qquad \text{and} \qquad E_{II} = B^2(K_{12} - J_{12}) \qquad (4.10)$$

with the average Coulomb interaction energy (in the case of a H_2 molecule):

$$K_{12} = \int \Phi_a{}^*(1)\Phi_b{}^*(2)H_{12}\Phi_a(1)\Phi_b(2)d\tau_1 d\tau_2 \qquad (4.11)$$

and the exchange integral:

$$J_{12} = \int \Phi_a{}^*(1)\Phi_b{}^*(2)H_{12}\Phi_a(2)\Phi_b(1)d\tau_1 d\tau_2. \qquad (4.12)$$

A and B are normalizing factors, Φ_a and Φ_b are the wave functions of the hydrogen atoms. The integration is performed over the relevant volume. The Hamiltonian for the H_2 molecule is given by:

$$H_{12} = \frac{e^2}{r_{ab}} + \frac{e^2}{r_{12}} - \frac{e^2}{r_{1b}} - \frac{e^2}{r_{2a}},$$
(4.13)

where r_{ab} is the distance between the nuclei, r_{12} is the distance between the electrons, and r_{1b} and r_{2a} are the distances between a nucleus and the electron of the other atom.

In crystals there is more than one exchange-interaction partner. In order to calculate the average exchange integral of an ion $\bar{J}$ the data from all ligands have to be averaged:

$$\bar{J} = \frac{\sum_j z_j J_{ij}}{\sum_j z_j}$$
(4.14)

with the number z_j of j-type neighbors of the ion i with the exchange integral J_{ij}.

For two atoms with more than one electron and one unpaired electron each, the total exchange Hamiltonian can be written in its spin dependent form:

$$H_{ex} = -2J_{ij}\mathbf{S}_i \cdot \mathbf{S}_j$$
(4.15)

with the total spins of the atoms $\mathbf{S}_i = \sum_i \mathbf{s}_i$ and $\mathbf{S}_j = \sum_j \mathbf{s}_j$. In this equation two assumptions have been made:

- all electrons have the same exchange integral, which is reasonable in crystalline environments, and

- the exchange energy between electrons of the same atom can be omitted

The total value of the exchange interaction on an atom i is given by a summation of the exchange interaction with the neighboring ions in the crystal:

$$H_{ex} = -2\sum_j J_{ij}\mathbf{S}_i \cdot \mathbf{S}_j,$$
(4.16)

If the value of $\bar{J}$ is positive, the crystal is likely to show ferromagnetic behaviour. However, some crystals with positive values of $\bar{J}$, like Er_2O_3 and Yb_2O_3, show antiferromagnetic behaviour. This is caused by indirect exchange interaction through the ligands, in this case oxygen. The strength of this indirect exchange interaction, also known as super-exchange-interaction, depends strongly on the ligand distances and positions. Several models to estimate the super-exchange-interaction can be found in the book of A. Morrish [mor65].

4.2.2 Calculation of the Davydov-Splitting

Since a direct calculation of the exchange interaction involves a huge computational effort there are several methods to estimate the amount of the Davydov-splitting in a crystal [mor65, zie69, zie71]:

- **Molecular-field approximation for the Neel-temperature**
  The Neel-temperature[3] T_N and the average exchange interaction (in cm^{-1}) are connected by:

$$\bar{J} = \frac{3T_N}{zS(S+1)} \tag{4.17}$$

  with the spin S of the atomic state and the number of nearest neighbors z. The molecular-field approximation using the Neel-temperature generally gives too low values for $\bar{J}$.

- **Molecular-field approximation for the Curie-Weiss-temperature**
  The approximation of the average exchange interaction with the Curie-Weiss-temperature[4] θ is more exact than that with the Neel-temperature:

$$\bar{J} = \frac{3\theta}{zS(S+1)} \tag{4.18}$$

  The Neel-temperature is related to the Curie-Weiss-temperature by $\theta/T_N \approx$ 1.1 to 1.5 for simple antiferromagnets. For some materials higher ratios have been measured.

- **Series-expansion-method**
  The series expansion method introduced by Rushbrooke and Wood generally gives the most accurate estimate for the exchange interaction. For cubic antiferromagnets the average exchange interaction is given by:

$$\bar{J} = \frac{192T_N}{5(z-1)[11S(S+1)-1]\left[1-\frac{0.63}{zS(S+1)}\right]} \tag{4.19}$$

The splitting of the energy levels can be as large as several hundred cm^{-1} in transition metals and is generally much smaller in rare-earth components by more than one order of magnitude.

---

[3]The temperature at which antiferromagnetic ordering of the spins occurs.
[4]The temperature at which ferromagnetic ordering of the spins occurs.

$[^5/_2(z),^5/_2(z')]$ —— $[^5/_2(z),^5/_2(z')]$ —— $[^5/_2(z),^5/_2(z')]$ ——

$[^7/_2(y),^5/_2(y')]$ —— $[^7/_2(y),^5/_2(y')]$ —— $[^7/_2(y),^5/_2(y')]$ ——

$[^7/_2(x),^7/_2(x')]$ —— $[^7/_2(x),^7/_2(x')]$ —— $[^7/_2(x),^7/_2(x')]$ ——

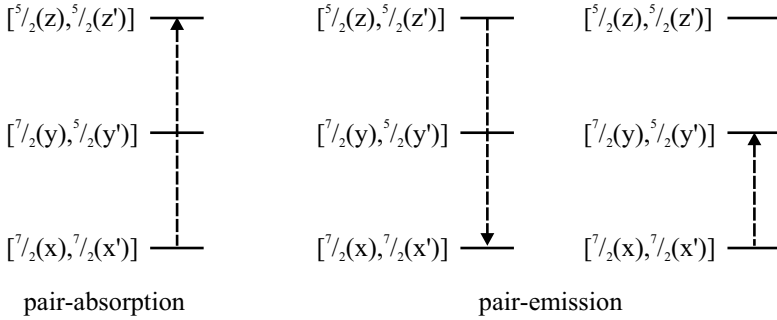pair-absorption   pair-emission

Figure 4.2: Cooperative transitions in ytterbium

4.2.3   Cooperative Optical Transitions

A second impact of exchange-coupling on ion-spectra is the existence of cooperative optical transitions, that is simultaneous absorption or emission of one photon by two coupled ions (see figure 4.2). The resulting absorption and emission energies are the added energy differences of the two single ions. The first report of cooperative transitions has been published by Varsanyi and Dieke in Pr:LaCl$_3$ [var61]. Cooperative emission of Yb-dimers in the green spectral range was first observed by Nakazawa in YbPO$_4$ [nak70]. Since then, cooperative processes have been studied in numerous Yb-compounds [sch75, heh93, gol97a, gol97b] and transition-metal systems [kis69, val00, hee01].

Cooperative transitions in ytterbium systems are mainly observable as a weak emission in the green spectral range at the half emission wavelength of the infrared emission. In this case both ions of the dimer are in their excited state and emit one photon while simultaneously changing to the ground state $\left[\frac{5}{2}(x'),\frac{5}{2}(x)\right] \rightarrow \left[\frac{7}{2}(y'),\frac{7}{2}(y)\right]$ (x, x', y, and y' denote an arbitrary Stark-level of the manifold). The same process appears in absorption when the dimer absorbs one high energetic photon and both coupled ions are switched to their excited state. The cooperative transitions are weaker than the infrared transitions by a factor of 10^3 - 10^4, depending on the material. Furthermore, cooperative emission in the infrared has also been observed [heh93]. Here one of the ions is in its excited state and the other is in a higher Stark-level of the ground state . This can create slightly shifted, weak mirror images of the infrared emission $\left[\frac{7}{2}(x'),\frac{5}{2}(x)\right] \rightarrow \left[\frac{7}{2}(y'),\frac{7}{2}(y)\right]$.

The oscillator strength of the cooperative transitions is proportional to the exchange- and super-exchange-interaction of the coupled ions. Theoretical calculations of the oscillator strengths have only been published for Yb:CsCdBr$_3$

[gol97a]. Here, ytterbium ions can only fit into the $CsCdBr_3$-lattice if two ytterbium ions replace three cadmium ions. Therefore all Yb-ions in the crystal form pairs of well defined nearest neighbor distances. Calculations for other materials with statistical dopant distributions would involve the calculation of all possible nearest neighbor combinations, numbers, interaction distances, and statistical probabilities, which has not been accomplished up to now.

Notable is also that the intensity of vibronic sidebands is reduced by a factor of up to 20 in the cooperative ytterbium transitions compared to the sidebands of single-ion transitions at low temperatures. Hehlen et al. have offered an explanation for this phonon selection effect [heh93]: A vibronic excitation of a pair $\left[\frac{7}{2}(0), \frac{7}{2}(0')\right] \rightarrow \left[\frac{5}{2}(y), \frac{7}{2}(y')\right]$ is immediately followed by a non-radiative transfer to the lowest Stark-level of the $\left[\frac{5}{2}, \frac{7}{2}\right]$-multiplet $\left[\frac{5}{2}(0'), \frac{7}{2}(0)\right]$. Due to the slightly different vibrational energies in the ground- and excited-state a different excitation energy would be needed to excite the analogous vibronic excitation for the second ion $\left[\frac{5}{2}(0), \frac{7}{2}(0')\right] \rightarrow \left[\frac{5}{2}(y), \frac{5}{2}(y')\right]$ and therefore the rate of vibronic pair-transitions is lowered.

4.3   Interaction with the Lattice

As mentioned earlier, the electron-phonon-coupling in ytterbium is one of the strongest in the lanthanide series. Therefore, the strength an influence of phononic features in the optical spectra is very high compared to other rare-earths. The effects of the electron-phonon-coupling will be introduced in this section.

4.3.1   Line-Broadening

Several mechanisms lead to a line-broadening of the rare-earth transitions. The broadening of an energy level can be written as:

$$\Delta E_{phon} = \Delta E^D(T) + \Delta E^R(T) + \Delta E^{Orb}(T) + \Delta E^{MR}(T) + \Delta E^{Rad}.$$

(4.20)

The natural linewidth ΔE^{Rad}, the broadening by multi-phonon-relaxation ΔE^{MR}, and the broadening by the ΔE^{Orb} the Orbach-process, a resonant two-phonon-process, can usually be neglected [yen64, kus67, kus69, ell97]. Furthermore the temperature dependent inhomogeneous line-broadening as well as the broadening by local distortions of the crystal lattice are not taken into account. The two remaining terms are mainly responsible for the temperature dependence of the linewidth: ΔE^D describes the influence of the direct single-phonon absorption and emission. ΔE^R is due to the two-phonon Raman-process. First the state i absorbs a phonon and reaches a virtual state j'. Then a phonon of different energy is emitted and the atom reaches the state j. The energy of the absorbed and emitted phonons is considered to be large compared to the energy difference between the states i and j.

At room temperature the linewidth of rare-earths is typically in the order of several cm^{-1} due to these processes.

4.3.2   Vibronic Sidebands

Most trivalent rare-earths show nearly exclusively pure electronic to electronic transitions. Transitions of coupled electronic and vibrational states (vibronic states) are usually very weak. Some rare-earth ions, like the ytterbium ion, however, show a stronger coupling between electronic and phononic states which leads to the formation of vibronic sidebands with transition strengths comparable to those of purely electronic transitions. A detailed theoretical analysis of electron-phonon interaction in rare-earths can be found in [ovs87].

Since the electron-phonon coupling can still be considered small, the interaction of an ion with lattice phonons can be described by a perturbation term to the
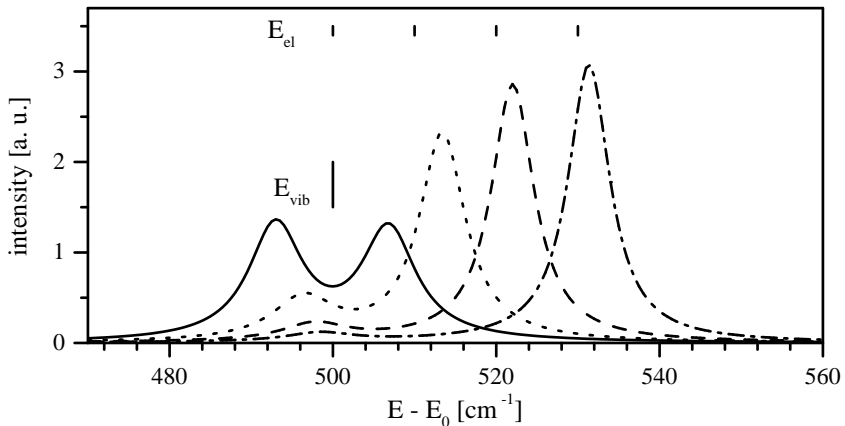
Figure 4.3: Calculation of the coupling between a vibronic side-
band at 500 cm^{-1} and an electronic line. The shape of
transitions from another level to the coupled electronic-
vibronic-state depends on the energy separation between
the vibronic and electronic line $\Delta E = E_{vib} - E_{el}$.
The symmetric double structure appears for $\Delta E = 0$.
For larger ΔE the influence of the coupling between
the electronic- and vibronic-line becomes weaker and the
lines show as separated features [mix99].

free-ion Hamiltonian [hak73]:

$$H_{el-ph} = \sum_{\alpha, \mathbf{q}, \xi} e\left[V(\mathbf{r}_\alpha, \mathbf{q}, \xi) \cdot a_{\mathbf{q}\xi} + V^*(\mathbf{r}_\alpha, \mathbf{q}, \xi) \cdot a_{\mathbf{q}\xi}^t\right], \qquad (4.21)$$

with the wave-vector $\mathbf{q}$ and branch ξ of the phonon and the construction and
destruction-operator of the phonons a and a^t. $\mathbf{r}_\alpha$ is the position of the $4f$ elec-
tron α.

A quantitative modeling of the vibronic sidebands is possible if the complete
phonon-dispersion relation of a system is known [hur72, ign96, lup99].

4.3.3　Coupling of Vibronic and Electronic Levels

Most studies treat vibronic sidebands of transitions as isolated from other elec-
tronic levels. If vibronic sidebands overlap with neighboring electronic levels, the
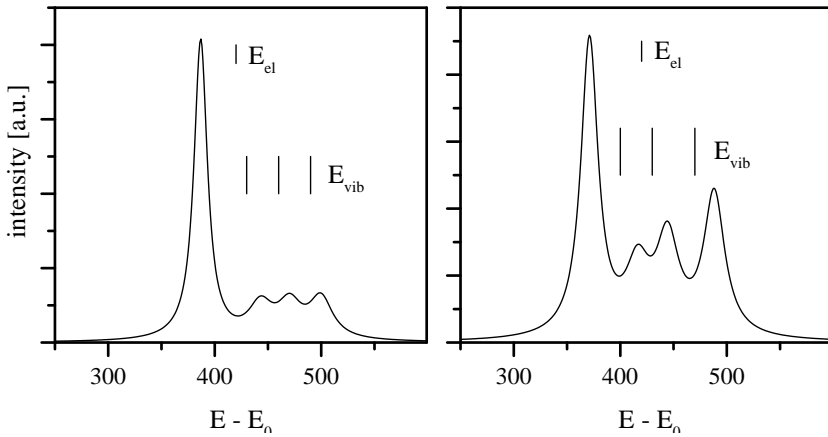
Figure 4.4: Calculation of the coupling between an electronic level
at 420 cm^{-1} and three vibronic sidebands. The resulting
structures are similar to those found in the low tempera-
ture spectra in section 6.2.1.

coupling between the sideband and the level can lead to a deformation or splitting
of the transition [del94, lup97, lup99, mal95].

Figure 4.3 shows the shape of a transition from an electronic level to a coupled
electronic-vibronic state for several energy differences between the coupled lines.
The calculation was performed using the algorithm shown in appendix C. The
larger the energy difference, the smaller the effect of the coupling. In the case that
the coupling electronic and vibronic states have the same energy, the transition
takes the shape of a symmetric double structure with no peak at the position of the
original electronic line.

In case of ytterbium a coupling between the vibronic sidebands and electronic
transitions is very probable. The impact on the Yb^{3+}-spectrum can be modeled if
the complete phonon dispersion curves are known and the vibronic sidebands can
be calculated. Lupei et al. have modeled the coupled electronic-vibronic spectra
for ytterbium-doped YAG, LiNbO$_3$, and YLF with the success of being able to
unambiguously identify the electronic Stark-levels of the ^{2}F$_{5/2}$-state [lup99].

In figure 4.4 the coupling between an electronic level at 420 cm^{-1} and three
vibronic levels is displayed. It is notable that the strongest peak does not appear at
the position of either of the levels but shifted away from the coupled levels. Fea-
tures like this can be seen in many low temperature spectra of the ytterbium-doped

sesquioxides. The data on vibronic transitions in the sesquioxides is unfortunately
not sufficient for quantitative modelling of the actual structures found in the spec-
tra.

4.4   Energy Transfer

4.4.1   Intraionic Processes

Intraionic processes are those in which one ion or a coupled ion-pair interacts with
photons or phonons. Interactions with photons are called radiative transitions,
those with phonons non-radiative transitions.

Radiative Transitions

Absorption, stimulated and spontaneous emission:

The basic radiative transitions are ground-state absorption (GSA), stimulated
emission, and spontaneous emission. They were described by Einstein using the
coefficients B_{ji} (absorption), B_{ij} (emission), and A_{ij} (spontaneous emission)
[ein16, ein17]. In thermal equilibrium the population of the energy levels of a
system follows the Boltzmann statistics:

$$N_j = N_i \cdot e^{\frac{E_i - E_j}{kT}} \tag{4.22}$$

with the temperature T and the population densities $N_{i,j}$ and the energies $E_{i,j}$ of
the levels i and j. By comparing coefficients to Planck's radiation law:

$$E(\nu) = \frac{8\pi h \nu^3}{c^3} \frac{1}{e^{\frac{h\nu}{kT}} - 1} \tag{4.23}$$

the Einstein-relations can be deduced:

$$B_{ij} = \frac{g_j}{g_i} B_{ji} \tag{4.24}$$

with the degeneracy level $g_{i/j}$ of the state $|i/j>$ and

$$\frac{A_{ij}}{B_{ij}} = \frac{8\pi h n^3 \nu^3}{c_0^3} \tag{4.25}$$

with the frequency

$$\nu = \frac{E_i - E_j}{h}.$$ (4.26)

n is the refractive index of the material and $E_{i/j}$ is the energy of the state $|i/j>$. The transition cross section σ_{ji} is given by:

$$\sigma_{ji} = \frac{2\pi^2 \nu}{3n\epsilon_0 c_0 h} \cdot |\mu_{ji}|^2 = B_{ji} \cdot \frac{nh\nu}{c}$$ (4.27)

with the dipole-matrix element μ_{ji} and the speed of light within the material c [sve93].

The radiative lifetime τ_{rad} of an excited state $|i>$ is defined as the reciprocal of the sum of the spontaneous radiative transition rates to all energetically lower levels $|j>$:

$$\tau_{rad}(|i>) = \frac{1}{\sum_j A_{ij}}.$$ (4.28)

The branching ratio β_{ij} determines the percentage, that one transition $|i> \rightarrow |j>$ takes up of the entire transition rate from a state $|i>$:

$$\beta_{ij} = \frac{A_{ij}}{\sum_k A_{ik}}.$$ (4.29)

Excited-state-absorption (ESA):

Absorption from excited states is analogous to the ground state absorption. ESA can be positive or negative for the laser properties of a system. Excited state absorption from the upper laser level can lead to a depopulation of this level and therefore lower the laser efficiency. On the other hand ESA can be used to populate energy levels of higher energy than the pump light and allow laser operation from those levels.

In the ytterbium-system ESA can only occur to the conduction band, to charge transfer states, or in coupled ytterbium-impurity pairs. Strong $4f$-$4f$ ESA as in other rare-earths cannot occur due to the simple energy level structure.

Reabsorption:

If a photon that has been emitted is absorbed again by the same activator type the process is called reabsorption. Reabsorption can become a significant process

if the overlap of the absorption and emission is large. In the case of ground state lasers, reabsorption is a well-known loss process. Furthermore it can prolong the measured lifetime of an excited state compared to the real lifetime of the level, the so-called radiation trapping. With ytterbium-doped YAG, lifetimes up to 50% higher than the radiative lifetime could be measured depending on the used setup [sum94, bol01].

Non-Radiative Transitions

Multi-phonon-relaxation is the transition of an excited state into a lower one by interaction with one or more lattice phonons. The excitation energy is directly transformed into heat by this process. Multi-phonon relaxation into energetically close levels is very fast and can efficiently depopulate excited states. The temperature dependent non-radiative transition rate W_{nr} is described by [moo70]:

$$W_{nr}(T) = W_0 \cdot e^{-a\Delta E} \left[1 - e^{\frac{\hbar\omega_{\text{eff}}}{kT}}\right]^{-p}.$$ (4.30)

The empirical parameter W_0 depends on the host material and a describes the electron-phonon coupling, which can be considered weak in the case of $4f$ electrons. ΔE is the energy difference between the two states and $\hbar\omega_{\text{eff}}$ is the effective phonon energy of the host material. The number of phonons needed to bridge the energy gap is given by $p = \frac{\Delta E}{\hbar\omega_{\text{eff}}}$. Usually, the temperature dependence of $\hbar\omega_{\text{eff}} > kT$ can be neglected in the case of ytterbium.

The non-radiative lifetime of an excited state is defined as

$$\tau_{nr} = \frac{1}{W_{nr}}.$$ (4.31)

The fluorescence lifetime can now be calculated from the radiative (eq. 4.28) and non-radiative lifetime:

$$\frac{1}{\tau} = \frac{1}{\tau_{rad}} + \frac{1}{\tau_{nr}}.$$ (4.32)

The fluorescence lifetime can be determined experimentally from the decay of the fluorescence intensity I, which is single exponential in the most simple case:

$$I(t) = I(0) \cdot e^{\frac{-t}{\tau}}.$$ (4.33)

4.4.2 Selection Rules for Radiative Transitions

The radiative transitions in the trivalent lanthanides occur mainly between $4f^n$-states. Since the start- and end-state of these transitions have the same parity,

electric-dipole transitions are forbidden by the Laporte selection rule and only magnetic dipole transitions can occur [hen89]. Magnetic dipole transitions are generally weaker than electric dipole transitions by a factor of 10^5. Under the influence of a non-inversion-symmetric crystal field, however, configurational mixing between $4f$ and opposite parity states like $4f^{n-1}5d$-states partly allow electric dipole transitions between $4f$-sates in the lanthanides [vle37]. In the case of crystallographic sites with inversion symmetry the Laporte selection rule can be weakened by non-centric distortions like lattice defects. In general the weakening for sites with inversion symmetry is still considerably smaller than the weakening for non-inversion sites.

The general selection rules for electric dipole transitions can be summarized as follows [kam90, hen89]:

1. $\Delta l = \pm 1$,

2. $|\Delta S| = 0$

3. $|\Delta L| \leq 2l = 6$

4. $|\Delta J| \leq 2l = 6$

In the case of rare-earth ions with an even number of electrons some additional selection rules apply:

- $J = 0 \leftrightarrow J' = 0$ is forbidden

- $J = 0 \leftrightarrow J' = 2, 4, 6$ should be strong

- $J = 0 \leftrightarrow J'$ uneven should be weak

The mixing of $4f$- and opposite-parity-states and the resulting transition rates have been calculated by Judd and Ofelt [jud62, ofe62]. The transitional-matrix-elements μ_{ji} and the Judd-Ofelt-parameters Ω_j can be determined from measurements of the oscillator strengths of several ground state transitions. With these parameters the oscillator strengths of the remaining transitions can be calculated with an accuracy of about 20%. In the case of the Yb-ion this method can not be successfully applied, since the transitions from the only existing excited state are not sufficient to determine all the necessary parameters [mix99].

4.4.3   Interionic Processes

Interionic processes involve the direct transfer of excitation energy between two ions without absorption or emission of photons. The involved ions are coupled through multipolar-, exchange-, or super-exchange-interaction.
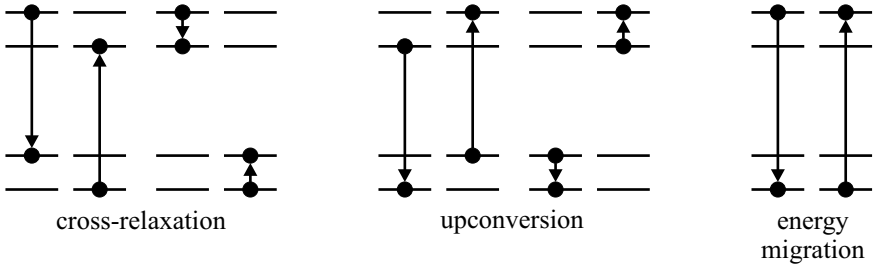
Figure 4.5: Interionic processes

Förster and Dexter have developed a model to describe energy transfer on the basis of multipolar- and exchange-interaction [foe48, dex53]. In the case of low dopant concentrations the transition probability for an electric-dipole-interaction is given by:

$$
\begin{aligned}
W_{DA,ed} &= \frac{3\hbar^4 c_0^4}{4\pi n^4 R_{DA}^6 \tau_{rad,D}} \cdot \int \sigma_{abs,A}(E)dE \cdot \int \frac{f_{em,D}(E) \cdot f_{abs,A}(E)}{E^4} dE \\
&\equiv \frac{C_{DA}}{R_{DA}^6}
\end{aligned}
$$

$$(4.34)$$

with the vacuum speed of light c_0, the refractive index n, the distance between donor and acceptor R_{DA}, the radiative lifetime of the donor $\tau_{rad,D}$, the absorption cross section of the acceptor $\sigma_{abs,A}$, and the normalized line shapes of the emission line of the donor and the absorption line of the acceptor f. The micro-parameter C_{DA} is a measure for the efficiency of the transfer process.

More detailed information on energy transfer processes is given in the books of B. Henderson and G. F. Imbusch [hen89] as well as R. Reisfeld and C. K. Jørgensen [rei77]. A study of energy transfer processes in ytterbium-doped scandia can be found in the work of A. Bolz [bol01].

The different types of energy transfer processes (see figure 4.5) will be described in the following:

Cross-Relaxation

Cross-relaxation is the full or partial transfer of excitation energy to an acceptor in a lower level. This process can be very efficient, if the energy differences in the participating donor and acceptor levels are resonant or the energy needed to excite

the acceptor is slightly smaller than the energy provided by the donor. Cross-relaxation is often used to sensitize ions with small absorption cross section by co-doping with ions with strong absorption, like ytterbium, to achieve a more efficient excitation.

Upconversion

Upconversion is similar to cross relaxation except that the acceptor is initially in an excited state. The resulting excitation energy of the acceptor is higher than the original excitation energy of the donor. This process allows the realization of lasers with a shorter emission- than pump-wavelength [joh71].

Energy-Migration

Energy migration is the resonant energy transfer between two ions of the same type. This process allows the excitation energy to quickly spread out and therefore raises the probability of the other energy transfer processes. Energy migration is described by several models depending on the ratio of transfer rates between two donors C_{DD} and between donor and acceptor C_{DA}. Right after the excitation a fast migration of the excitation energy between donors occurs [vor82]. After this first, fast migration to neighboring ions, the further spreading of energy can be either described by the diffusion-model in the case that C_{DD} is much smaller than C_{DA} [yok67] or the hopping-model for C_{DD} larger than C_{DA} [bur72].

Due to the strong dependence of the transition probabilities on the distance between donor and acceptor, the energy transfer processes become most important at high doping levels. This can be very useful if energy transfer is desired as in sensitized systems or can be harmful if the excitation energy is transferred away from the active ion to unwanted impurities. In the case of highly doped ytterbium systems, energy transfer to such impurities can cause a nearly complete quenching of the excitation energy and therefore make laser operation impossible. The energy quenching of $Yb_3Al_5O_{12}$ and $Yb:RE_2O_3$ has been investigated in the works of V. Müller and A. Bolz [mue01, bol01].

4.5   Trivalent Ytterbium as Active Ion

Ytterbium is the second heaviest element of the lanthanide series and has the atomic number 70. The atomic weight of the natural isotope mixture is 174.04 $\frac{g}{mol}$ [roe92]. The metal has a gray color and is easily workable. Its melting point is 819 C, and its evaporation point is 1196 C. In nature ytterbium is usually found in
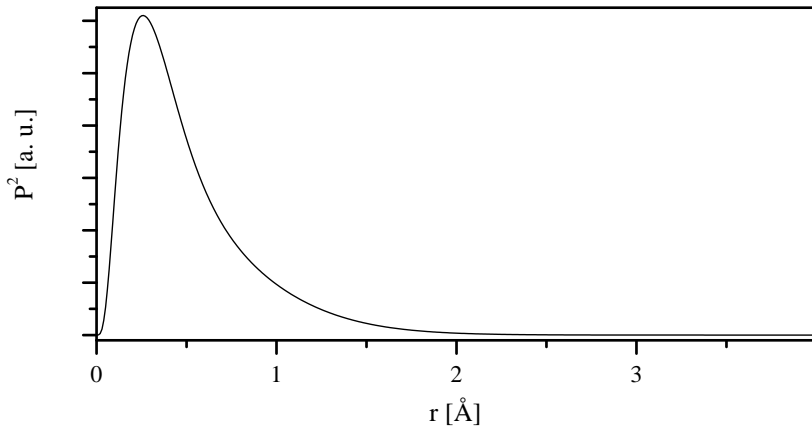
Figure 4.6: P^2 of the $4f$ wave-function of trivalent ytterbium in the Hartree-Fock approximation [fre62].

minerals as a trivalent ion but can also occur in divalent form. It has been named after the village Ytterby, near Stockholm, where it has first been discovered by Marignac in 1878.

The electronic configuration of the ytterbium atom is $[Xe]4f^{14}6s^2$, of the trivalent ion $[Xe]4f^{13}$ in which case the $4f$-shell can be treated as a closed shell with one hole. The radius of the trivalent ion is between 0.87 and 1.2 Å depending on the coordination of the surrounding lattice. There are two $4f$-states, the ground-state $^2F_{7/2}$ which is split into four Stark-levels and the excited state $^2F_{5/2}$ which is split into three Stark-levels. The wave-function of the $4f$-electrons has been approximated by the Hartree-Fock method by Freeman and Watson to the fourth order [fre62]. It can be calculated by the following equation (see figure 4.6):

$$P_{4f}(r) \equiv \sum_{i=1}^{4} C_i r^4 e^{-Z_i r} \qquad (4.35)$$

with the normalization condition

$$\int_0^\infty P_{4f}{}^2(r)dr = 1. \qquad (4.36)$$

r is used in units of the Bohr radius. The eigenfunctions C_i and exponential parameters Z_i for the ytterbium $4f$-wave-function are

- C_i: 3914.4363, 790.99957, 90.998364, 4.8064115

lower Stark-level	upper Stark-level	reference
0, 140, 590, 620	10336+: 0, 291, 593	[woo63]
0, 611, 696, 782	10321+: 0, 299, 306	[buc67]
0, 388, 613, 776	10324+: 0, 310, 586	[kon65]
0, 565, 612, 785	10327+: 0, 316, 358	[bog76]
0, 584, 635, 783	10328+: 0, 424, 589	[bog77]
-	10327+: 0, 319, 587	[lup99]

Table 4.2: Different sets of Stark-levels for Yb:YAG

- Z_i: 15.287, 8.501, 5.667, 3.126.

As described earlier in this chapter, ytterbium exhibits a strong electron-phonon coupling. This is the reason for the large linewidths and strong vibronic sidebands in the spectra. The identification of the Stark-levels from low temperature spectra is complicated by the overlap and the coupling of vibronic sidebands and electronic lines. Crystal-field calculations cannot be accurately performed since the number of electronic levels is too small to fit all available parameters. Due to these effects the determination of the electronic structure of the ytterbium ion is rather complicated. Most of the work on this matter has been done with Yb:YAG. The different values published in literature are shown in table 4.2. The latest results by Lupei et al. [lup99] were obtained by taking into account the electronic-vibronic coupling in the ytterbium-spectra and appear to be conclusive. The different published sets of Stark-levels lead to an uncertainty in the calculation of the emission cross sections of the ytterbium ion, which are a vital part in the simulation of the laser capabilities of a system. From the published sets a statistical standard deviation for the emission cross sections of Yb:YAG can be calculated to be about 20% [mix99].

5

Spectroscopic Methods

5.1 Absorption Measurements

The intensity I of light passing through an absorbing medium of the length d decreases according to Lambert-Beer's law:

$$I(\lambda) = I_0(\lambda)e^{-\alpha(\lambda)d}.$$ (5.1)

α is called absorption coefficient and I_0 is the reference intensity in front of the absorbing medium. This equation is valid as long as α does not depend on the intensity, which is given at low excitation intensities.

The absorption coefficient α can be calculated from the transmitted intensity of the medium $I(\lambda)$ and the reference intensity of the measurements setup $I_0(\lambda)$:

$$\alpha(\lambda) = \frac{\ln(I_0(\lambda)/I(\lambda))}{d}.$$ (5.2)

The effective absorption cross-section σ_{abs} can then be determined using the dopant concentration n_d:

$$\sigma_{abs}(\lambda) = \frac{\alpha(\lambda)}{n_d}.$$ (5.3)

The ground-state-absorption measurements at room temperature were performed using a dual-beam Varian Cary 2400 photo-spectrometer with a wavelength range of 180 - 3000 nm. In case of the low temperature measurements a halogen lamp was used as light source and a $^1/_2$ m-Czerny-Turner-grating-monochromator with a silicon detector or photomultiplier with S1 characteristic
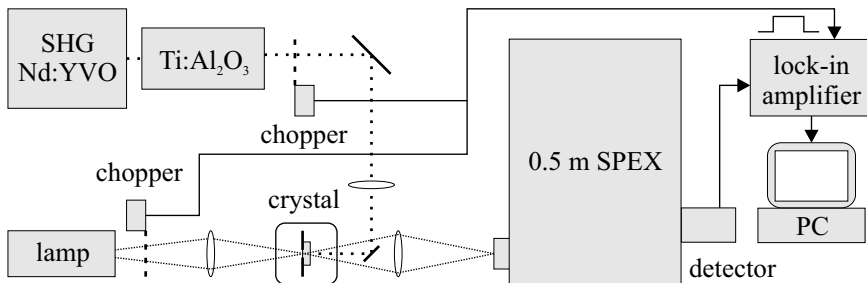
Figure 5.1: Setup for absorption, excitation, and emission measurements

were used for detection. The setup is depicted in figure 5.1. The low temperature absorption measurements were performed at a sample temperature of 10 - 15 K, achieved with a closed cycle helium cryostat, using low excitation intensities to avoid heating of the sample. In oder to reduce the wavelength deviation of the spectrometer, the low temperature measurements were performed with an additional mercury vapor lamp in the optical path. The correct wavelengths were calculated afterwards using the exactly known, sharp transitions of the vapor lamp. By this method a wavelength accuracy of better than 1 Å was reached.

5.2   Excitation Measurements

In contrast to absorption measurements, excitation measurements can distinguish between different luminescence centers. In an excitation measurement the detection wavelength is set to a luminescence line of the center that is to be observed and the excitation wavelengths is slowly shifted through a certain wavelength range. Unless several luminescence centers or non-emitting centers are present in a medium the excitation measurement will produce the same results as an absorption measurement. Excitation measurements are especially interesting if the absorption of a weak center, such as ytterbium ions in C_{3i}-sites of the sesquioxides, are superimposed by a stronger absorption of another center or if the absorption is too weak to be detected in transmission. Centers that do not decay radiatively cannot be accessed by this method.

The setup used for the excitation measurements presented in this work is shown in figure 5.1. As excitation source a titanium sapphire laser with a tuning range of 850 - 1000 nm and a maximum output power of 2 W was used.

5.3 Emission Measurements

The fluorescence of the samples was analyzed using a $^1/_2$ m-monochromator and a silicon-detector or an S1-photomultiplier for detection. As excitation source a titanium-sapphire laser was used (see figure 5.1). The measured intensity I_{sample} has to be calibrated with the measured spectrum of a tungsten lamp I_W operating at the temperature T_{cal} to eliminate the spectral response function of the used setup from the spectra. The calibrated emission spectrum can be calculated with the known emissivity of tungsten $\epsilon_W(T_{cal})$ and the calculated radiation intensity $I_{Planck}(T_{cal})$ of a black-body:

$$I(\lambda) = \frac{I_{sample}(\lambda) \cdot I_{Planck}(\lambda, T_{cal}) \cdot \epsilon_W(T_{cal})}{I_W(\lambda, T_{cal})} \qquad (5.4)$$

The corresponding emission cross-sections σ_{se} can be calculated from the absorption as well as from the emission spectra:

From the GSA spectra only the cross-sections for transitions to the ground state can be determined. The calculation of the emission cross-sections follows the reciprocity method [mcc64, pay92]. The effective absorption and emission cross-sections σ_{abs} and σ_{se} of a transition between identical Stark-levels are correlated with the atomic cross-sections σ_{at} through the Boltzmann-factors $f_{l,u}$:

$$\sigma_{abs} = f_l \sigma_{at}, \qquad \sigma_{se} = f_u \sigma_{at} \qquad \Longrightarrow \qquad \sigma_{se} = \frac{f_u}{f_l} \sigma_{abs} \qquad (5.5)$$

with the Boltzmann-factors f_l and f_u of the lower and upper level, respectively:

$$f_{l/u} = \frac{g_{l/u} \cdot e^{-(E_{l/u} - E_{zl,multi,l/u})/(kT)}}{Z_{multi,l/u}} \qquad (5.6)$$

with $Z_{multi,l/u}$, partition function of lower and upper level, respectively defined as:

$$Z_{multi,l/u} = \sum_k g_k \cdot e^{-(E_k - E_{zl,multi,l/u})/(kT)}, \qquad (5.7)$$

and the degeneracy $g_{l,u}$ of the Stark-levels (see chapter 4.1.2), $E_{l,u}$ the energy of the Stark-levels, $E_{zl,multi,l/u}$ the energy of the lowest Stark-levels of the manifolds, and the partition function of the manifold $Z_{multi,l/u}$. By combining 5.5 and 5.6 the emission cross-section can be correlated to the absorption cross-section:

$$\sigma_{se}(\nu) = \sigma_{abs}(\nu) \cdot \frac{Z_{multi,l}}{Z_{multi,u}} \cdot e^{-(E_{zl,multi,u} - h\nu)/(kT)} \qquad (5.8)$$

with the frequency $\nu = c/\lambda$.

The emission cross-sections calculated by this method can have a deviation of up to 20% from the real value due to vibronic interactions [aul82]. The calculation of the emission cross-sections from the absorption cross sections has the disadvantage that the long wavelength part of the transition, which is usually well observable in emission measurements, is very weak or not at all observed in the absorption measurements. Also the signal-to-noise ratio decays rapidly to longer wavelengths which makes the correct determination of the emission cross-sections in the long wavelength part of the transition difficult. In the short wavelength part of the transition the emission cross-sections calculated by the reciprocity method are, however, more accurate than those determined from the emission measurements since the absorption measurement is not affected by reabsorption which can significantly reduce the measured emission intensities.

The emission cross-sections can be calculated from the fluorescence spectra through the Füchtbauer-Ladenburg-equation [aul82, pay92]:

$$\sigma_{se}(\lambda) = \frac{\lambda^5 I_{i \to j}(\lambda)}{8\pi n^2 \tau_{rad} \int_j \lambda' I_{i \to j}(\lambda') d\lambda'} =: C_{FL} \lambda^5 I_{i \to j}(\lambda). \qquad (5.9)$$

with the intensities $I_{i \to j}$ of the transition between the Stark-levels i and j, the radiative lifetime τ_{rad}, and the refractive index n of the regarded wavelength range.

The quantitative evaluation of this equation is usually avoided due to several reasons: The integral of the fluorescence intensity has a very large error margin, especially in the long wavelength region. In case of ions with more than one excited state this also causes problems in the correct calculation of the branching ratio for the emission from i to j. Furthermore the radiative lifetime can be a source for considerable error margins, especially in systems with strong non-radiative decays or efficient energy transfer.

Generally the emission intensities $I_{i \to j}$ are multiplied with λ^5 and the resulting spectrum is fitted to the spectrum calculated by the reciprocity method. By using the Füchtbauer-Ladenburg-equation the emission cross-sections for non-ground state transitions can be determined if the transition in question can be measured in one measurement together with a ground state transition from the same manifold to ensure an identical system response function. With a known emission cross-section from the ground-state transition $\sigma_{se,1}(\lambda_1)$ all other emission cross sections for transitions originating in the same excited state can be calculated:

$$\sigma_{se,j}(\lambda) = \sigma_{se,1}(\lambda_1) \cdot \frac{I(\lambda)}{I_1(\lambda_1)} \cdot \frac{\lambda^5}{\lambda_1^5} \qquad (5.10)$$
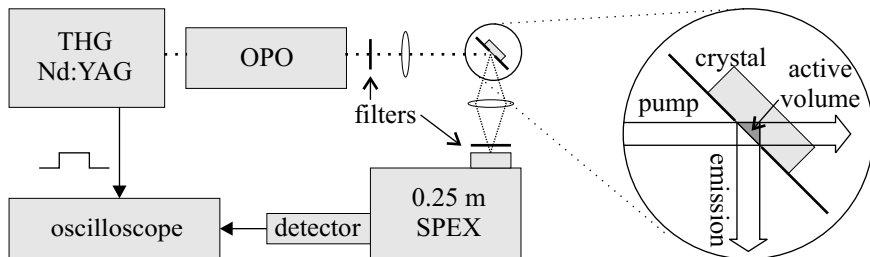
Figure 5.2: Setup for lifetime measurements

5.4   Time Resolved Emission Measurements

In order to measure the fluorescence decay, the sample is excited by a short pulse of a few nanoseconds duration and the temporal development of the fluorescence intensity is then monitored by a fast detector.

In the case of ytterbium, non-radiative multi-phonon decays can be neglected due to the large energy gap between the two manifolds. At low dopant concentrations the measured fluorescence decay is mainly single exponential and the decay time is nearly identical to the radiative lifetime. At higher dopant concentrations a strong quenching of the $^2F_{5/2}$-lifetime can be observed. This is due to efficient energy transfer processes to impurities in the crystals. Depending on the transfer process the decay curve can become non-exponential [bol01].

The samples were excited using an optical-parametric-oscillator (OPO), that is pumped by a frequency tripled, Q-switched Nd:YAG laser (see figure 5.2). The fluorescence signal is separated from the OPO pulse by filters and an additional monochromator. The signal is then detected by an S1-photomultiplier and recorded by an oscilloscope. In order to achieve a better signal-to-noise ratio, the signal is averaged for several thousand pulses. The setup of the sample is crucial for the correct measurement of the fluorescence lifetime. Due to the large overlap between the absorption and emission in ytterbium, radiation trapping can be very efficient and can prolong the measured decay time by up to 50% [bol01]. Radiation trapping can be nearly completely avoided by placing the crystal behind an aperture and exciting through this aperture. The detector has to be placed at an angle of nearly 90°, while avoiding direct reflection of the excitation pulse into the detector. By this method the volume that is excited and detected is kept very small, and energy that is reabsorbed outside this volume will not be detected, thus reducing the impact of radiation trapping on the measurement.
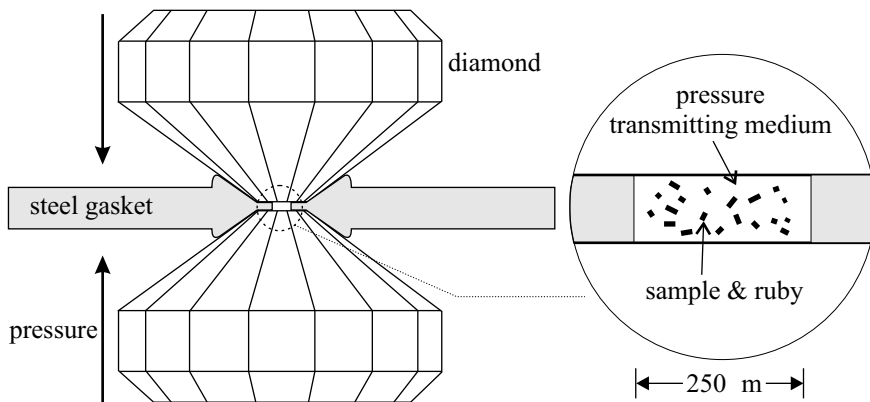
Figure 5.3: Diamond anvil setup for high pressure measurements

5.5   High Pressure Measurements

The high-pressure measurements presented in the next chapter were performed using a diamond anvil cell with the described excitation and emission setups [tro01]. The anvil cell consists of two diamonds with polished end facets of about 0.5 mm diameter. The diamonds are mounted opposing each other in a steel cell that is needed to stabilize the orientation of the diamonds and transfer the pressure onto the diamonds. A steel plate of 200 - 400 μm thickness is placed between the end facets of the diamonds and forms the gasket for the sample chamber. The samples are placed in a small hole of approximately 250 μm diameter and 20 - 50 μm height that is drilled into the steel gasket. After the sample in powder form is placed in the sample chamber, the chamber is filled with a pressure transmitting medium and is then sealed by placing it between the diamonds. The pressure transmitting medium needs to keep its liquid phase throughout the entire pressure and temperature range required for the experiment to ensure that the pressure is transferred hydrostatically onto the sample. Non-hydrostatical pressure can lead to drastic and uncontrollable changes of the local sample geometry and therefore unpredictable results.

In the experiments ethanol and liquid argon were used as pressure transmitters. Unlike ethanol, liquid argon does not solidify at 10 K which is favorable for the low temperature measurements shown here. However, liquid argon is very complicated to handle in experiment. Comparisons between spectra taken with ethanol and liquid argon as pressure transmitters revealed no visible differences in the recorded spectra, even at low temperature. Therefore, all later measurements used ethanol.

The used anvil cell supports pressures of up to 35 GPa (350 kbar). The pressure is adjusted by tightening several screws that press the diamonds closer together. Ruby powder was used as a pressure sensor. The shift of the red ruby fluorescence depending on temperature and pressure is very well documented [mcc63, rek99, tro01] and can be calculated above ambient pressure by the following formula:

$$P = 0.132(E_{Ruby,0GPa}(T) + 18 - E_{Ruby,press.}) \qquad (5.11)$$

The pressure is calculated in GPa using the energies of the ruby emission in cm^{-1} at atmospheric and high pressure. The resulting shift is approximately 10 cm^{-1} per 1.32 GPa. The position of the ruby line at 10 K is approximately 14409 cm^{-1}.

6

Spectroscopic Investigations

In this chapter the spectroscopic investigations of the ytterbium-doped sesquioxides will be presented. Earlier measurements from the Ph.D. thesis of E. Mix [mix99] are reproduced as far as they are necessary for the understanding of the later measurements and for the evaluation of the laser properties of Yb-doped sesquioxides. The first part of this chapter will treat the spectroscopic properties at room temperature. The remaining chapter discusses the low temperature spectroscopy, such as transitions of ions in the two different crystallographic sites, high pressure experiments, dimer-systems, and impurities. In the last section the current identification of the electronic levels of trivalent ytterbium will be presented.

6.1 Room Temperature Spectroscopy

Measurements at room temperature are necessary for the evaluation of a laser crystal, since they can depict the actual spectral properties near the temperature range of laser operation. Table 6.1 shows a summary of the spectroscopic properties that are important for the evaluation of a laser system with the sesquioxides in comparison to YAG. Unless severe heating of the laser channel of several hundred Kelvin occurs, absorption and emission cross-sections will only show minimal changes. In the case of three-level and quasi four-level systems, like the ytterbium laser, the population of the lower laser level, which is strongly temperature dependent according to the Boltzmann formula (equation 4.22), is a vital information for the evaluation of the laser crystal. However, since the temperature of the active channel depends on the pump power and resonator setup, the values given here have also been calculated for room temperature.

	Yb:Sc$_2$O$_3$	Yb:Y$_2$O$_3$	Yb:Lu$_2$O$_3$	Yb:YAG
absorption maximum [nm]	975.1	976.7	976.0	968.8
$\Delta\lambda_{absmax}$ [nm]	≈ 1.5	≈ 2.1	≈ 2.2	≈ 2.5
σ_{abs} [10^{-21}cm^2]	44 @ 975.1	24 @ 976.7	30 @ 976.0	8.3 @ 968.8
	8.7 @ 942	8.7 @ 950	9.5 @ 949	8.2 @ 941.5
λ_{laser} [nm]	1041	1031	1032	1030
	1095	1076	1079	1050
σ_{se} [10^{-21}cm^2]	14.4 @ 1041	10.6 @ 1031	12.8 @ 1032	19 @ 1030
	3.3 @ 1095	4.2 @ 1076	4.3 @ 1079	3 @ 1050
lower laser level [cm^{-1}]	481	414	427	565
	579 (1041)	498 (1031)	514 (1032)	612 (1030)
	1017 (1095)	874 (1076)	903 (1079)	785 (1050)
thermal population @ 300K [%]	8.1	10.6	10.1	5.8
	5.0 (1041)	7.0 (1031)	6.6 (1032)	4.6 (1030)
	0.6 (1095)	1.1 (1076)	1.0 (1079)	2.0 (1050)
σ_{reabs} [10^{-21}cm^2]	0.7 @ 1041	0.8 @ 1031	0.7 @ 1032	1.2 @ 1030
	<0.1 @1095	<0.1 @1076	<0.1 @1079	<0.2 @1050
τ_{flu} Yb(3%) [µs]	800	850	820	1050

Table 6.1: Spectroscopic properties of Yb-doped sesquioxides in comparison to YAG

6.1.1 Absorption and Emission Measurements

The room temperature absorption spectra of the four sesquioxides Yb:Sc$_2$O$_3$, Yb:Y$_2$O$_3$, Yb$_2$O$_3$, and Yb:Lu$_2$O$_3$ are shown in figure 6.1. For comparison, the spectrum of Yb:YAG is also shown. The dopant concentrations of the used crystals were about 3% for the doped sesquioxides and 7% for YAG (all values given relative to the replaced ion). Due to the low distribution coefficient of ytterbium in scandia, the calculated absorption cross-sections may have an error of 5 - 10% due to slightly different dopant concentrations in the samples used for the absorption and the microprobe measurements.

The spectra of the sesquioxides show three main absorption features, a small one around 900 nm, a broader transition around 940 nm, and the strong, sharp zero-

line around 975 nm. The transition strength of the two broad bands is in the same region as those of Yb:YAG at 915 nm and 940 nm between 5 and 10×10^{-21} cm^2. The absorption cross section of the zero-lines is much stronger in the sesquioxides than in YAG.

The impact of the crystal-field on the ytterbium spectra can be best seen when scandia and yttria are compared. Scandia has the smallest lattice sites of the four hosts, which results in the strongest crystal field. This can be seen in the splitting of the main absorption features. In scandia the zero-line and the shortest wavelength absorption maximum are separated by more than 90 nm, in yttria with much larger lattice sites this difference is only 80 nm. The splitting of the levels in lutetia and ytterbia is slightly larger than in yttria. It is notable that the spectra of lutetia and ytterbia are nearly identical which confirms the observation made on thermal conductivity in chapter 2.3, that the ytterbium-dopant only causes small distortion in the lutetia lattice. The zero-line at 975 nm is strongest and sharpest in ytterbia, followed by scandia and lutetia. The peak absorption cross-section of ytterbia is unknown due to the strong absorption of the material. The absorption length $(1/\alpha)$ of the zero-line is estimated to be less than 5 μm, which makes the preparation of sufficiently thin crystals (less than three absorption lengths) very complicated.

Optical pumping is possible in all three absorption regions. The absorption around 940 nm is currently the most interesting for pumping with laser diodes, since the absorption is sufficiently broad and powerful InGaAs-diodes in this wavelength region are commercially available. The zero-line at 975 nm is more interesting for pump sources with a narrow spectral range like Ti:sapphire lasers or narrowly emitting diodes due to the linewidth of only 1.5 to 2 nm. Simulations of the sesquioxides in the thin-disk-laser setup (see chapter 7) have shown that pumping of the zero-line can enhance the efficiency of the sesquioxide lasers, even if diodes with a broad spectral range are used. However, the efficiency rises considerably when narrow excitation sources are used since the absorbed part of the pump light becomes larger. A drawback of zero-line pumping is that the wavelength of the pump has to be kept very stable since small deviations cause a considerably lower absorption of the pump light.

There are three main emission features (see figure 6.2). The zero-line emission is, as in absorption, the strongest in the sesquioxides. In ytterbia the emission appears weaker because the fluorescence is nearly completely reabsorbed by the zero-line absorption. The splitting of the emission features is strongest in scandia and weakest in yttria, analogous to the absorption measurements. Also the spectra of ytterbia and lutetia are nearly identical, except for the mentioned zero-line.

The emission cross-section of the line between 1030 and 1040 nm is in the range of 10^{-20} cm^2, which is 50 to 75% of the cross-section of the corresponding line in YAG. The emission cross-sections of the longest wavelength line are 3 $\times$
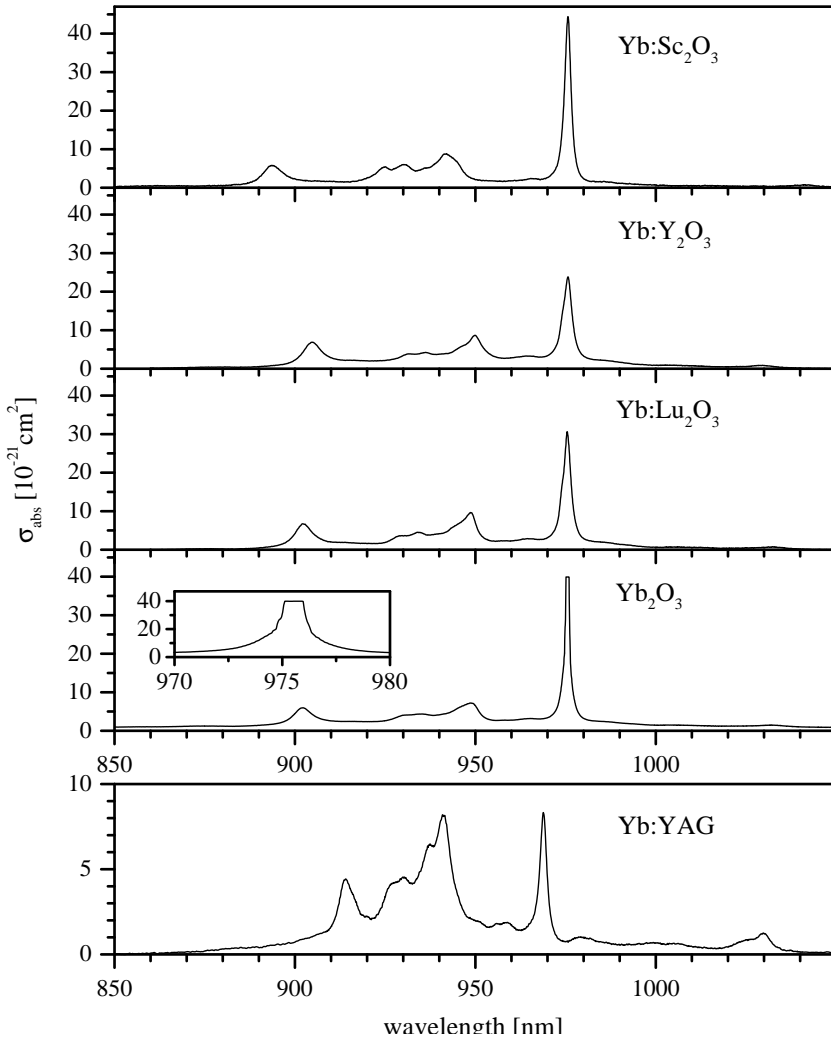
Figure 6.1: Room temperature absorption spectra of Yb^{3+} in Sc_2O_3, Y_2O_3, Lu_2O_3, Yb_2O_3, and YAG [mix99]. The scale of the YAG measurement is enlarged by 4.7 compared to the other spectra. The zero-line of Yb_2O_3 could not be fully resolved with the used crystal of 94 μm thickness.
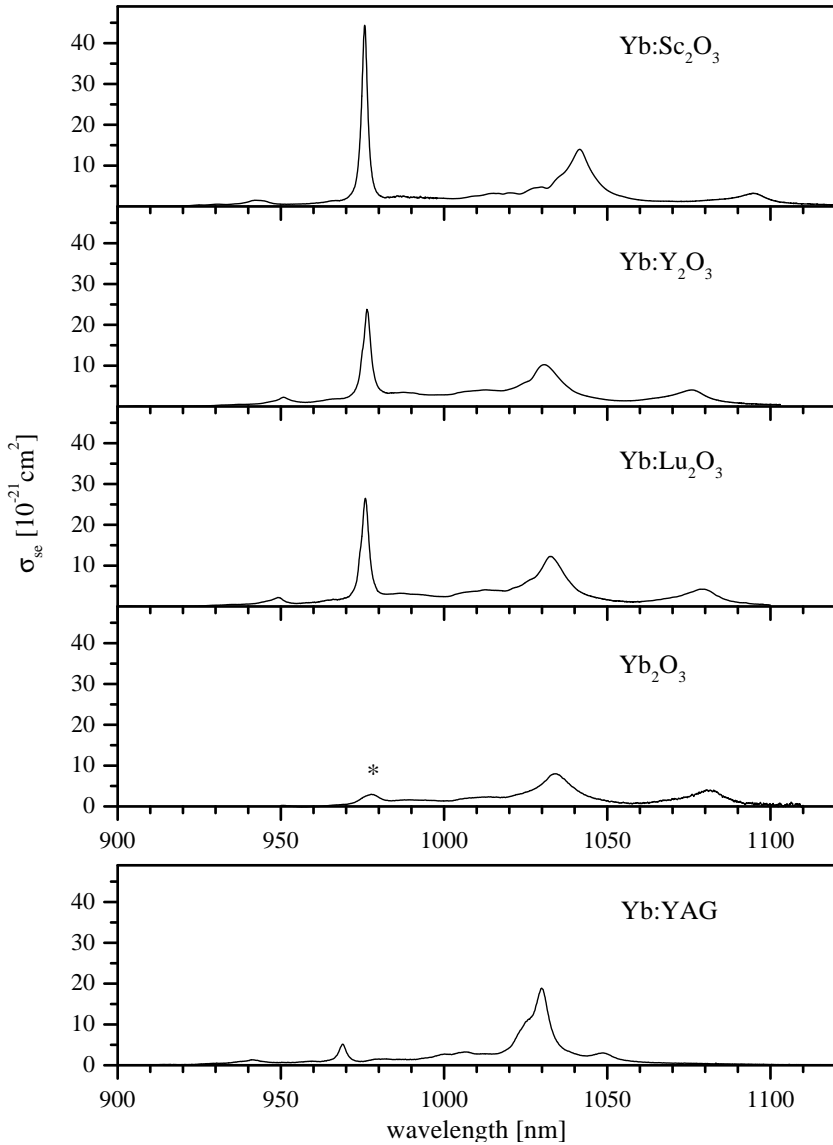
Figure 6.2: Room temperature emission spectra of Yb^{3+} in Sc_2O_3, Y_2O_3, Lu_2O_3, Yb_2O_3, and YAG [mix99]. * reduced intensity due to strong reabsorption.

10^{-21} cm^2 which is in the same range as the corresponding line in YAG.

The emission cross-sections shown in figure 6.2 have been determined by fitting the emission measurement to the emission cross-sections calculated from the absorption spectra as described in chapter 5.3.

Efficient gain for laser operation can be found at the emission lines around 1030 - 1040 nm and 1075 - 1095 nm. Laser operation of both lines in scandia, yttria, and lutetia has been demonstrated [mix99]. The wavelength of the ytterbium laser depends on the used transmission of the output coupler, as long as no wavelength selective elements are placed inside the resonator. For transmissions below $\approx$ 1% the laser operates on the long wavelength

Figure 6.3: Room temperature emission and absorption (dashed) in the range of the main emission lines [mix99].

peak, at higher transmissions it switches to the 1030 -1040 nm emission. This behaviour can be explained by the reabsorption of the laser emission in the crystal. Figure 6.3 shows the absorption and emission cross sections in the range of the laser wavelengths. In the 1030 -1040 nm region there is still noticeable absorption whereas the 1075 - 1095 nm region is basically free of reabsorption. This reabsorption leads to a lower overall gain at low output coupler transmissions in the 1030 -1040 nm region which causes the laser to run at 1075 - 1095 nm. At higher output coupler transmissions the gain for 1030 -1040 nm region is higher due to the higher emission cross section [mix95, mix99].
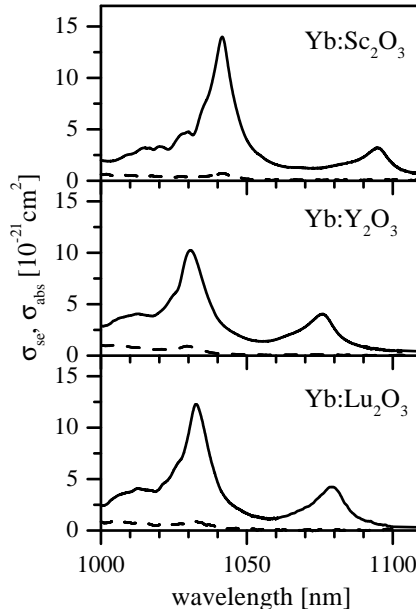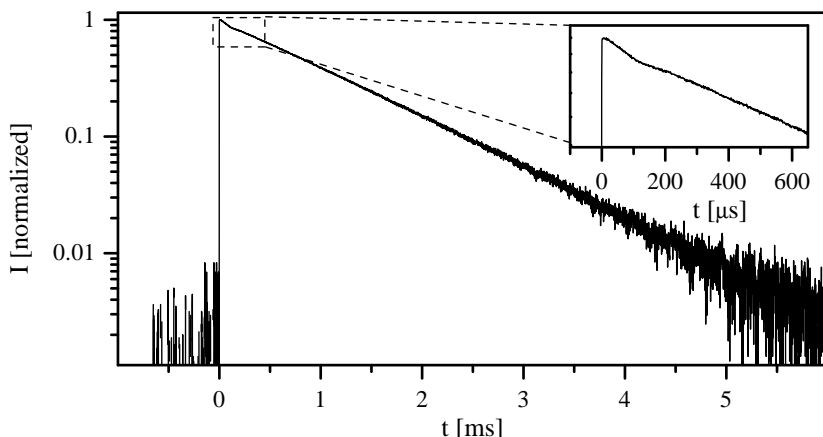
Figure 6.4: Fluorescence decay of Yb(10%):Sc$_2$O$_3$ [bol01].

6.1.2 Lifetime Measurements

Many ytterbium-doped materials exhibit a fluorescence lifetime in the range of about 1 ms at low to medium dopant concentrations. The sesquioxides have fluorescence lifetimes of around 800 µs at ytterbium concentrations of a few percent (see table 6.2). In this case the fluorescence has a single exponential decay as shown in figure 6.4. The origin of the nonlinearity in the first 200 µs of the decay can be explained by a fast energy migration from excited ytterbium ions to their direct neighbors [bol01]. The impact of this fast transfer on the ytterbium system depends on the amount of impurities and defects in the crystal and can cause a notable decrease of the quantum efficiency [bol01, mue01].

At higher ytterbium concentrations a shortening of the fluorescence lifetime is observed in many materials. Similar effects can be created by co-doping the crystals with small amounts of impurity ions. The observed fluorescence decay curves show exponential and non-exponential parts that can be explained by different dominating energy transfer mechanisms [bol01]. Figures 6.5 and 6.6 show fluorescence decays of Yb:Sc$_2$O$_3$ co-doped with holmium in single and double logarithmic representation. In figure 6.5 a non-single-exponential decay can be seen in the beginning which ends in a single exponential decay after some time. The single-exponential part can be explained by slow energy migration between the ytterbium ions in the crystal. The other part decays with $e^{-\sqrt{t}}$ and is attributed to ytterbium-holmium transfer. In the $\ln(\ln(I/I_0))$ vs. $ln(t)$ representation the
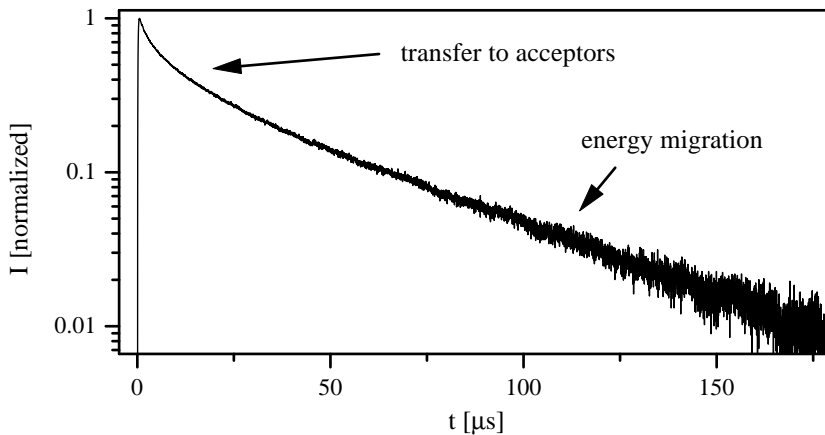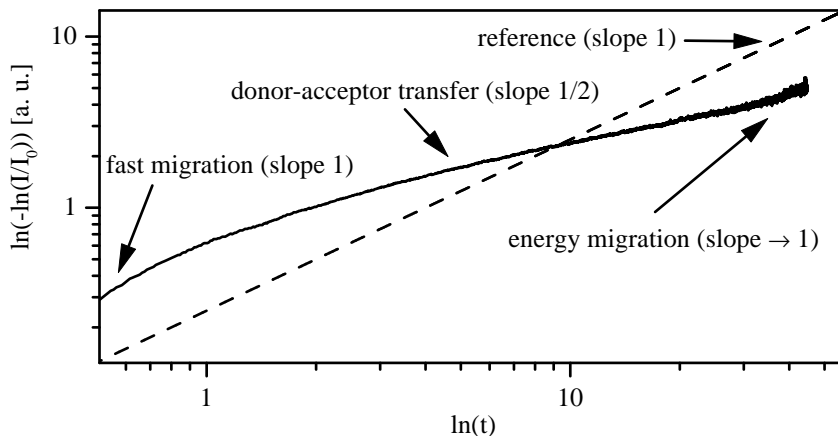
Figure 6.5: Fluorescence decay of Ho(0.1%),Yb(10%):Sc$_2$O$_3$ [bol01].

Figure 6.6: Fluorescence decay of Ho(0.5%),Yb(10%):Sc$_2$O$_3$ [bol01].

host	n_{Yb} $[10^{20}\text{cm}^3]$	τ [µs]	host	n_{Yb} $[10^{20}\text{cm}^3]$	τ [µs]
Y_2O_3[1]	0.7 (0.26%)	790	Lu_2O_3[1]	1.31 (0.46%)	820
Y_2O_3[1]	23.9 (8.9%)	580	Lu_2O_3	28.1 (10%)	530
Sc_2O_3[1]	1.0 (0.3%)	730	Lu_2O_3	56.3 (20%)	10
Sc_2O_3[2]	33.6 (10%)	776	Lu_2O_3	84.3 (30%)	2.6
Yb_2O_3	281 (100%)	15	Lu_2O_3	228 (80%)	0.013
Yb_2O_3[3]	281 (100%)	66.5	Lu_2O_3	257 (90%)	0.014

Table 6.2: Room temperature fluorescence lifetimes of Yb-doped sesquioxides.

fast migration in the very beginning of the decay can also be seen.

Since no internal mechanisms of the ytterbium ion can lead to a quenching of the fluorescence lifetime, the shortening of the lifetime at higher concentrations depends entirely on the amount, type, and distance of the impurities and defects in the crystal to ytterbium ions.

An impurity that is often found in oxide crystals is divalent ytterbium. It is formed when an ytterbium ion is next to an oxygen vacancy or impurity that provides charge compensation and can be identified by a strong absorption in the visible spectral range (see figure 6.7). Divalent ytterbium appears to be an excellent transfer partner for trivalent ytterbium and relaxes non-radiatively in the sesquioxides and YAG. It has been identified as one of the main quenching impurities in YAG but can fortunately be completely removed by annealing unless a quadrivalent impurity provides stable charge compensation [mue01].

Impurities that are present in the starting materials can usually not be avoided unless cleaner starting materials are available. In the case of a lattice with a low ion density like YAG the impurities from the starting materials of 5N purity have no effect on the fluorescence lifetime even if the yttrium ions are completely replaced by ytterbium ($Yb_3Al_5O_{12}$). The measured lifetime in this case is still 1 ms with a small fast decay in the beginning due to the fast migration to neighboring ions [mue01]. In the sesquioxides the interionic distances are considerably shorter than in YAG because of the high cation density. This has the effect that the transfers to impurities become much more probable and have an impact on the fluorescence lifetime. This is illustrated by the lifetime of Yb:Lu_2O_3 at different doping levels (see table 6.2). The lifetime at low concentrations of 820 µs is quenched to 13 ns

---

[1]measured by E. Mix [mix99]

[2]measured by A. Bolz [bol01]

[3]grown without crucible in LHPG setup
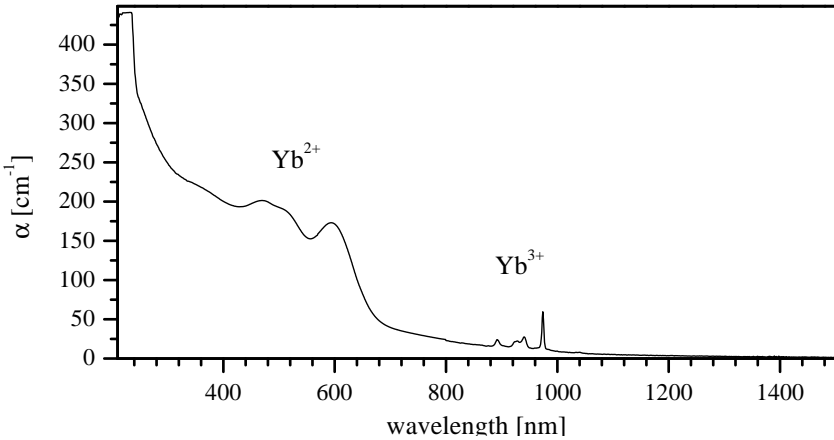
Figure 6.7: Absorption spectrum of Yb^{2+} and Yb^{3+} in Sc_2O_3. The slow rise from 1300 nm towards shorter wavelengths is due to color-centers caused by oxygen vacancies as described in section 3.5.2.

at 80% doping level. Since the pure ytterbia has a lifetime of 15 μs in comparable growth conditions, this indicates that the used lutetia contains either more, or more harmful impurities than the used ytterbia. Studies with $Yb:Sc_2O_3$ co-doped with small amounts of rare-earths showed that praseodymium, samarium, dysprosium, holmium, and thulium strongly affect the fluorescence of the ytterbium ion, whereas neodymium, europium, terbium, and erbium only show a weak impact on the ytterbium fluorescence. Chromium and possibly other, up to now untested, transition metals also cause strong quenching of the ytterbium fluorescence [bol01].

Other impurities that originate in the growth setup can also have severe effects on the ytterbium lifetime. In the case of $Yb_3Al_5O_{12}$ the use of iridium crucibles limited the ytterbium lifetime in YbAG to less than 300 μs. When rhenium crucibles were used instead, the intrinsic lifetime of 1 ms could nearly be reached [mue01]. In the case of ytterbia the growth setup introduces an additional lifetime-shortening. The lifetime of ytterbia grown without contact to any other materials is 67 μs, whereas the crystal grown from a rhenium crucible only has a lifetime of 15 μs. It is yet unknown if the rhenium itself causes the lifetime-shortening or if any impurities from the material or the manufacturing process of the crucible are the cause.
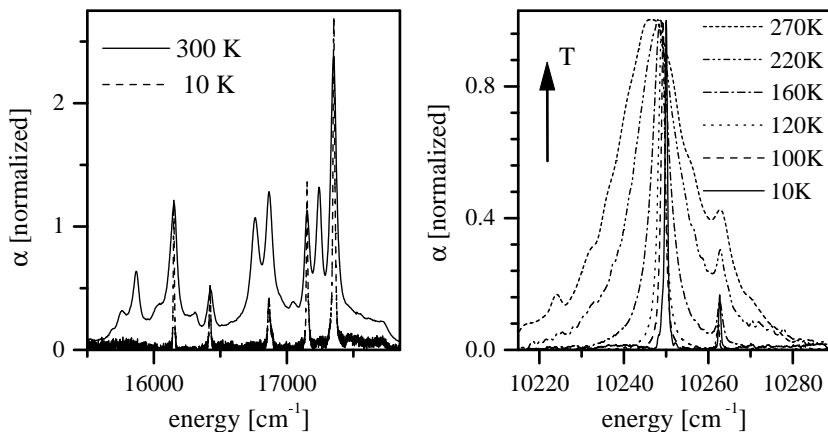
Figure 6.8: left: Absorption of the $^1D_2$-manifold of Pr:Y_2O_3 at 10 K
and 300 K [pet98]. right: Temperature dependent absorp-
tion of the zero-line of Yb:Lu_2O_3 [mix99].

The purity of the available starting materials appears to be a major issue for the
ytterbium-doped sesquioxides. The strong fluorescence quenching currently sets
an upper limit for the use of highly doped sesquioxides as laser materials. Future
research will have to show which impurities need to be avoided or reduced in order
to use ytterbium-doped sesquioxides as laser materials with optimum efficiency.

6.2   Low Temperature Spectroscopy

The spectroscopic features of a material change strongly between room temper-
ature and low temperatures. At low temperatures the linewidths as well as the
population of phononic states are greatly reduced compared to room temperature.
This leads to sharper transitions and less prominent vibronic sidebands as can be
seen in figure 6.8 for the zero-lines of Yb:Lu_2O_3. Furthermore, the thermal popu-
lation of higher Stark-levels of a manifold is reduced according to the Boltzmann
law (equation 4.22). Under ideal circumstances only the lowest Stark-level of each
manifold is populated so that only transitions from these levels can occur as seen
in figure 6.8 left for praseodymium-doped yttria.

   In the case of many rare-earths with weak electron-phonon coupling low tem-
perature absorption and emission measurements are sufficient to clearly identify
the electronic levels of the system, see e. g. figure 6.8 left. In the case of trivalent

Figure 6.9: Expected ytterbium transitions at 10 K

ytterbium this is not the case, mostly due to the strong electron-phonon-coupling of the ytterbium ion.

The energy level scheme of trivalent ytterbium suggests that, if only the lowest Stark level of each manifold is populated,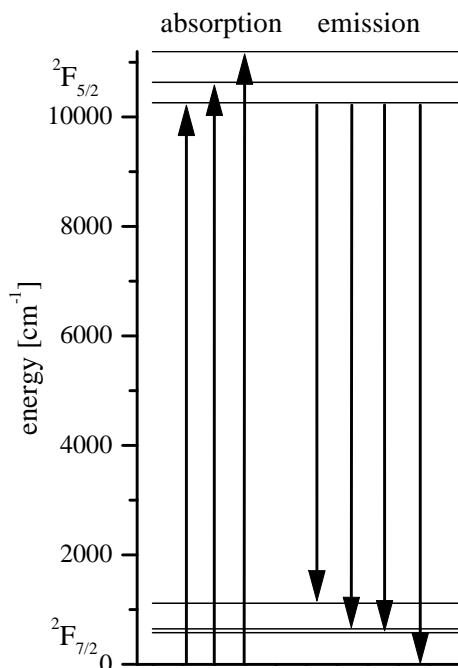 which is fulfilled at temperatures of a few Kelvin, there will be three absorption lines from the $^2F_{7/2}$ ground-state to the $^2F_{5/2}$ excited state and four emission lines from the $^2F_{5/2}$ (see figure 6.9). Due to the fact that there are two lattice sites in the sesquioxides, two sets of lines can be expected: a strong set from ions in C_2-sites (in the following referred to as C_2-lines or C_2-transitions) and a weaker set from ions in C_{3i}-sites (in the following referred to as C_{3i}-lines or C_{3i}-transitions). The C_{3i}-lines can be expected to be about one order of magnitude weaker than the C_2-lines due to the inversion symmetry of the site. Vibronic transitions are expected to be another source for many additional lines in the spectra. In areas where the vibronic and electronic lines overlap coupling between these two can occur, which may result in transition shapes that do not show any peaks at the positions of the original electronic and vibronic transitions. Furthermore infrared transitions of Yb-pairs like $\left[\frac{7}{2}(0), \frac{7}{2}(0')\right] \rightarrow \left[\frac{5}{2}(y), \frac{7}{2}(y')\right]$ can appear. However, these transitions are very weak and are therefore likely to be covered by the electronic and vibronic transitions. Also transitions from impurity ions in the crystals may occur. In the absorption and emission spectra of the C_2-ions (figures 6.11 and 6.12) these transitions are not likely to be observed due to the strong transitions of the ytterbium ions and the comparatively low concentrations of the possible impurities. In the C_{3i} excitation and emission spectra these impurity transitions may be observed due to the weaker transitions of the C_{3i}-ions.
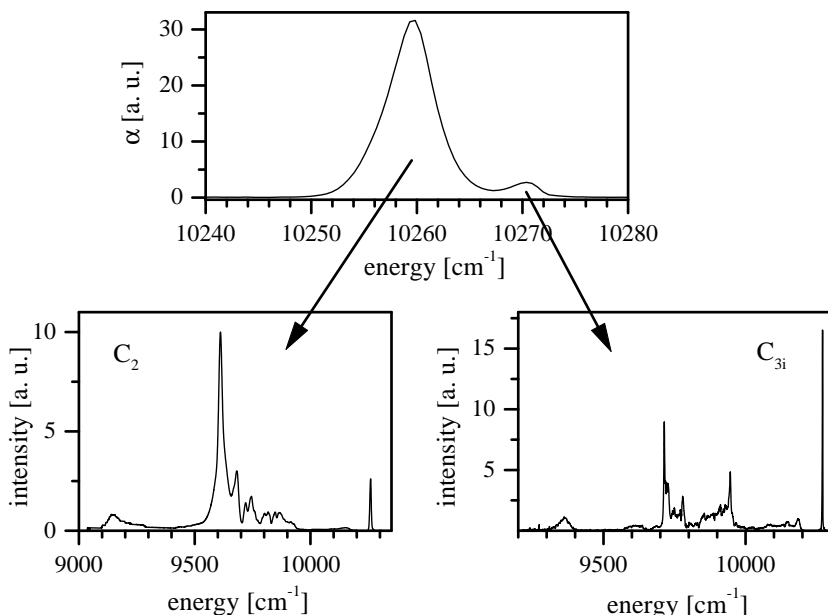
Figure 6.10: 10 K fluorescence of Yb:Sc_2O_3 depending on the excitation energy.

6.2.1   Site-Selective Absorption and Emission Measurements

In low temperature absorption measurements the spectral features originate nearly completely in ions on C_2-sites as can bee seen in figure 6.10 and 6.11. The only line that is clearly caused by C_{3i} transitions is the small peak next to the C_2 zero-line, which is identified as the C_{3i} zero-line. In emission, the resulting spectrum depends on the excitation wavelength, temperature, and doping level. If the C_2-zero-line is excited the strong emission spectrum of the C_2-ions can be measured (see figure 6.10 and 6.12). By excitation in the C_{3i}-zero-line a completely different emission spectrum appears (as seen in figures 6.10 and 6.14), which contains mostly fluorescence of ions in C_{3i}-sites and some parts of the C_2-spectra. The absorption of the C_{3i}-ions cannot be directly measured due to the much stronger absorption of the C_2-ions in the same spectral region. It can only be accessed through the excitation of fluorescence in a spectral region where the C_{3i} fluorescence dominates over the C_2-fluorescence, which is best fulfilled in the region between 9900 and 10000 cm^{-1}. A measurement of the C_{3i}-sites in ytterbia is not
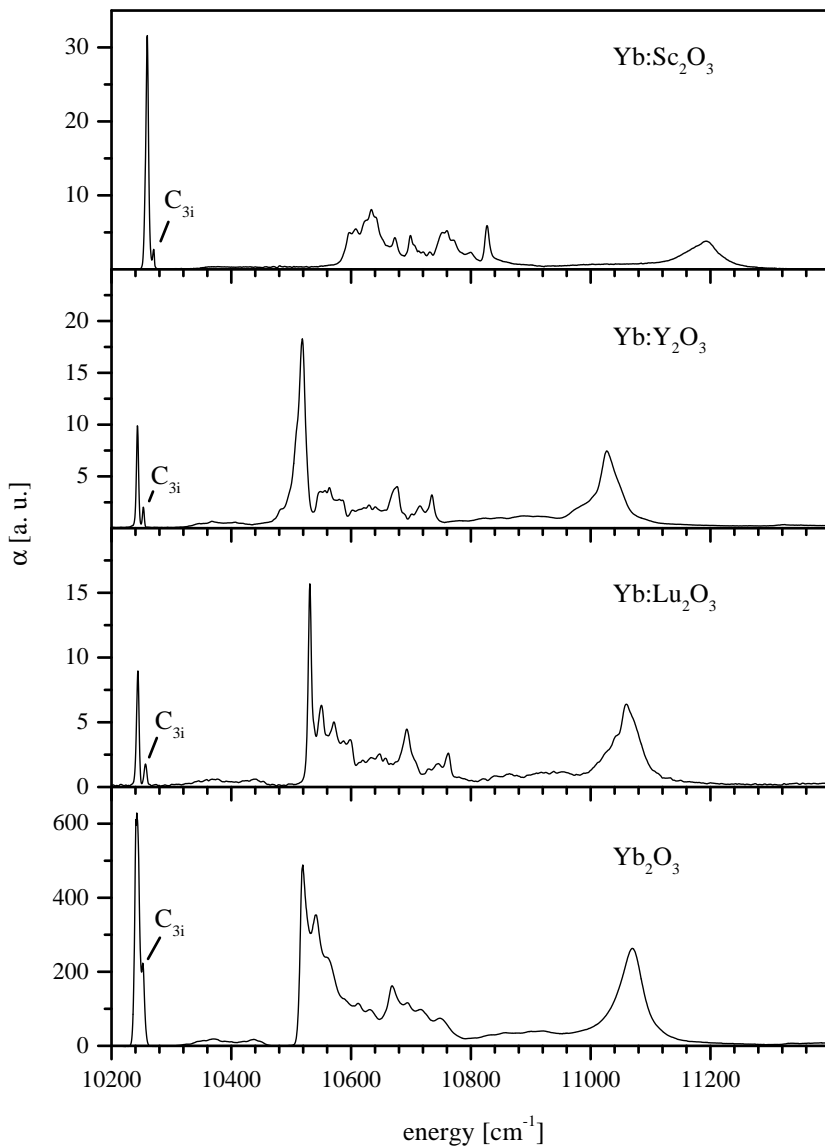
Figure 6.11: 10 K absorption of Yb in scandia, yttria, lutetia, and yt-
terbia in C_2-sites [mix99].
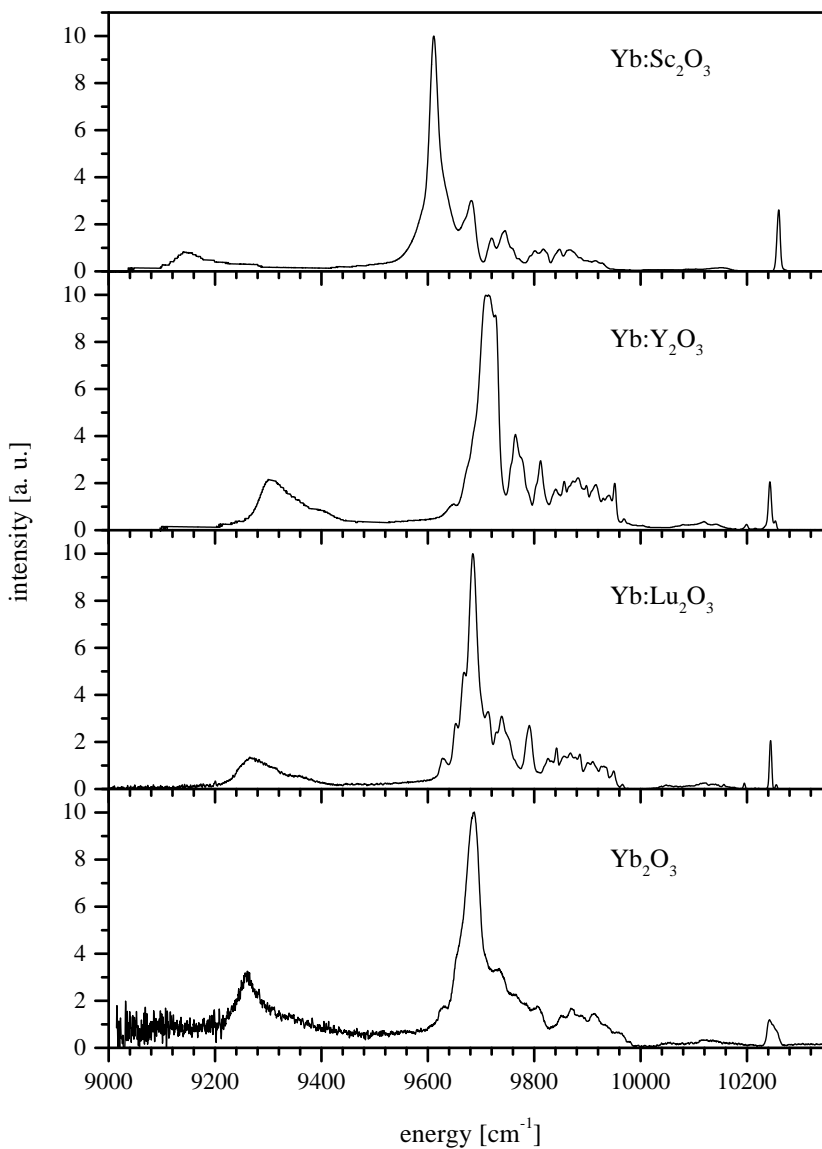
Figure 6.12: 10 K emission of Yb in scandia, yttria, lutetia, and ytterbia in C_2-sites [mix99].

Figure 6.13: 10 K excitation of Yb in scandia, yttria, and lutetia in C_{3i}-sites [mix99].

Figure 6.14: 10 K emission of Yb in scandia, yttria, and lutetia in C_{3i}-sites [mix99].

possible due to a very efficient energy transfer from the C_{3i}-sites to the C_2-sites at ytterbium concentrations above 6% or temperatures above 120 K [mix99].

The ytterbium absorption of ions in C_2-sites (figure 6.11) shows three main features in all sesquioxides. The zero-line is located between 10242 cm^{-1} in ytterbia and 1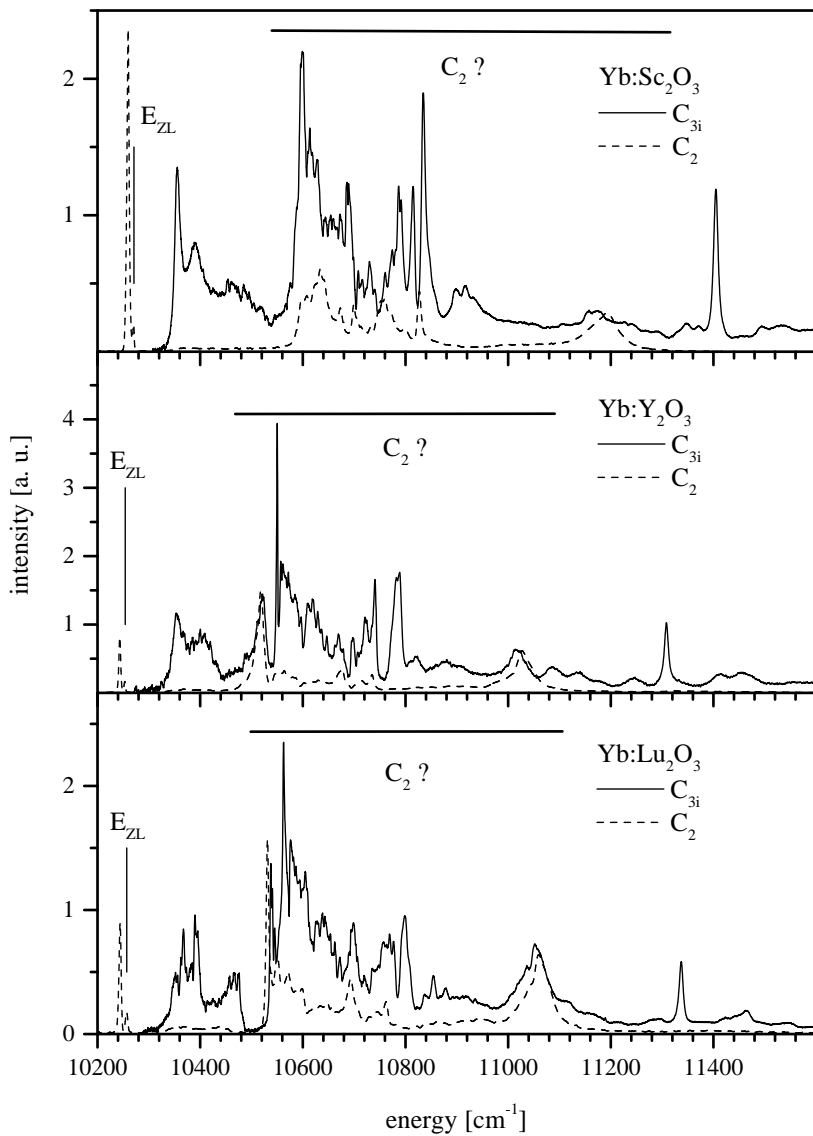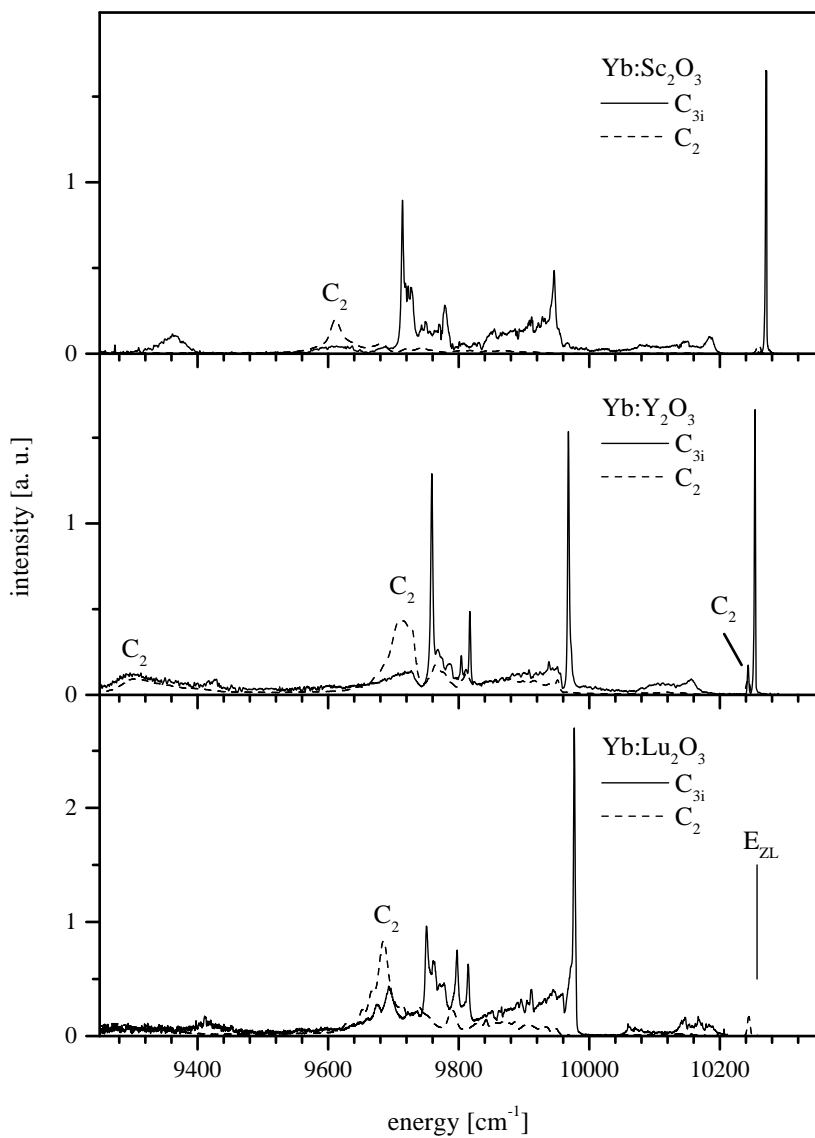0260 cm^{-1} in Yb:Sc$_2$O$_3$. It is notable that the zero-line in ytterbia is considerably broader than in the other materials. An explanation for this can be found in the study of pair effects (see section 6.2.3). The second broadest zero-line can be found in scandia. This can be understood by the influence of local distortions of the scandia lattice by the considerably larger ytterbium ions, which will be studied in more detail later in this section. In drastic contrast to the observations at room temperature the absorption strength of the zero-lines in comparison to the strengths of the other features in the spectra varies strongly in the different crystals at low temperatures. In Yb:Y$_2$O$_3$ and Yb:Lu$_2$O$_3$ the zero-line is only half as strong as the highest other peak, whereas at room temperature the zero-line peak is by far the strongest in all four materials. This may be an indication that the other electronic levels of the $^2F_{5/2}$-manifold experience strong coupling with vibronic levels which affects the observable transition strengths. The second main feature is the sharply structured absorption between 10500 and 10850 cm^{-1}. It is a mixture between one or two electronic levels and several vibronic lines. Between 11000 and 11250 cm^{-1} is the third main feature, a broad nearly unstructured absorption which does not have the typical narrow linewidths of $4f$-$4f$ transitions. This absorption can either be explained by an electronic level coupled to several vibronic levels or it could be completely of vibronic origin. The splitting between the main features is comparable to that found in the room temperature spectra. Scandia shows the largest and yttria the smallest splitting. The splitting of the ytterbia and lutetia spectra is again nearly identical, but the shapes of the absorption features show slight differences.

The emission of the C_2-sites (figure 6.12) is very similar to the absorption. Here also three main features can be found and the splitting of the features is again according to the splitting at room temperature. The splitting of the emission features is slightly larger than the splitting of the absorption features. The emission strengths of the zero-lines between 10242 and 10260 cm^{-1} are, as in the room temperature spectra, reduced by reabsorption, which can be best seen in the case of ytterbia.

The excitation spectra of ions in C_{3i}-sites (figure 6.13) look considerably more complicated than those of the C_2-ions. The spectra consist of many narrow to very narrow lines and there are four main features. The zero-line, which was not measured due to strong interference from the C_2-zero-line, is marked in the spectra. The second feature is an absorption of medium strength between 10300 and 10500 cm^{-1} which appears only very weakly in the C_2-spectra. In the C_2-

spectra this band can be assigned to purely vibronic transitions (see section 6.3), but the strength of the transitions in the C_{3i}-spectra suggest that it is a mixture of one electronic and several vibronic levels. The third main feature between 10500 and 11200 cm^{-1} shows many similarities with the C_2 absorption spectrum. It could either be of electronic-vibronic origin with some additional lines brought in by energy transfer from C_2-sites to C_{3i}-sites, or it could be completely caused by energy transfer from C_2-ions and vibronic transitions. Especially the appearance of the highest energy C_2-peak around 11050 to 11200 cm^{-1} in the C_{3i} spectra indicates that energy transfer from the C_2- to the C_{3i}-sites is as well possible as transfer from C_{3i} to C_2. The most notable feature in the C_{3i}-excitation spectra is the sharp line at 11300 to 11400 cm^{-1}. The shape of this line suggests a mainly electronic origin or mixing between an electronic line and a single vibronic state. It has to be noted that the splitting of the features in the C_{3i} excitation spectra is slightly larger than the splitting in the C_2 absorption spectra.

The C_{3i} emission spectra (figure 6.14) also show strong traces of the C_2-spectra especially between 9600 and 9800 cm^{-1}. Apart from the probably electronic-vibronic band between 10000 and 10200 cm^{-1}, the measurements show an emission between 9600 and 10000 cm^{-1} which is likely to contain at least one electronic C_{3i}-level coupled to several vibronic levels and overlayed by C_2-emissions. The longest wavelength feature that appears in the C_{3i}-spectra is a weak broad peak between 9350 and 9400 cm^{-1}. A strong, sharp peak as in the C_{3i}-excitation measurements could not be found. According to crystal-field theory an emission with a larger splitting from the zero-line than that measured in excitation can be expected: The splitting of the features in the C_{3i}-measurements should be comparable to those in the C_2-measurements. In the case of lutetia the ratio between the maximum splitting of the main features of the C_2-sites $\text{Split}_{abs}/\text{Split}_{se}$ is 0.8, in the case of the C_{3i}-sites it is 1.3. This drastically different behaviour of the splitting of the ground-state and excited-state can not be brought into agreement with crystal-field theory and calculations, which will be presented in section 6.3. Since the splitting ratio should be at least similar for C_2- and C_{3i}-sites this suggests the existence of another emission band at a longer wavelength. When the splitting ratio $\text{Split}_{abs}/\text{Split}_{se}$ from the crystal-field calculations (0.80 for C_2; 0.85 for C_{3i}) is used, this would indicate that the missing band is located around 9000 to 8900 cm^{-1}. Unfortunately this wavelength range cannot be measured with the S1-photomultiplier which was used for all infrared measurements. Other detectors that are available in this wavelength range like Ge, PbS, or InSb have either a much lower efficiency or lower signal to noise ratio than a photomultiplier. Therefore a measurement of the expected extremely weak C_{3i}-emission in this wavelength range is not feasible at the current time.

Another interesting point in the low temperature spectra is the influence of
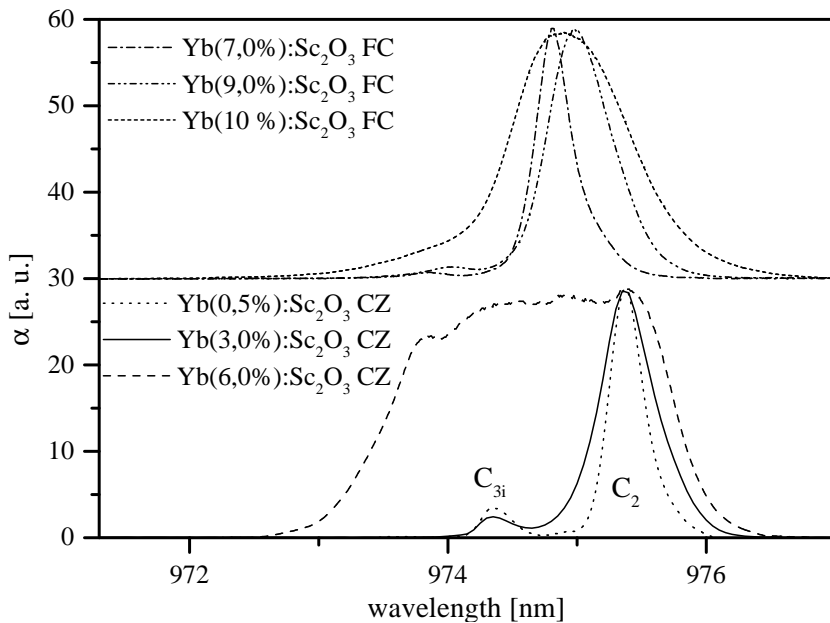
Figure 6.15: 10 K absorption of the zero-line in Yb:Sc$_2$O$_3$. CZ: Czochralski-method; FC: fast cooling, complete crystallization within a few seconds to ensure a distribution coefficient near unity.

local distortions of the host lattice around a dopant ion that can be observed in scandia which shows the largest mismatch between the ionic radii of the host and dopant ions. In yttria and lutetia no effects due to local distortions could be observed. Figure 6.15 shows the absorption of the zero-line of ytterbium-doped scandia at different doping levels and grown by different methods. All spectra were taken using a mercury lamp to establish an absolute wavelength scale independent of the monochromator adjustment. Several grown crystals show very different results in terms of peak wavelength and linewidth. However, no correlation between the observed features and the dopant-concentrations or growth conditions could be found. The sharpest line has been measured for the lowest ytterbium concentration of 0.5%. Here only a very small peak between the C$_2$ and C$_{3i}$ peaks can be seen. The line of the Yb(9%):Sc$_2$O$_3$ crystal is nearly as sharp, but shifted by almost 0.5 nm compared to the 0.5%-doped crystal. All other crystals show much wider
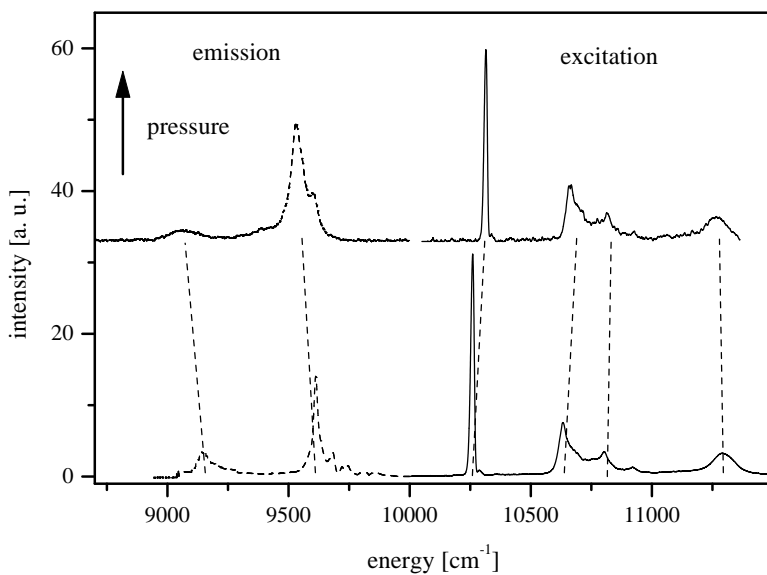
Figure 6.16: Yb:Sc$_2$O$_3$ 10 K excitation and emission under pressure.
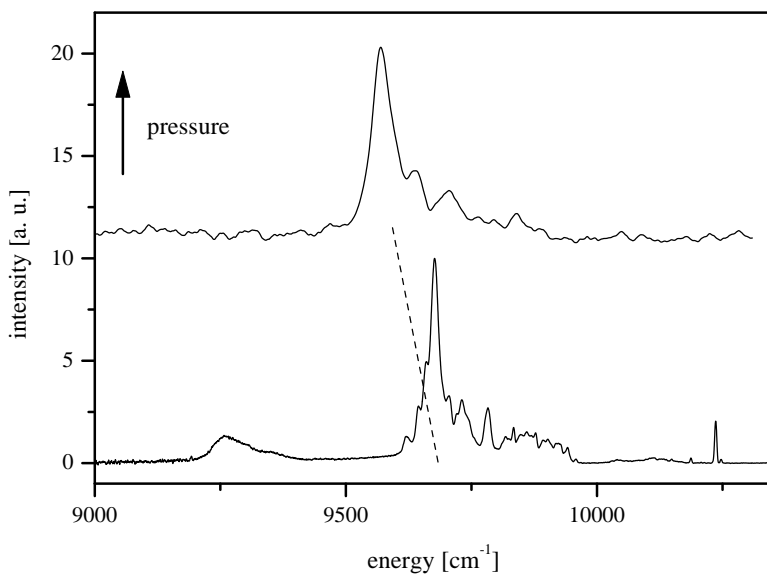
Figure 6.17: Yb:Lu$_2$O$_3$ 10 K emission under pressure.

$\bar{J}$ [cm^{-1}]	$^2F_{7/2}$	$^2F_{5/2}$
Molecular-field with T_N	0.073	0.131
Molecular-field with $\theta = 1.1$ to $1.5 \times T_N$	0.080 - 0.110	0.145 - 0.197
Series-expansion-method	0.103	0.188

Table 6.3: Calculations of $\bar{J}$ in Yb$_2$O$_3$ with T_N=2.3 K.

lines, especially the Czochralski-grown 6%-doped crystal which apparently has several distinguished local surroundings for the ytterbium ions. The line positions and shapes have up to now only been reproducible for low dopant concentrations of 1% or less. In this case the absorption has the shape of the shown 0.5%-doped crystal. The observed shifts and line broadening can be explained by ytterbium ions that are close to other ytterbium ions. The local distortion of the host lattice around one dopant ion affects the ligands of another ytterbium ion nearby and therefore causes the observed changes. It is also possible that nearby ytterbium ions are shifted partially from the lattice sites towards interstitial lattice positions (compare section 2.1) by the local distortions around one ion.

6.2.2 Measurements at High Hydrostatic Pressures

The measurements performed with sesquioxides under high pressures are shown in figures 6.16 and 6.17. In the case of Yb:Sc$_2$O$_3$ a small blue-shift of the zero-line of 55 cm^{-1} was observed. This is in contrast to the expected red-shift due to the nephelauxetic effect and indicates that pressure induced changes of the local ligand configuration occurred. The overall influence of the crystal field is increased under pressure as can be seen by the increased splitting of the levels in the case of the emissions of scandia (by 141 cm^{-1}) and lutetia (not determinable). The excitation spectrum of scandia on the other hand shows a decreased splitting by 78 cm^{-1} which in conjunction with the blue-shift of the entire spectrum indicates changes of the local geometry. In the case of lutetia the absence of the lowest energy emission might be an indication that the phase transition which is supposed to occur at 4 GPa has taken place. Also an increase of the linewidths of all transitions was observed, which has the result that no changes in the pressure spectra can be seen, that would indicate different shifts of electronic and vibronic levels and therefore allow the identification of the electronic levels.

The total pressure at the time of the measurement is unknown due to experimental difficulties. Depending on the ratio of the sample powder and the ruby powder that is used for the pressure calibration in the sample chamber, either the ytterbium signal or the ruby signal could be measured at high pressure due to
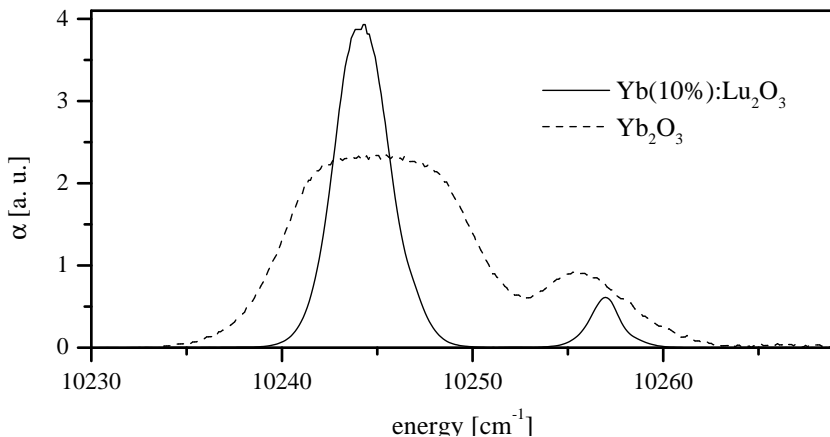
Figure 6.18: 10 K Absorption of Yb(10%):Lu$_2$O$_3$ and Yb$_2$O$_3$.

the increasing linewidths and decreasing signal intensities. Near ambient pressure both signals could be clearly detected. Measurements in which the ruby signal could be detected indicate that the applied pressure on the samples was well above 10, possibly above 20 GPa.

6.2.3   Dimer Systems

Davydov-Splitting

In order to estimate the impact of the exchange-coupling of the ytterbium ions on the infrared spectra, calculations of the average exchange integral have been made with the methods described in section 4.2 and the Neel Temperature of ytterbia of $T_N = 2.3$ K as published in [moo68]. The results are shown in table 6.3. For both manifolds the maximum Davydov-splitting $2\bar{J}$ of the electronic levels can be expected to be smaller than 0.5 cm^{-1} which is well below the linewidth of the observed transitions and is therefore negligible. It can only be observed as a line broadening at higher concentrations, as seen in the case of 10%-doped lutetia and ytterbia (see figure 6.18). It has to be noted that the absorption peak of ytterbia could not be fully resolved even though a sample of only 12 µm thickness was used in this absorption measurement.
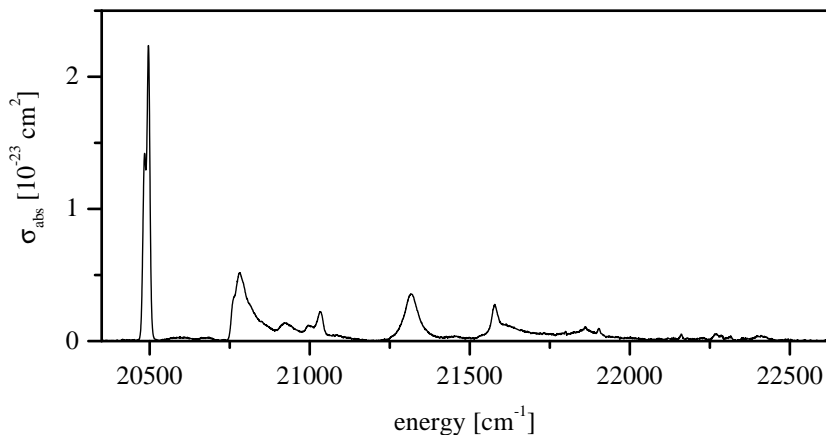
Figure 6.19: 10 K pair absorption of Yb_2O_3.

Pair-Transitions

Visible absorption and emission of ytterbium pairs can be expected between 20000 and 23000 cm^{-1} in absorption and 18000 and 21000 cm^{-1} in emission. Unfortunately, due to the fact that ytterbium is an excellent energy transfer partner and upconversion sensitizer for many rare-earths with transitions in the same spectral region, a large amount of parasitic transitions from impurities in the chemicals has to be anticipated in emission measurements. Of the available substances only $Yb:Sc_2O_3$ crystals made from 5N purity material were usable for pair emission measurements when the crystal was grown in a crucible. Grown without a crucible 5N ytterbia was also well suited for the observation of pair emission. In case of the available 4N purity materials none of the crystals were suitable to observe the weak pair emissions. Pair absorption could only be observed in a 4 mm long ytterbia crystal grown by the Bridgman-method. In all other hosts with ytterbium concentrations of up to 15% and a thickness of up to 15 mm the absorbance of the ytterbium pairs was below the detection limit at low temperatures.

In the sesquioxides three types of pairs exist: C_2-C_2, C_2-C_{3i}, and C_{3i}-C_{3i}. Since the pairs all have no special symmetry, as shown in section 2.1, transitions of these pairs are all equally strong according to selection rules. Especially the high symmetry of the single C_{3i}-ions has no impact on the transition probabilities of the pairs. However, there are other factors which influence the pair transition probabilities. The most important factor is the separation of the coupled ions. In
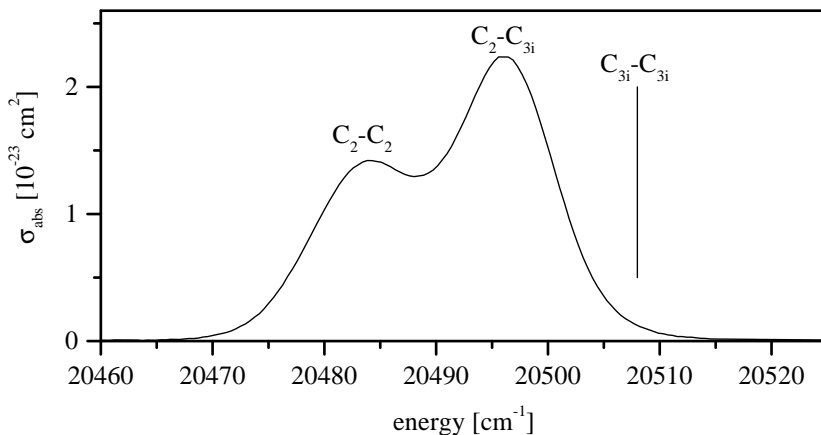
Figure 6.20: 10 K pair absorption of Yb_2O_3 at the combination wave-
lengths of the zero-lines.

case of C_2-C_2- and C_2-C_{3i}-pairs the distances are almost equal at $0.33 \times a_0$, so that the exchange- and super-exchange coupling of the two pairs is also almost equal, giving them the same transition probabilities (compare estimations below). The ions in C_{3i}-C_{3i}-pairs are much farther separated ($0.5 \times a_0$). The exchange coupling between the ions and therefore the transition probabilities of C_{3i}-C_{3i}-pairs are therefore reduced by a factor of 10^6 in comparison to the other pair types. Due to this large difference C_{3i}-C_{3i}-pairs can not be expected to appear in pair spectra. The second factor which influences the transition probabilities of the pair types is the coordination number of the pair type. C_2-C_2-pairs are four-fold coordinated, this means each C_2-ion has four nearest C_2-neighbors, and C_2-C_{3i}-pairs are six-fold coordinated, which makes transitions of C_2-C_{3i}-pairs 1.5 times as probable as transitions of C_2-C_2-pairs.

The transition energies of pair transitions are the added energies of the single-ion transitions. Pair spectra will therefore show all combinations of the possible transitions of two single-ions. At low temperatures, when only the lowest Stark-level of a manifold is populated, transitions from the lowest level of the ground state to all combinations of the excited levels $\left[\frac{7}{2}(0), \frac{7}{2}(0') \right] \rightarrow \left[\frac{5}{2}(y), \frac{5}{2}(y') \right]$ can be expected in the green spectral region. In absorption there are nine possible $\left[\frac{7}{2}(0), \frac{7}{2}(0') \right] \rightarrow \left[\frac{5}{2}(y), \frac{5}{2}(y') \right]$ transitions for the C_2-C_{3i}-pairs. In the case of C_2-C_2-pairs only six of the nine possible combinations have distinct energies, which leads to a total of 15 expected absorption lines in the green spectral region plus
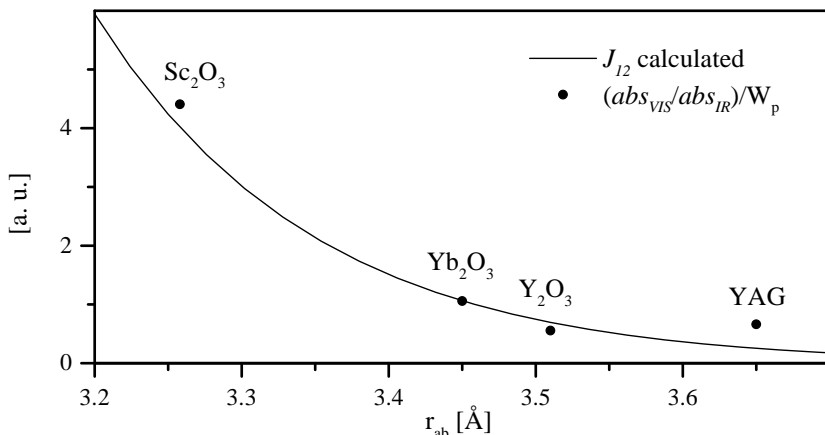
Figure 6.21: Exchange interaction of neighboring ytterbium ions and
relative visible to infrared absorption intensity in the
sesquioxides and YAG.

transitions from vibronic states, which are expected to be weaker than in the single
ion spectra. Coupling between electronic and vibronic states is expected to be
weakened, though not completely removed since only the intensity of the vibronic
transitions is weakened but not the strength of the coupling between the electronic
and vibronic levels. In emission only transitions of the type $\left[\frac{5}{2}(0), \frac{5}{2}(0')\right] \rightarrow$
$\left[\frac{7}{2}(y), \frac{7}{2}(y')\right]$ are possible, which leads to 10 lines at distinct energies for the C_2-
C_2-pairs and 16 for the C_2-C_{3i}-pairs, totaling 26 transitions and the mentioned
vibronic and electronic-vibronic lines.

The absorption spectrum of Yb-pairs in ytterbia is shown in figure 6.19. The
measured absorption of the crystal is strong enough that transitions from rare-
earth impurities in the 5N starting material can be ruled out as source of any of
the measured lines. The spectral resolution of this measurement was 0.4 Å, which
is much better than the observed lines would have required. By using this high
resolution the existence of sharper structures can be ruled out, so that the shown
measurement accurately describes the ytterbium pair absorption. Compared to
the single-ion spectra, there are by far less sharp transitions, which would have
indicated strong vibronic transitions. It is also notable that some structures, such as
the band between 20750 and 21100 cm^{-1} look similar to the calculated electronic-
vibronic transitions in figures 4.3 and 4.4. The splitting of the recorded lines is in
the range of 2000 cm^{-1}. This indicates a large Stark-splitting of the electronic

crystal	minimum Yb-Yb distance [Å]	Yb con- centration $[10^{20}\mathrm{cm}^{-3}]$	abs_{VIS}/abs_{IR}	W_p
Yb(5.5%):Sc$_2$O$_3$	3.27	18.5	3×10^{-5}	0.036
Yb$_2$O$_3$	3.45	281.3	2×10^{-4}	1.0
Yb(8.9%):Y$_2$O$_3$	3.53	23.9	1×10^{-5}	0.095
Yb(10%):Y$_3$Al$_5$O$_{12}$	3.65	13.8	5×10^{-6}	0.04

Table 6.4: Measured visible and infrared absorption ratios in the sesquioxides and YAG.

levels.

The contributing pair types can be easily identified in the pair-zero-line at 20500 cm^{-1}, which is shown enlarged in figure 6.20. The energy of a C$_2$-C$_2$ $\left[\frac{7}{2}(0), \frac{7}{2}(0')\right] \rightarrow \left[\frac{5}{2}(0), \frac{5}{2}(0')\right]$ transition is 20484 cm^{-1}, for a C$_2$-C$_{3i}$-pair 20496 cm^{-1}, and for a C$_{3i}$-C$_{3i}$-pair 20508 cm^{-1}. It is clearly visible that the C$_2$-C$_2$ and the C$_2$-C$_{3i}$ appear in the spectrum and the C$_{3i}$-C$_{3i}$ transition does not. Also, as expected, the C$_2$-C$_{3i}$ transition is about 50% stronger than the C$_2$-C$_2$-transition.

The intensity of the pair transitions is directly related to the strength of the combined exchange- and super-exchange-coupling. The exchange coupling for trivalent ytterbium ions, as shown in figure 6.21, has been calculated under the rough assumptions that super-exchange-coupling can be neglected and that the ytterbium ion which has a closed $4f$-shell with one hole can be treated like a hydrogen atom with one electron. The calculation with respect to the ion-separation was performed using equation 4.12 and the ytterbium $4f$-wave-function calculated by the Hartree-Fock-method (see section 4.5). The relative intensities of the pair-absorption to the infrared-absorption at room temperature for the sesquioxides and YAG were measured by Mikhail Noginov at Norfolk State University (see table 6.4). When the measured absorption ratios are scaled by the probability of ytterbium ions having nearest neighbors W_p at the given concentration, the ratios show good agreement with the calculated exchange-coupling curve considering the the numerous approximations made.

The main impurities that were found to emit in the same spectral region as ytterbium pairs are terbium, holmium, and thulium, as can be seen in the visible emission spectrum of Yb(10%):Lu$_2$O$_3$ (see figure 6.22). In the case of this crystal especially thulium overlaps with the main part of the ytterbium pair emission. Of several tested lutetia materials from different suppliers up to a nominal quality of 6N, no material showed considerably less impurity emissions as in the shown
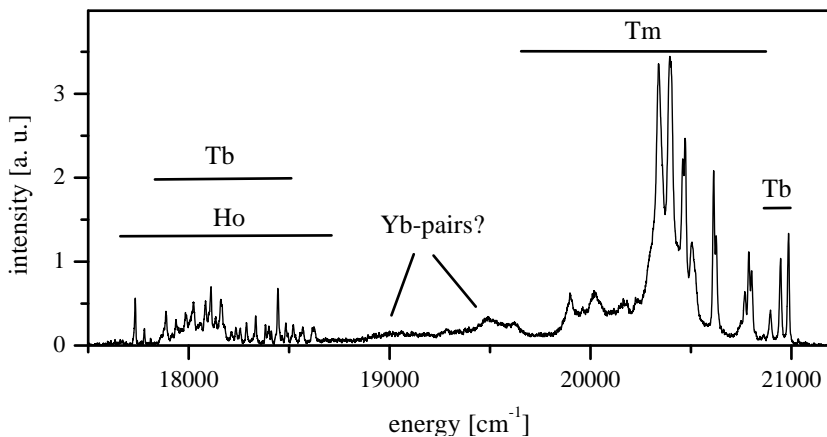
Figure 6.22: Visible emission of Yb(10%):Lu$_2$O$_3$ under ytterbium excitation at 10 K.

spectrum. Only the relative intensity of the different impurities varied.

In the case of Yb(6%):Sc$_2$O$_3$ the visible emission spectrum, as shown in figure 6.24, was corrected for minor impurity emissions from Tb:Sc$_2$O$_3$ and Tm:Sc$_2$O$_3$. The major impurity emission from holmium was not subtracted since the available Ho:Sc$_2$O$_3$ spectra did not fit well enough to the spectrum to retrieve any useful information from this region. Except for the spectral region with holmium emissions below 18500 cm^{-1}, the spectrum completely consists of emissions from ytterbium pairs. Due to the low emission cross-section of the pair transitions the spectral resolution and the signal to noise ratio of this spectrum are too low to make clear identifications of the measured transitions.

The pair emission of Yb$_2$O$_3$ in figure 6.24 shows a similar fingerprint. In this case however the signal to noise ratio was higher by several orders of magnitude than in the measurement of the Yb(6%):Sc$_2$O$_3$ emission due to a better detection system consisting of a photomultiplier tube with optimum efficiency in the green spectral region and a Hammamatsu C5410 photon-counter. The resolution of this spectrum is 0.8 Å which is sufficient to resolve the pair transitions. The transitions caused by holmium in this spectrum can be clearly identified by comparison with an emission spectrum from Ho:Lu$_2$O$_3$. Lines caused by terbium or thulium emissions were not found in this spectrum.
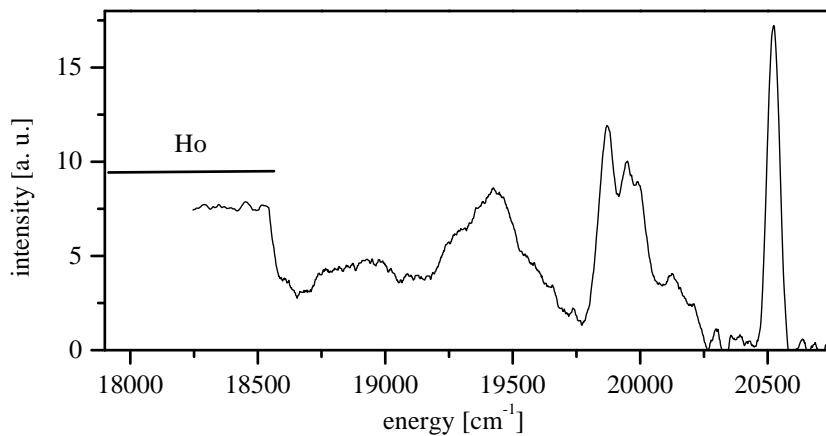
Figure 6.23: 10 K pair emission of Yb(6%):Sc$_2$O$_3$ corrected for thulium and terbium emissions. Resolution: 2 nm
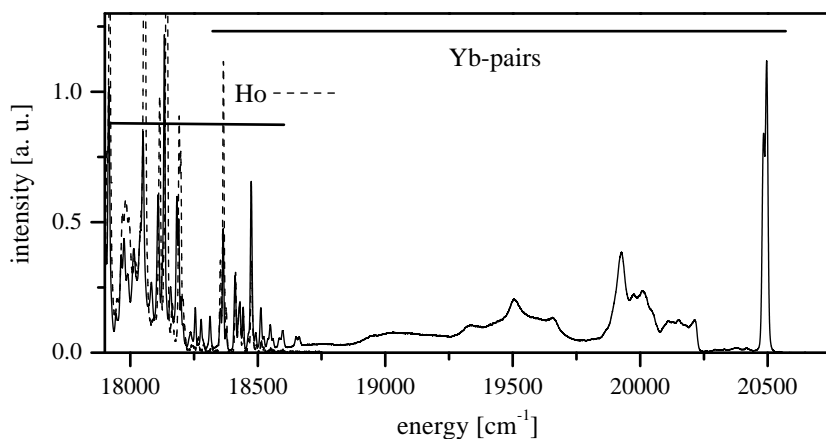
Figure 6.24: 10 K pair emission of Yb$_2$O$_3$. Resolution: 0.8 Å
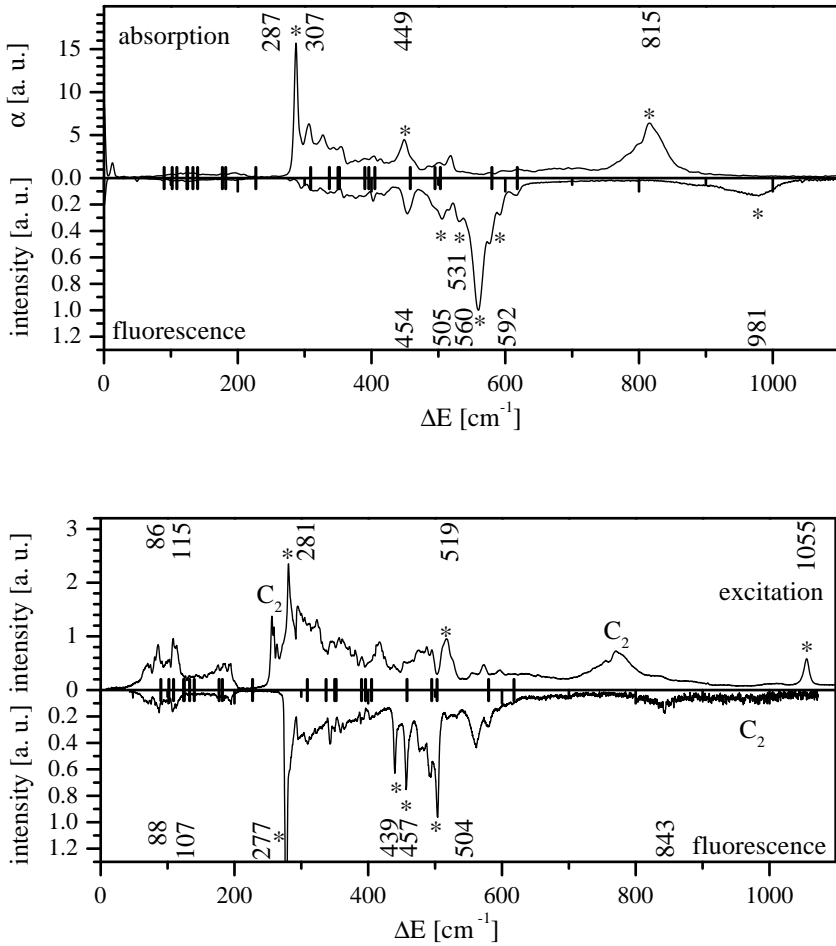
Figure 6.25: 10 K absorption, excitation, and emission spectra of the C$_2$- (top) and C$_{3i}$-sites (bottom) of Yb:Lu$_2$O$_3$ in the Buchanan representation. Raman-active-phonons appear as black marks on the abscissa. Strong peaks are marked by the energy offset from the zero-line. * indicate the Stark-levels defined in [mix99].

6.3 Identification of the Electronic Stark-Levels

From a crystallographic point of view the four sesquioxides are very similar. The only difference is the lattice constant. For the crystal-field this means that the only change is the distance of the ligands to the dopant-ions and that the symmetry of the crystal field remains unchanged in all four crystals. Due to these strong similarities between the materials the identification of the Stark-levels will be presented by analyzing the spectra of ytterbia and lutetia, which together give a complete set of measurements of C_2-, C_{3i}-, and pair spectra. A slight deviation in the overall similarity of the materials is posed by scandia. The ytterbium-dopant is so much larger than the host ions, that distortions of the lattice sites may occur. The recorded single-ion spectra indicate that no major changes of the local symmetry are introduced but it is likely that the crystal-field strength acts somewhat differently in the two lattice sites in scandia in comparison to the other three hosts. This is due to slightly different interatomic distances between the cations and the oxygen ligands in the two sites which allow for different degrees of ligand relaxation around the larger ytterbium ions. Further small differences between the four hosts are introduced by the different phonon-energies but are neglected in this analysis since the available data on phonon-energies are not sufficient to make clear distinctions.

Some insights into the positions of vibronic bands and energetic regions where coupling between electronic and vibronic levels may occur are given by displaying the spectra in the Buchanan representation [buc67]. In this representation the energy scale is set to zero at the position of the zero-line (ZL) in absorption and emission. Then the energy scale of the emission spectrum is mirrored around the zero-line, so that absorption and emission spectra extend to positive energies from the zero-line. In this representation the C_2- and C_{3i}-spectra of Yb:Lu$_2$O$_3$ are shown in figure 6.25. The phonon energies from Raman-measurements coupled to the zero-line are displayed as black marks on the abscissa and one can see that vibronic transitions extend up to $+600$ cm^{-1} from the zero-line. This covers a large portion of the spectral features in all spectra. Furthermore, it has to be taken into account, that additional vibronic transitions may appear due to coupling to the higher electronic levels, so that the occurrence of vibronic lines and the coupling between electronic and vibronic levels is possible in the entire spectrum. An exception may be given in the C_{3i} excitation spectrum by the sharp line located at $+1055$ cm^{-1}. With a maximum phonon energy of 600 cm^{-1} the remaining electronic level would have to be located above $+400$ cm^{-1} to make coupling between a vibronic level coupled this electronic level and the line at $+1055$ cm^{-1} probable. Since this is not likely, as can be seen in the crystal-field calculations below, the line at 1055 cm^{-1} is probably not subject to strong electronic-vibronic coupling.

	$C_2\ ^2F_{7/2}$ [cm^{-1}]	$C_2\ ^2F_{5/2}$ 10244+ [cm^{-1}]	$C_{3i}\ ^2F_{7/2}$ [cm^{-1}]	$C_{3i}\ ^2F_{5/2}$ 10257+ [cm^{-1}]
First calculation for bixbyite [bon00]; x_{calc}	0 490.8 590.1 1035.8	0 420.7 824.8	0 80.2 238.7 823.3	0 79.5 703.7
Yb:Lu$_2$O$_3$: scaled to the maximum splitting in absorption and emission; x_{max}	0 464 559 981	0 515 815	0 122 362 1257	0 119 1055
Yb$_2$O$_3$: x_{max} values refined through pair absorption and emission spectra; x_{refine}	0 432 521 914	0 427 839	0 113 337 1171	0 121 1075

Table 6.5: Crystal-field calculations for Yb:RE$_2$O$_3$.

The same would be true for a corresponding line in the C_{3i}-emission at approximately +1100 cm^{-1} or more, which cannot be proven here since the line could not be measured.

The first step towards the identification of the electronic levels of the sesquioxides is to determine the overall splitting of the levels. The central question here is whether the absorption and emission peaks farthest away from the zero-lines are purely vibronic or include an electronic level. This point can be decided by looking at the pair-absorption of ytterbia. In figure 6.26 the pair-absorption and combinations of the largest peak energies for a small and a large splitting of the energy levels are shown. The two sets of energy levels used to calculate the pair transitions are Stark-level sets published in [mix99]. Both Stark-level sets are based on the strongest peaks of the spectra. The set with the large splitting uses the peaks +815 (C_2) and +1055 cm^{-1} (C_{3i}) apart from the zero-line and the other set does not. The levels of the C_{3i}-peaks have been taken from the Yb:Lu$_2$O$_3$ C_{3i}-spectra under the reasonable assumption that the spectra of the C_{3i}-spectra of ytterbia and lutetia are as similar as the C_2 spectra. It is clearly visible that the combinations for the small splitting do not cover major parts of the pair absorption spectrum above 21500 cm^{-1} which contains transitions that are too strong to be of purely vibronic origin. The combined peak energies for the large splitting on the other hand cover the entire pair-absorption spectrum with fairly good agreement to the

observed peaks. Therefore, it can be concluded with some certainty that the absorption features with the largest splitting from the zero-lines contain an electronic level.

The identification of the electronic levels has been performed in several steps that are explained below in greater detail for the ytterbium excited-state and the ground-state:

1. Crystal-field calculations of the relative positions of the electronic levels (x_{calc})

2. Scaling by fitting the highest Stark-level to the peak farthest away from the zero-line in the infrared spectra (x_{max})

3. Refinement of the scaling by fitting the pair-levels calculated from x_{max} to the pair-spectra (x_{refine})

The relative position of the electronic levels can be determined by crystal-field calculations for the bixbyite structure. However, the calculations can only be used to define the positions if the exact total splitting of a manifold is known, since a calculation of the absolute crystal-field strength is not feasible. The calculations x_{calc} for Yb:Y$_2$O$_3$ that are presented in table 6.5 were done by Carl Bonner at Norfolk State University and complete the partial calculations published earlier in [cha82] for the C$_2$-levels and in [gru85] for the C$_{3i}$-ground-state levels.

The calculated values were then scaled so that the highest Stark-levels fit to the highest energy peaks in the lutetia absorption and emission spectra (see table 6.5):

$$x_{max} = A_{7/2C_2,5/2C_2,7/2C_{3i},5/2C_{3i}} \cdot x_{calc} \tag{6.1}$$

A is the scaling factor for each manifold in the two lattice sites. This procedure was done individually for ions in both lattice sites in the excited state and for ions in the C$_2$-ground state. The scaling for the C$_{3i}$-ground state was performed based on the assumption that the ratio of the maximum splitting between the C$_2$-excited state and the C$_{3i}$ excited state should be equal to the ratio between the ground states of the two sites:

$$\frac{\text{Split}_{5/2C_2}}{\text{Split}_{5/2C_{3i}}} = \frac{\text{Split}_{7/2C_2}}{\text{Split}_{7/2C_{3i}}} \tag{6.2}$$

The obtained splitting of 1257 cm^{-1} for the C$_{3i}$-ground-state has brought up the assumption that there should be a transition in this region.

The choice to place the highest electronic Stark-level at the maximum of the infrared peaks farthest away from the zero-line is somewhat arbitrary. The obtained Stark-levels might be less precise since the peaks used for fitting are probably
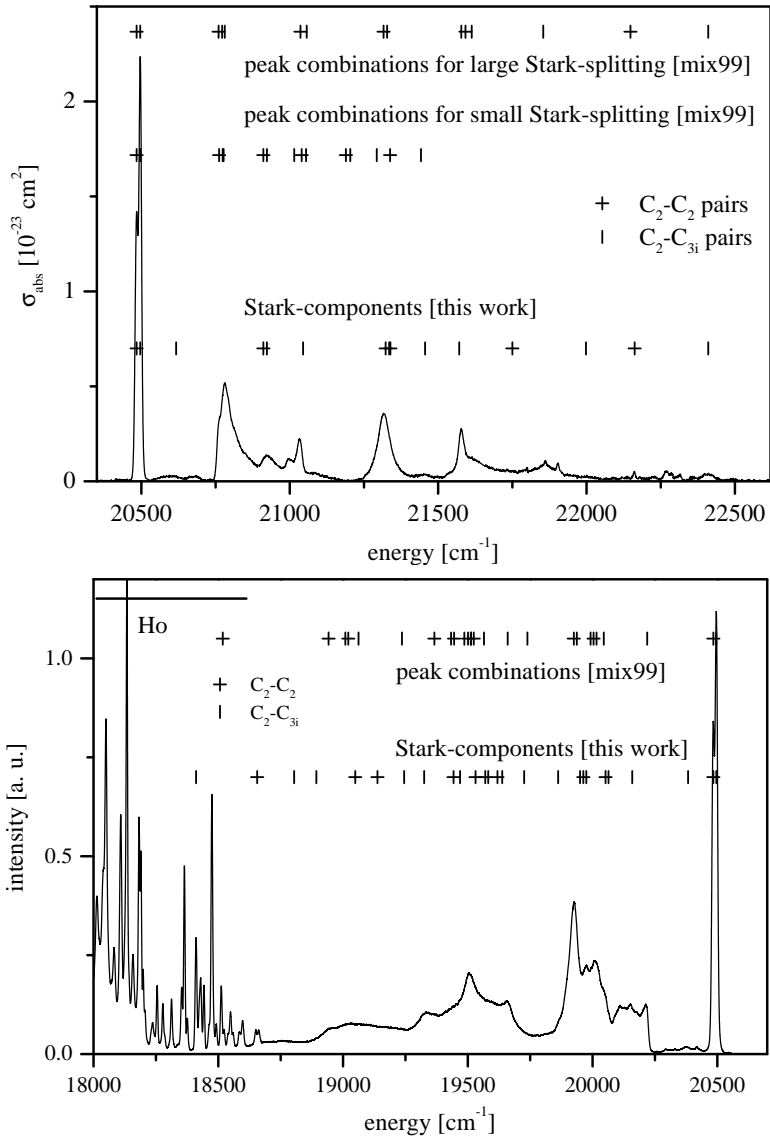
Figure 6.26: Pair absorption (top) and emission (bottom) of Yb_2O_3 with combinations of measured IR-peaks and calculated Stark-levels.

deformed by electronic-vibronic coupling. To obtain correct level positions, the Yb:Lu$_2$O$_3$ x_{max} values were used to calculate combined level positions for fitting the pair absorption and emission spectra. The combined levels were then placed into the pair absorption and emission spectra of ytterbia and rescaled to fit the observed features. The resulting set of levels for ytterbia is shown in table 6.5 as set x_{refine}.

This method works excellently in the case of the pair absorption as seen in the top part of figure 6.26. The calculated pair transitions with the refined set of ytterbia Stark-levels either fit directly to a measured pair transition or are inside of transitions that have shapes similar to those caused by electronic-vibronic coupling (see section 4.3.3 and [lup99]). The identification of the Stark-levels of the excited state of ytterbia by this method is therefore highly reliable. The exact position of the second ^{2}F$_{5/2}$-Stark-level should, however, be further refined with direct calculations of the electronic-vibronic coupling when complete measurements of the phonon-dispersion curves for the materials become available.

In case of the ground-state levels the refinement through pair spectra is, unfortunately not as easy due to the higher number of pair-transitions in emission and the overlap of the pair emissions with holmium emissions. The pair levels shown in figure 6.26 (bottom) were calculated so that the combination of the highest C$_2$-levels corresponds to the small peak at 18656 cm^{-1}, which is the only peak in this region that cannot be accounted for by holmium. The position of this pair peak, in turn, corresponds to a side-peak of the longest wavelength emission band of the C$_2$-ions which is probably the electronic part of a coupled electronic-vibronic transition. However, the confidence in the placement of this level is not as high as in the excited state levels.

The C$_{3i}$-ground state splitting has then been calculated using again the assumption that the ratio of C$_2$ - C$_{3i}$-excited state splitting is identical to the ratio of ground state splitting. The resulting maximum splitting for C$_2$ - C$_{3i}$-pairs coincides with a holmium peak that appears to be slightly broader than the peak in the measured holmium spectrum. Since this difference of the line could also be caused by the fact that the holmium spectrum was taken using a Ho:Lu$_2$O$_3$ crystal and not holmium doped ytterbia it cannot be seen as a definite proof for a pair transition at this wavelength. The different host material could cause the different linewidth even though it is not likely since all other significant lines have nearly identical linewidths in both spectra. The other pair transitions calculated from these levels fit to the measured pair emission spectrum within the boundaries set by the numerous expected transitions and the fairly broad transitions of the spectrum.

The Stark-levels for the other host materials have been determined by transferring the positions in the single-ion spectra of ytterbia and lutetia to the corresponding spectral features of the other materials. The results are shown in table 6.6 and
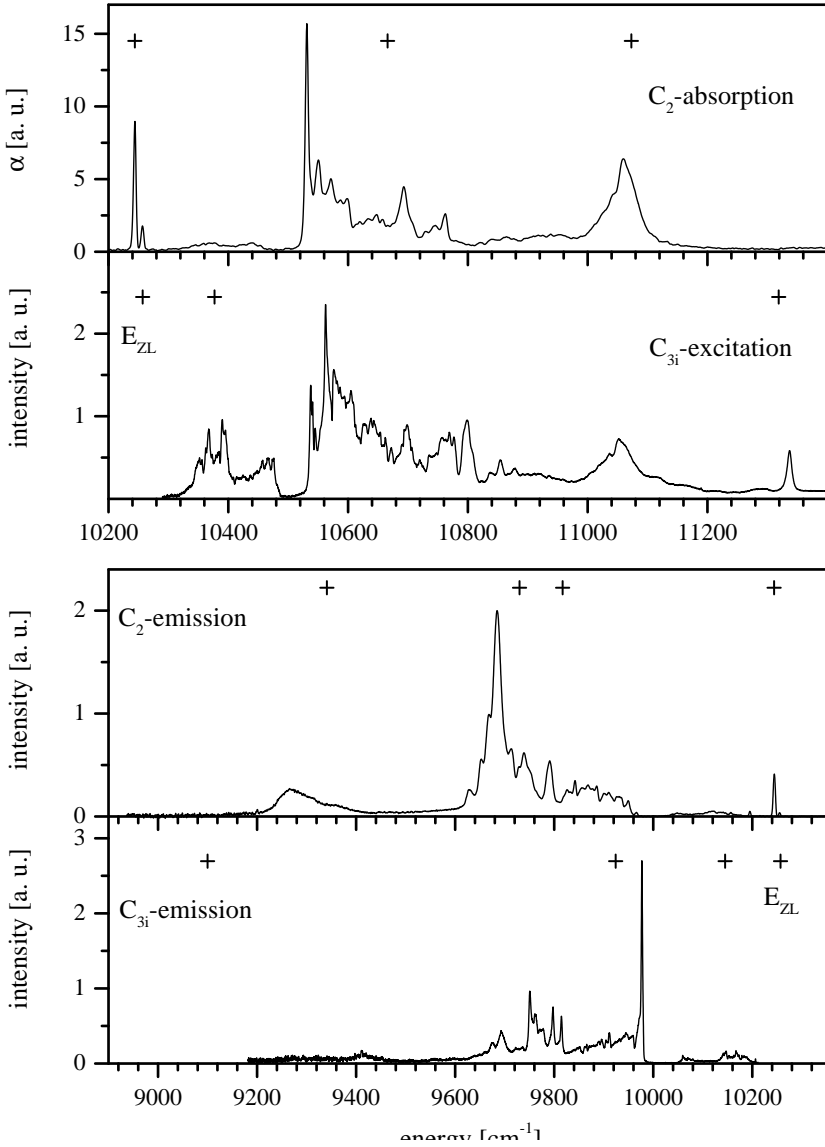
Figure 6.27: Infrared spectra of Yb:Lu$_2$O$_3$ with the Stark-levels (+).

	C_2 $^2F_{7/2}$	C_2 $^2F_{5/2}$ x+	C_{3i} $^2F_{7/2}$	C_{3i} $^2F_{5/2}$ x'+
	[cm^{-1}]	[cm^{-1}]	[cm^{-1}]	[cm^{-1}]
Yb:Sc$_2$O$_3$ C_2: 10260+ C_{3i}: 10271+	0 481 579 1017	0 476 934	0 118 352 1221	0 127 1121
Yb:Y$_2$O$_3$ C_2: 10243+ C_{3i}: 10254+	0 414 498 874	0 408 802	0 108 322 1119	0 116 1027
Yb$_2$O$_3$ C_2: 10242+ C_{3i}: 10254+	0 432 521 914	0 427 839	0 113 337 1171	0 121 1075
Yb:Lu$_2$O$_3$ C_2: 10244+ C_{3i}: 10257+	0 427 514 903	0 422 829	0 112 333 1157	0 120 1062

Table 6.6: Energy levels of Yb:RE$_2$O$_3$ determined from the values for ytterbia.

for lutetia also in figure 6.27. The Stark-components are not necessarily located at the positions of the strongest peaks except for the zero-line. As mentioned before, the impact of electronic-vibronic coupling is very strong in the sesquioxides (see section 4.3.3). The electronic levels are coupled to several vibronic levels which leads to transition bands that have maxima that are shifted away from the original electronic and vibronic levels with shapes similar to those in figures 4.3 and 4.4.

It is notable that for yttria, lutetia, and ytterbia all ratios between the maximum splitting of the C_2- and C_{3i}-ground and excited state levels are identical. In the case of scandia the splittings for the C_{3i}-sites are slightly lower than expected when comparing to the other materials. This indicates that by doping with ytterbium the C_{3i}-lattice site in scandia is enlarged by a different amount than the C_2-site, which causes a slightly different change of the crystal-field strength in contrast to the pure scaling of the lattice constant.

If the newly identified Stark-levels are compared to those published by Mix [mix99] some changes are visible. Table 6.7 shows the previous and new C_2-level energies and the partition functions which are needed to calculate the emission

host	ground-state [cm^{-1}]	$Z_l/2$	excited-state x+ [cm^{-1}]	$Z_u/2$	Z_l/Z_u
Sc$_2$O$_3$	0, 481, 579, 1017	2.318	0, 476, 934	2.214	1.047
Sc$_2$O$_3$ (M)	0, 578, 649, 1116	2.224	0, 374, 935	2.356	0.944
Y$_2$O$_3$	0, 414, 498, 874	2.462	0, 408, 802	2.308	1.067
Y$_2$O$_3$ (M)	0, 479, 528, 941	2.382	0, 275, 784	2.582	0.923
Yb$_2$O$_3$	0, 432, 521, 914	2.418	0, 427, 839	2.278	1.061
Yb$_2$O$_3$ (M)	0, 507, 555, 983	2.334	0, 278, 829	2.564	0.910
Lu$_2$O$_3$	0, 427, 514, 903	2.430	0, 422, 829	2.286	1.063
Lu$_2$O$_3$ (M)	0, 505, 560, 981	2.332	0, 287, 815	2.546	0.917

Table 6.7: Energy levels and partition functions of Yb:RE$_2$O$_3$ C$_2$-
ions in comparison to the values published in [mix99] (M).
The energies of the lowest Stark-components of the excited
state x are given in table 6.6

cross sections. The splitting of the ground-state levels is slightly smaller in the
new set, whereas the splitting of the excited-state is larger except in the case of
scandia. The positions of the second Stark-level of the excited state and the second
and third level of the ground state have shifted drastically in comparison to the
previous values (M) which denoted absorption and emission maxima in the low
temperature spectra. The ratio of the partition functions Z_l/Z_u, which linearly
enters the calculation of the emission cross sections by the reciprocity method, is
10 to 15% larger for the new Stark-levels than for the values from [mix99], which
leads to higher emission cross sections for ytterbium (see table 6.1).

7

Simulation and Experiments with Sesquioxides in the Thin-Disk-Laser-Setup

The thin-disk-laser is a novel pump- and resonator-design for high-power lasers developed by Giesen et al. [gie94]. The active medium is polished to a thin circular disk and coated with a high-reflecting dielectric mirror for the pump and laser wavelengths on the back and with an anti-reflection coating on the front. The disk is then bonded with the HR side to a heat-sink (compare figure 7.1). The resonator is formed by the coated crystal and an output coupler. The pump light is provided by fiber-coupled laser-diodes which are focused onto the crystal. Since the thin crystal-disk only absorbs a small fraction of the pump light during one pass through the crystal, the pump light is reflected back into the disk several times by a parabolic mirror and the folding mirror. Up to a total of 24 pump light passes are currently used. Due to the geometrical setup a nearly one-dimensional thermal profile can be reached within the crystal. The hottest area is the crystal surface, the coolest is the back of the crystal, which is in direct contact to the heat sink. This setup minimizes the formation of thermal lenses at high powers, and therefore extends the applicable power limit to the destruction-limit of the crystal. The thin-disk-laser setup can easily be scaled up by adding more disks to the resonator.

First experiments with ytterbium-doped scandia and lutetia crystals by Mikhail Larionov at the Institut für Strahlwerkzeuge, University of Stuttgart, have shown very promising results with this setup. The high thermal conductivity and mechanical stability help to reach higher powers in this setup. The experiments were
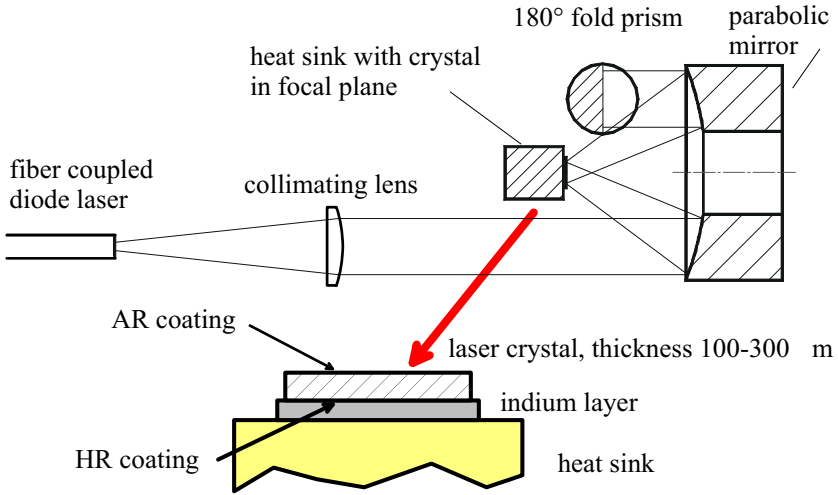
Figure 7.1: Thin-disk laser setup with 24 pump passes [gie94]
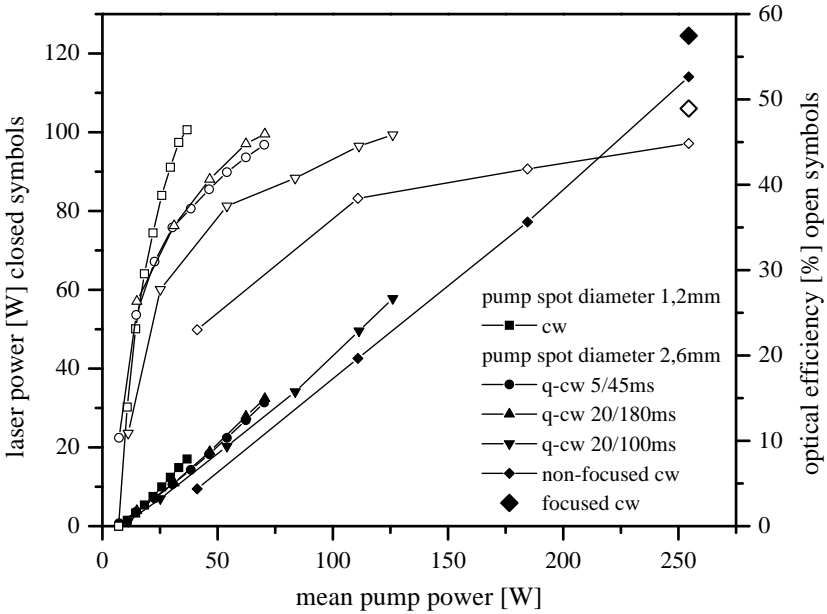
Figure 7.2: Thin-disk laser results of $Yb(2.8\%):Sc_2O_3$
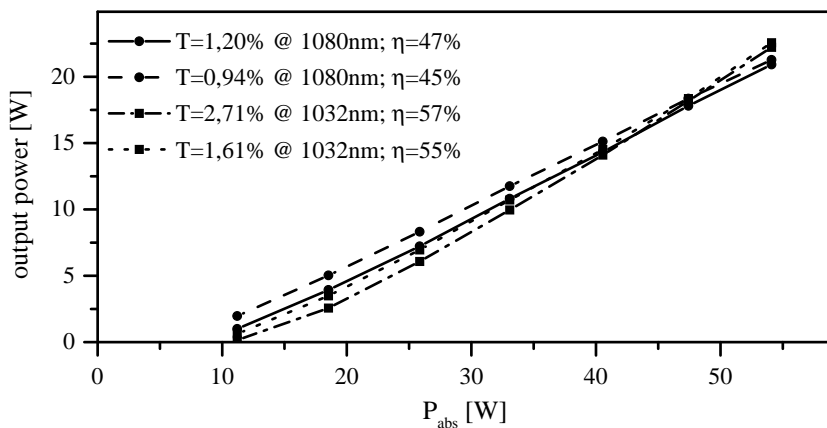
Figure 7.3: Thin-disk laser results of Yb(2.7%):Lu$_2$O$_3$
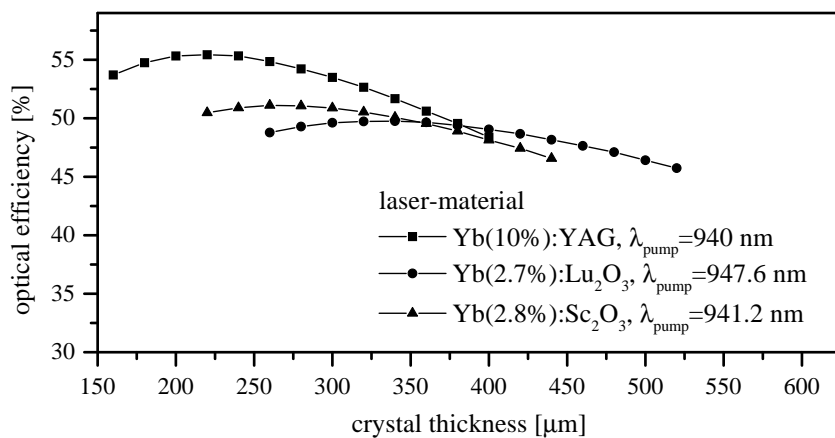
Figure 7.4: Calculated efficiency of the thin-disk laser setup with 940 nm pumping
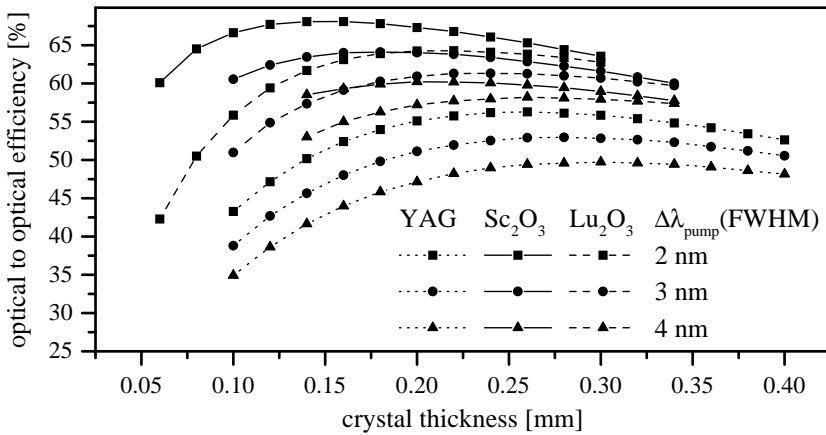
Figure 7.5: Calculated efficiency of the thin-disk laser setup with zero-line pumping

performed using crystals grown by the Bridgman-method in the small Czochralski-growth-setup. The best results were reached with an Yb(2.8%):Sc$_2$O$_3$ crystal. The maximum output power was 124.5 W for 254 W input power at 940 nm resulting in a slope efficiency of 49% (see figure 7.2 single point). The laser wavelength was 1041 nm and the output-coupler had a transmission of 1.7%. Other experiments with quasi-cw pumping at several pumping ratios or somewhat defocused excitation showed slightly lower results. Up to the maximum power no roll-off can be seen, which would indicate overheating of the crystal. A fully optimized Yb:YAG crystal can reach about 60% optical efficiency in a comparable setup. Higher output powers should be possible with this system. The used crystal was damaged when the pump power was accidentally switched to 600 W.

The used Yb(2.7%):Lu$_2$O$_3$ crystal was of low quality. Simulations indicated a quantum efficiency of only 85% for this crystal. Nevertheless, a maximum output power of 22.5 W at 54 W pump power was reached (see figure 7.3). The maximum slope efficiency was 57% for lasing at the emission maximum at 1032 nm and 47% for lasing at 1080 nm. Due to the lower reabsorption losses at 1080 nm the laser wavelength switches to the longer wavelength when low transmission output-coupling mirrors are used [mix99].

Simulations of the laser system by Karsten Contag from the Forschungsgesellschaft für Strahlwerkzeuge mbH in Stuttgart have revealed that the full potential of the sesquioxides is not utilized when the crystals are pumped at 940 nm. Here maximum slope efficiencies of 51% for scandia and 50% for lutetia can be

reached at 35 W of input power (see figure 7.4). Yb:YAG can reach 56% optical efficiency in this setup. The experiments show a good agreement with the simulation except for Yb:Lu$_2$o$_3$, which was calculated with 100% quantum efficiency instead of the actual 85%. However, when the system is pumped at the zero-line the reachable efficiencies rise considerably due to the strong absorption of the zero-line in the sesquioxides (see section 6.1 and figure 7.5). Furthermore, thinner crystals can be used, which reduces the risk of mechanical damage at higher pump powers. With zero-line pumping maximum slope efficiencies of 60% could be reached with scandia if a realistic spectral bandwidth of 4 nm is assumed for the laser diode. If diodes with only 2 nm spectral bandwidth would be available even higher slope efficiencies could be reached. Yb:YAG, which does not have a strong zero-line absorption, shows lower results with zero-line pumping than the sesquioxides but performs better when pumping at 940 nm is used.

8

Conclusion

The subject of the presented work was the enhancement of the growth technique for the high melting sesquioxides scandia, yttria, and lutetia and the spectroscopic characterization of trivalent ytterbium in these crystals beyond the achievements of the previous works by L. Fornasiero, E. Mix, and the author [for99, mix99, pet98].

The high melting points of the sesquioxides of about 2400 C considerably narrow the choice of crucible and insulation materials. Stable growth conditions were reached using rhenium crucibles and zirconia felt mats without direct contact to the hot crucible for insulation. Beyond the earlier tested Czochralski-, Nacken-Kyropoulos-, and Bridgman-growth-methods, which were further used in this work, the heat-exchanger-method (HEM) was introduced as a new growth method for the sesquioxides. First experiments with this method showed that it greatly enhances the possibilities for sesquioxide growth in terms of reachable single crystal size and optical quality. Also it allows fully computerized operation of the crystal growth which is favorable for possible future industrial production of sesquioxides. Until now single crystals with volumes of several cubic centimeters and low mechanical stress were manufactured.

The spectroscopic investigations focused on the identification of the electronic level structure of the ytterbium $4f$-shell in the sesquioxide lattice. Previous attempts by E. Mix have revealed that a clear identification of the levels from standard low temperature absorption and emission measurements is not possible. This is due to the strong electron-phonon-coupling in ytterbium in comparison to other rare-earths which leads to numerous vibronic transitions that can be observed in the ytterbium spectra.

A first attempt to solve this problem was made by applying high hydrostatic pressure on the samples and recording the changes in the optical spectra. Signif-

icant shifts of the spectral features could be observed as expected. However, the measured changes were not sufficient to distinguish between electronic and vibronic levels and it has become obvious that this technique could not be used to make that distinction at the current state of technology.

The study of exchange-coupled ytterbium ions delivered the necessary information for a secure identification of the electronic levels. Exchange coupling between neighboring ions has two intermediate effects on the spectroscopic properties of an ion. The first is a splitting of all electronic levels into two dimer levels, the so called Davydov-splitting, and the second are optical transitions of the coupled system. The Davydov-splitting could only be observed indirectly through a slight line-broadening at high ytterbium concentrations. Estimations of the level splitting showed that the expected splitting of ytterbium levels in the sesquioxides is in the range below 0.5 cm^{-1}, which is smaller than the linewidth of the ytterbium transitions.

The strength of pair effects depends on the density of the pairs in the crystal which is directly coupled to the dopant concentration. The best observations of pair effects were therefore made with pure ytterbia. The second, less controllable, factor for the strength of pair transitions is the separation between the coupled ions. Since the strength of the exchange-coupling between the ions scales exponentially with the distance, small interionic distances are favorable. The sesquioxides with their high cation-density and low interionic distances are therefore excellent hosts for the observation of pair effects.

Absorption of ytterbium pairs in the green spectral region was observed in ytterbia and emission from pairs could be identified in ytterbia and ytterbium-doped scandia. In connection with the pair emission measurements, the visible emissions of various other rare-earths were recorded to compensate for emissions from impurity ions in the starting materials. A side effect of pair transitions is the significant reduction of the electron-phonon coupling compared to single-ion transitions. The reduced electron-phonon coupling allowed the identification of the electronic levels by combining crystal-field calculations with pair and single-ion spectroscopy. The energy levels of the two ytterbium $4f$-manifolds for both symmetry sites in the crystal lattice were directly identified in the case of ytterbia and indirectly set for the other materials by transferring the results to the very similar spectra of the other sesquioxide hosts.

First laser experiments by E. Mix have revealed the high potential of ytterbium-doped sesquioxides as laser materials. The high thermal conductivity, especially in ytterbium-doped lutetia, suggests the use of the sesquioxides in high power laser applications. Recent experiments with ytterbium-doped scandia and lutetia in the thin-disc-laser design with maximum output powers of 124 W cw from Yb:Sc$_2$O$_3$ have confirmed this.

In the future various optimizations and enhancements will have to be made in order to turn the high melting sesquioxides into reliable high power laser materials. Especially the optimization of the growth parameters of the HEM-technique, such as temperature profiles and crucible shape, is necessary to achieve excellent optical crystal quality with highly reliable setups. Also the size scalability of the technique needs to be further explored.

The identification of the ytterbium Stark-levels is at the current point in time very secure. When complete phonon dispersion curves for the sesquioxides become available simulations of the actual electronic-vibronic coupling should be performed to give some further refinement to the exact positioning of the center levels of each manifold, which were only set through crystal-field calculations. The impact of these refinements on the theoretical evaluation of the laser properties of the materials is, however, estimated to be below the error margins of the other measurements required to obtain these values, e. g. in the case of the emission cross sections.

Further laser experiments with ytterbium-doped sesquioxides in the thin-disk-laser setup and as materials for mode-locked operation are currently in planning and will give an evaluation of the crystals grown by the HEM-technique.

When using the materials at higher dopant concentrations, the drastic lifetime shortening that was observed may present a sincere problem. Here further research of the energy transfer processes that cause the quenching are necessary in order to find ways to reduce these effects as far as possible. In direct connection to this, it would be extremely helpful if chemicals of higher purity were available to reduce the density of possible transfer partners.

Aside from ytterbium there are other rare-earths that are very promising dopant-ions for the sesquioxides which could benefit from the now available high crystal quality. Most notable here are neodymium in scandia for operation at 1486 nm which is interesting for the telecommunications industry and erbium in lutetia which is promising for high power operation at 2.7 μm for medical applications because of the strong upconversion in the erbium-doped sesquioxides and the high thermal fracture limit of the crystals.

Appendix A

Distribution Coefficients

The following table shows the distribution coefficients for several rare-earth dopants in the high melting sesquioxides. The values have been measured with crystals grown by the Czochralski method and should be valid for growth methods using a slow crystallization rate. When high crystallization rates in the range of several millimeters per second are employed the distribution coefficients are close to unity for all rare-earth dopants [bol01].

Ion	Sc_2O_3	Y_2O_3	Lu_2O_3
Pr	0.04	< 1	< 1
Nd	0.03	0.9	0.7
Ho	0.4	≈ 1	≈ 1
Er	0.4	≈ 1	≈ 1
Tm	0.5	≈ 1	≈ 1
Yb	0.56	≈ 1	≈ 1

Appendix B

Stark-Levels of Rare-Earth-Doped Sesquioxides

All values are given in cm^{-1}. Unless otherwise noted only the energy levels for ions in C$_2$ sites are given. The values in [...] are calculated, those in (...) could not be securely determined.

Ce^{3+}:Y$_2$O$_3$	^{2}F$_{5/2}$:	0, [651], [1128]
[cha82]	^{2}F$_{7/2}$:	2182, 2750, 3061, 3880
Pr^{3+}:Sc$_2$O$_3$	^{3}H$_4$:	0, 104, 316, 433, 555, 778, 1047, 1111, 1431
[pet98]	^{3}H$_5$:	-
	^{3}H$_6$:	4265, 4290, 4329, -, -, 4642, 4717, 4717, 4769, 4958, 5020, 5134, 5146, 5297
	^{3}F$_2$:	5432, 5541, 5633, 5773, 5902
	^{3}F$_3$:	6419, 6591, 6672, 6707, 6885, 6928, 7045
	^{3}F$_4$:	7149, 7246, 7330, 7343, 7381, 7490, 7560, 7610, 7756
	^{1}G$_4$:	9791, 9805, 9884, 9931, 9973, 10021, 10081, 10242, 10386
	^{1}D$_2$:	15960, 16296, 16795, 17107, 17345
	^{3}P$_0$:	19687
	^{3}P$_1$:	20024, 20115, 20437
	^{1}I$_6$:	20492, 20525, 20570, 20636, 20672, 20851, 20921, 21070, 21151, 21462, 20605, 21894, 21974
	^{3}P$_2$:	22406, 22805, 22912, 22957, 23034
Pr^{3+}:Y$_2$O$_3$	^{3}H$_4$:	0, 108, 291, 345, 635, 709, [914], 919, 1141

[cha82, pet98]	$^3H_5$:	2207, 2226, 2310, [2359], 2675, 2702, 2754, 2773, 2906, 2973, [3112]
	$^3H_6$:	4284, 4303, 4364, 4382, 4524, [4683], 4771, 4877, 4910, 4947, 5078, [5104], 5237
	$^3F_2$:	5340, 5440, 5500, 5607, 5712
	$^3F_3$:	6501, 6654, [6679], 6730, 6790, 6812, 6931
	$^3F_4$:	7067, [7120], [7143], 7188, 7227, 7271, [7499], [7598], 7601
	$^1G_4$:	9810, [9814], 9932, 9972, 10011, 10041, 10660, 10713, [11006]
	$^1D_2$:	16156, 16423, 16867, 17159, 17362
	$^3P_0$:	20028
	$^3P_1$:	20278, 20314, 20440
	$^1I_6$:	20643, 20672, 20719, 20771, 20883, 20894, 20953, 21018, 21113, 21309, 21657, 21840, 22087
	$^3P_2$:	22506, 22701, 22789, 22885, 23096
Pr^{3+}:Lu_2O_3	$^3H_4$:	0, 112, 292, 352, 663, 746, 953, 956, (1014)
[pet98]	$^3H_5$:	-
	$^3H_6$:	4279, 4301, 4352, -, 4519, 4693, 4769, 4891, 4929, -, 5092, 5179, 5249
	$^3F_2$:	5360, 5460, 5529, 5642, 5754
	$^3F_3$:	6445, 6656, 6715, 6740, 6807, 6837, 6952
	$^3F_4$:	7082, 7171, (7171), 7276,, 7243, 7284, 7519, 7609, 7635
	$^1G_4$:	9812, 9935, 9975, 10019, 10057, 10669, 10699, 10763
	$^1D_2$:	16122, 16404, 16868, 17164, 17374
	$^3P_0$:	19969
	$^3P_1$:	20097, 20274, 20389
	$^1I_6$:	20614, 20631, 20700, 20751, 20833, 20925, 20960, 21066, 21204, 21286, 21645, 21796, 22070
	$^3P_2$:	22491, 22728, 22831, 22894, 23100
Nd^{3+}:Sc_2O_3	$^4I_{9/2}$:	0, 36, 356, 532, 797
[for99]	$^4I_{11/2}$:	1900, 1942, 2240, 2352, 2438, 2473
	$^4I_{13/2}$:	3791, 3822, 4170, 4259, 4374, 4412, 4435
	$^4I_{15/2}$:	5421, 5671, 6121, 6194, 6506, 6561, 6623 (measured at 300K)
	$^4F_{3/2}$:	11152, 11394
	$^4F_{5/2}$:	12117, 12269, 12372
	$^2H_{9/2}$:	12416, 12491, 12569, 12651, 12718
	$^4F_{7/2}$ / $^4S_{3/2}$:	13137, 13285, 13370, 13397, 13422, 13513
	$^4F_{9/2}$:	14374, 14502, 14553, 14715
	$^2H_{11/2}$:	15717, 15808, 15973, 16061, 16149, 16322 (measured at 300K)
	$^4G_{5/2}$:	16488, 16660, 16835
	$^4G_{7/2}$:	17047, 17178, 17198, 17292
	$^2G_{7/2}$:	18315, 18450, 18579, 18641
Nd^{3+}:Y_2O_3	$^4I_{9/2}$:	0, 27, 267, 447, 640
[cha82, for99]	$^4I_{11/2}$:	1891, 1928, 2141, 2259, 2325, 2350

	$^4I_{13/2}$:	3802, 3826, 4082, 4187, 4270, 4296, 4318
	$^4I_{15/2}$:	5520, 57006, 5866, -, 6052, 6150, 6393, 6444 (measured at 300K)
	$^4F_{3/2}$:	11208, 11405
	$^4F_{5/2}$:	12189, 12323, 12396
	$^2H_{9/2}$:	12437, 12492, 12554, 12644, 12704
	$^4F_{7/2} / {}^4S_{3/2}$:	13182, 13308, 13390, 13415, 13498
	$^4F_{9/2}$:	14426, 14505, 14532, 14570, 14721
	$^2H_{11/2}$:	15721, 15809, 15866, 15934, 15986, 16111 (measured at 300K)
	$^4G_{5/2}$:	16581, 16735, 16762
	$^4G_{7/2}$:	16903, 17113, 17209, 17310
	$^2G_{7/2}$:	-
Nd^{3+}:Lu$_2$O$_3$ [for99]	$^4I_{9/2}$:	0, 32, 287, 470, 685
	$^4I_{11/2}$:	1894, 1931, 2136, 2283, 2356, 2384
	$^4I_{13/2}$:	3802, 3825, 4103, 4208, 4299, 4326, 4348
	$^4I_{15/2}$:	5483, 5505, 5699, 6201, 6289, 6386, 6457, 6537 (measured at 300K)
	$^4F_{3/2}$:	11199, 11404
	$^4F_{5/2}$:	12176, 12314, 12396
	$^2H_{9/2}$:	12438, 12501, 12557, 12650, 12711
	$^4F_{7/2} / {}^4S_{3/2}$:	13173, 13310, 13389, 13414, 13423, 13506
	$^4F_{9/2}$:	14410, 14529, 14571, 14729, 14889
	$^2H_{11/2}$:	15694, 15710, 15746, 15856, 15939
	$^4G_{5/2}$:	16564, 16709, 16739
	$^4G_{7/2}$:	16885, 17097, 17204, 17313
	$^2G_{7/2}$:	18432, 18560, 18684, 18709
Sm^{3+}:Y$_2$O$_3$ [cha82]	$^6H_{5/2}$:	0, 200, 456
	$^6H_{7/2}$:	1101, 1339, 1361, 1528
	$^6H_{9/2}$:	2306, 2447, 2536, 2596, 2748
	$^6H_{11/2}$:	3630, 3731, 3780, 3818, 3964, 4077
	$^6H_{13/2}$:	5012, 5054, 5079, 5169, 5246, 5448, 5561
	$^6F_{1/2} / {}^6H_{15/2} /$	6214, [6336], 6482, 6539, [6606], 6753, 6823, 6844,
	$^6F_{3/2}$:	6921, [7028], [7126]
	$^6F_{5/2}$:	7283, 7345, 7422
	$^6F_{7/2}$:	8142, 8169, 8174, 8294
	$^6F_{9/2}$:	9283, 9313, 9354, 9383, 9427
	$^6F_{11/2}$:	10568, 10663, 10692, 10750, 10775, 10877
	$^4F_{5/2}$:	17557, 17698, 17837
	$^4F_{3/2}$:	18826, 18839
	$^4G_{7/2}$:	19771, 19938, 19957, 20076
Eu^{3+}:Y$_2$O$_3$ [cha82]	$^7F_0$:	0
	$^7F_1$:	199, 360, 543
	$^7F_2$:	859, 906, 949, [1226], 1380
	$^7F_3$:	1847, 1867, 1907, [1946], 2021, 2130, 2160
	$^7F_4$:	2669, 2800, 2846, 3014, 3080, 3119, 3163, 3178, 3190

	$^7F_5$:	3755, [3785], 3825, [3888], 3904, 3938, 4015, 4127, [4211], 4227, [4248]
	$^7F_6$:	4791, 4812, 5032, [5038], 5045, [5038], 5045, [5073], 5271, [5300], 5314, [5445], 5459, [5634], 5636
	$^5D_0$:	17216
	$^5D_1$:	18930, 18954, 18992
	$^5D_2$:	21355, 21367, 21394, 21487, 21503
	$^5D_3$:	24258, 24267, 24284, [24293], [24302], (24330), 24354
C_{3i} [gru85, heb70]	$^7F_0$:	0
	$^7F_1$:	132, 429
	$^7F_2$:	827, 948, 1188
	$^5D_0$:	17302
	$^5D_1$:	18991, 19080
$Tb^{3+}:Y_2O_3$ [cha82]	$^7F_6$:	0, 3, 228, 243, 321, 362, 410, 484, 536, 543, 568, [816], [824]
	$^7F_5$:	2272, 2274, 2314, 2377, 2494, 2551, 2607, 2616, [2684], 2706, 2746
	$^7F_4$:	3571, 3576, 3635, 3646, 3737, 3757, 3946, 3999, 4056
	$^7F_3$:	4602, 4622, 4700, 4787, 4811, 4844, 4882
	$^7F_2$:	5220, 5381, 5613, 5674, 5708
	$^7F_1$:	5840, 5998, 6167
	$^7F_0$:	6279
	$^5D_4$:	20661, 20667, 20721, 20725, 20784, 20792, 20843, 20851, 20868
$Dy^{3+}:Y_2O_3$ [cha82]	$^6H_{15/2}$:	0, 73, 262, 370, 501, 608, 727, 833
	$^6H_{13/2}$:	3595, 3684, 3854, 3893, 3963, 4020, 4046
	$^6H_{11/2}$:	5948, 6090, 6186, 6213, 6237, 6370
	$^6F_{11/2}$ / $^6H_{9/2}$:	7758, 7829, 7847, 7930, 7949, 8008, 8015, 8048, 8209, 8248, 8393
	$^6H_{5/2}$:	10336, 10509, 10624
	$^6F_{7/2}$:	11236, 11292, 11331, 11383
	$^6F_{5/2}$:	12586, 12669, 12738
	$^6F_{3/2}$:	13455, 13468
	$^6F_{1/2}$:	14005
	$^4F_{9/2}$:	21039, 21064, 21132, 21340, 21489
	$^4I_{15/2}$:	21911, 21952, 22010, 22085, 22391, 22399, 22406, 22471
	$^4G_{11/2}$:	23405, 23547, 23616, 23661, 23697, 23780
C_{3i} [gru85]	$^6H_{15/2}$:	0, 66, 186, 326, 423, 606, 682, 740
	$^6H_{13/2}$:	3200, [3330], 3450, 3562, 3695, 3740, 3785
$Ho^{3+}:Sc_2O_3$ [moh00]	$^5I_8$:	0, 1, 11, 12, 289, 297, 361, 368, -, 440, 450, (463), 474, -, (524), 531, 552
	$^5I_7$:	5183, -, 5213, 5236, 5253, 5342, 5349, 5358, 5369, 5381, 5390, 5416, 5499, 5512

	$^5I_6$:	(8669), -, -, 8695, 8738, 8746, (8817), 8852, 8860, 8885, 8895, 8950, 8961
	$^5I_5$:	10729, -, 10799, -, 10823, -, 10894, 10921, 10953, 11090, 11270
	$^5I_4$:	13177, -, -, 13344, -, -, 13516, 13580, - (measured at 300K)
	$^5F_5$:	15289, 15392, 15452, -, -, -, -, 15560, 15600, 15719
	$^5S_2 / {}^5F_4$:	18338, -, 18401, -, 18426, 18460, 18508, 18542, 18577, 18587, 18600, 18657, 18665
	$^5F_3$:	20393, 20497, 20503, 20524, (20584), 20629, 20671
$Ho^{3+}:Y_2O_3$ [lea82]	$^5I_8$:	0, 2, 10, 11, 214, 221, 283, 297, [351], 362, 367, 378, (392), 425, 438, 452, 460
	$^5I_7$:	5157, 5157, 5180, 5181, 5288, 5289, 5306, [5309], 5347, 5348, 5377, 5382, 5414, 5418, 5430
	$^5I_6$:	8669, 8669, [8708], 8711, 8746, 8762, 8792, 8800, 8833, 8838, 8882, 8897, 8904
	$^5I_5$:	11241, 11244, 11294, 11306, 11318, 11328, 11365, 11368, 11401, 11409, 11435
	$^5I_4$:	13233, 13243, 13320, 13323, 13381, [13415], 13523, [13570], [13620]
	$^5F_5$:	15328, 15349, 15400, 15405, 15415, 15462, 15555, 15574, 15601, 15690
	$^5S_2 / {}^5F_4$:	18367, 18375, 18419, 18421, 18436, 18470, 18492, 18514, 18542, 18545, 18553, 18586, 18649
	$^5F_3$:	20426, 20532, 20545, 20622, 20640, 20677, 20710
$Ho^{3+}:Lu_2O_3$ [moh00]	$^5I_8$:	0, 1, 10, 10, -, 232, 238, -, 315, 390, 397, 406, 413, 455, 466, 479, 486
	$^5I_7$:	5165, -, 5189, -, 5310, 5322, 5340, 5348, 5355, 5365, 5398, 5413, 5429, 5438, 5450
	$^5I_6$:	8670, 8678, -, 8717, 8724, 8797, 8805, 8810, 8844, 8847, 8894, 8910, 8915
	$^5I_5$:	11250, -, -, 11307, -, -, -, -, -, -, -
	$^5I_4$:	-
	$^5F_5$:	15314, 15326, 15335, 15395, 15405, 15416, 15456, 15466, 15589, 15606, 15704
	$^5S_2 / {}^5F_4$:	18365, 18371, 18414, 18430, 18440, 18474, 18493, 18514, 18526, 18542, 18556, 18585, 18596, 18652
	$^5F_3$:	20423, 20526, 20549, -, -, 20681, 20710
$Er^{3+}:Sc_2O_3$ [pir67, pet98]	$^4I_{15/2}$	0, 39, 75, 96, 190, 282, 604, (604)
	$^4I_{13/2}$	6516, 6547, 6594, 6604, 6697, 6905, 6936
	$^4I_{11/2}$	10192, 10212, 10245, 10264, 10393, 10412
	$^4I_{9/2}$	12281, 12419, 12514, 12588, 12629
	$^4F_{9/2}$	15067, 15167, 15256, 15323, 15457
	$^4S_{3/2}$	18147, 18278
	$^2H_{11/2}$	19001, 19046, 19082, 19179, 19214, 19242
	$^4F_{7/2}$	20292, 20408, 20488, 20569
	$^4F_{5/2}$	21973, 22009, 22131

	$^4F_{3/2}$	22349, 22538
	$^2H_{9/2}$	24300, 24456, 24497, 24550, 24609
	$^4G_{11/2}$	25981, 26062, 26153, 26342, 26359, 26439
$Er^{3+}:Y_2O_3$	$^4I_{15/2}$	0, 39, 76, 89, 158, 258, 490, 510
[cha82, pet98]	$^4I_{13/2}$	6510, 6542, 6588, 6594, 6684, 6840, 6867
	$^4I_{11/2}$	10193, 10214, 10244, 10264, 10361, 10379
	$^4I_{9/2}$	12324, 12436, 12512, 12576, 12604
	$^4F_{9/2}$	15120, 15199, 15280, 15333, 15436
	$^4S_{3/2}$	18231, 18318
	$^2H_{11/2}$	19038, 19045, 19072, 19187, 19218, 19243
	$^4F_{7/2}$	20346, 20442, 20511, 20575
	$^4F_{5/2}$	22046, 22072, 22172
	$^4F_{3/2}$	22372, 22493
	$^2H_{9/2}$	24364, 24485, 24522, 24554, 24608
	$^4G_{11/2}$	26091, 26115, 26207, 26388, 26399, 26459
C_{3i}	$^4I_{15/2}$	0, 41, 80, 328, 359, 391, 416, 485
[gru85]	$^4I_{13/2}$	6514, 6540, 6610, 6695, 6739, 6791, 6807
$Er^{3+}:Lu_2O_3$	$^4I_{15/2}$	0, 39, 76, 91, 172, 272, 501, 532
[pet98]	$^4I_{13/2}$	6510, 6547, 6593, 6602, 6695, 6862, 6887
	$^4I_{11/2}$	10192, 10213, 10244, 10265, 10366, 10385
	$^4I_{9/2}$	12311, 12427, 12510, 12579, 12612
	$^4F_{9/2}$	15109, 15193, 15275, 15333, 15439
	$^4S_{3/2}$	18207, 18290
	$^2H_{11/2}$	18974, 19015, 19051, 19130, 19168, 19227
	$^4F_{7/2}$	20317, 20416, 20483, 20555
	$^4F_{5/2}$	22022, 22052, 22156
	$^4F_{3/2}$	22381, 22548
	$^2H_{9/2}$	24334, 24459, 24501, 24540, 24588
	$^4G_{11/2}$	26048, 26082, 26185, 26350, 26392, 26427
$Tm^{3+}:Sc_2O_3$	$^3H_6$	0, -, 78, -, 305, -, 403, 545, 566, 621, 655, 991
[for99]	$^3F_4$	5636, 5695, 5826, 6089, 6101, 6176, 6207, 6238, 6253
	$^3H_5$	8273, 8283, 8324, 8328, 8340, 8500, 8509, 8518, 8600, 8817, 8855
	$^3H_4$	12553, 12706, 12826, 12942, 12960, 13133, 13196, -, -
	$^3F_3$	14633, 14688, -, 14724, 14742, 14832, -
	$^3F_2$	15008, 15090, 15186, 15263, 15330
$Tm^{3+}:Y_2O_3$	$^3H_6$	0, 31, 91, 220, 231, 340, 379, 432, 435, 488, 508, 592, 792
[lea82, for99]	$^3F_4$	5612, 5676, 5773, 610, 6022, 6105, 6117, 6149, 6194
	$^3H_5$	8003, 8240, 8268, 8280, 8311, 8341, 8472, 8478, 8570, 8760, 8904
	$^3H_4$	12560, 12640, 12702, 12820, 12874, 12890, 12914, 13020, 13050
	$^3F_3$	14574, 14629, -, 14666, 14733, 14829, -
	$^3F_2$	15000, 15069, 15194, 15214, 15247, 15364

Tm^{3+}:Lu$_2$O$_3$	^{3}H$_6$	0, 36, 89, 232, 245, 354, 392, 457, 467, 510, 527, 760, 835
[for99]	^{3}F$_4$	5613, 5680, 6033, 6045, 6127, 6141, 6174, 6223
	^{3}H$_5$	8232, 8267, 8282, 8303, 8318, 8340, 8475, 8487, 8578, 8785, 8938
	^{3}H$_4$	12562, 12710, 12831, 12915, 12936, 13080, 13140, 13254, 13484
	^{3}F$_3$	14558, 14592, 14688, 14695, 14760, 14841, 14922
	^{3}F$_2$	15029, 15080, 15213, 15272, 15390
Yb^{3+}:Sc$_2$O$_3$	^{2}F$_{7/2}$	0, 481, 579, 1017
	^{2}F$_{5/2}$	10260, 10736, 11194; 10260+: 0, 476, 934
C$_{3i}$	^{2}F$_{7/2}$	0, 118, 352, 1221
	^{2}F$_{5/2}$	10271, 10398, 11392; 10271+: 0, 127, 1121
Yb^{3+}:Y$_2$O$_3$	^{2}F$_{7/2}$	0, 414, 498, 874
	^{2}F$_{5/2}$	10243, 10651, 11045; 10243+: 0, 408, 802
C$_{3i}$	^{2}F$_{7/2}$	0, 108, 322, 1119
	^{2}F$_{5/2}$	10254, 10370, 11281; 10254+: 0, 116, 1027
Yb$_2$O$_3$	^{2}F$_{7/2}$	0, 432, 521, 914
	^{2}F$_{5/2}$	10242, 10669, 11081; 10242+: 0, 427, 839
C$_{3i}$	^{2}F$_{7/2}$[1]	0, 113, 337, 1171
	^{2}F$_{5/2}$[2]	10254, 10375, 11329; 10254+: 0, 121, 1075
Yb^{3+}:Lu$_2$O$_3$	^{2}F$_{7/2}$	0, 427, 514, 903
	^{2}F$_{5/2}$	10244, 10666, 11073; 10244+: 0, 422, 829
C$_{3i}$	^{2}F$_{7/2}$	0, 112, 333, 1157
	^{2}F$_{5/2}$	10257, 10377, 11319; 10257+: 0, 120, 1062

---

[1]estimated from Yb:Lu$_2$O$_3$ spectra and pair-emission spectra
[2]calculated from pair-absorption and Yb:Lu$_2$O$_3$ spectra

Appendix C

Calculation of the Coupling between Electronic and Vibronic Levels

The following Mathcad script adapted from [mix99] was used for the calculation of the coupling between electronic and vibronic levels. $H = H_R + H_I$ describes the coupling between the electronic level at the energy E_{el} to the vibronic levels E_1, E_2, and E_3. The coupling constants for the three levels are V_{elvib1}, V_{elvib2}, and V_{elvib3}. The shape of the coupled transition S is a superimposition of three Lorentz-profiles, defined by the components of the electronic eigenstate, the eigenvalues of the coupling-matrix, and the mixed line-widths.

$$
H_R(E_{el}, E_1, E_2, E_3, V_{elvib1}, V_{elvib2}, V_{elvib3}) :=
$$
$$
\begin{pmatrix}
E_{el} & V_{elvib1} & V_{elvib2} & V_{elvib3} \\
V_{elvib1} & E_1 & 0 & 0 \\
V_{elvib2} & 0 & E_2 & 0 \\
V_{elvib3} & 0 & 0 & E_3
\end{pmatrix}
\tag{C.1}
$$

$$
H_I(\Gamma_{el}, \Gamma_V) :=
\begin{pmatrix}
\Gamma_{el} & 0 & 0 & 0 \\
0 & \Gamma_V & 0 & 0 \\
0 & 0 & \Gamma_V & 0 \\
0 & 0 & 0 & \Gamma_V
\end{pmatrix}
\tag{C.2}
$$

$$S(E, E_{el}, E_1, E_2, E_3, V_{elvib1}, V_{elvib2}, V_{elvib3}, \Gamma_{el}, \Gamma_V) := \qquad\qquad (C.3)$$

$\quad\Big|\; MM \leftarrow H_R(E_{el}, E_1, E_2, E_3, V_{elvib1}, V_{elvib2}, V_{elvib3}) + H_I(\Gamma_{el}, \Gamma_V)$

$\quad\;\;\; V_{cpx} \leftarrow \text{eigenvecs}(MM)$

$\quad\;\;\; amp \leftarrow V_{cpx}^{-1} \cdot (MM) \cdot V_{cpx}$

$\quad\;\;\; \text{for } i \in 0..3$

$\qquad\Big|\; e_i \leftarrow amp_{i,i}$

$\qquad\;\;\; a_{el_i} \leftarrow V_{cpx_{0,i}}$

$\quad\;\;\; SS \leftarrow 0$

$\quad\;\;\; \text{for } i \in 0..3$

$\quad\;\;\; SS \leftarrow SS + \dfrac{\left(\left|a_{el_i}\right|\right)^2 \cdot (e_i)}{(Re(e_i) - E)^2 + (Im(e_i))^2}$

$\quad\;\;\; \text{return } SS$

Appendix D

Intrinsic Optical Bistability

Intrinsic optical bistability (IOB) is the existence of two stable fluorescence extraction intensity states for one excitation power depending on the excitation history of the system without use of an optical resonator. If a crystal that shows IOB is excited at a certain wavelength and temperature, the measured fluorescence intensity is lower in a certain excitation power region when the crystal is excited with a slowly rising input power than when the excitation power is slowly lowered from a high value (compare figure D.1). This behaviour could be used for an all optical switch which is highly interesting for the telecommunication industry.

IOB has been observed in several semiconductors and in the pair-fluorescence of some ytterbium-doped crystals and was first demonstrated by Hajto et al. in 1983 [haj83] in GeSe$_2$. IOB with ytterbium was first observed in 1994 by Hehlen et al. in Yb(10%):Cs$_3$Y$_2$Br$_9$ [heh94]. In Yb the bistability appears in the pair-fluorescence (see section 4.2) if the crystal is excited at certain wavelengths in the infrared usually at low temperatures. Several attempts have been made to explain this phenomenon. IOB due to local-field correction effects by a saturation of the polarization of the ions neighboring the active ion has been predicted by Bowden and Sung in 1979 [bow79]. Another model to explain the same data by photon avalanche excitation was brought up by Hehlen et al. in 1996 [heh96]. Both models were equally able to explain the available data at the time.

Recent experiments by Gamelin et al. with various ytterbium-doped cesium and rubidium bromides and chlorides, however, revealed data that could not be explained by the earlier models [gam00]. The crystals were excited with continuous and square wave light of adjustable power. The experiments with decreasing excitation power showed that the fluorescence power did not switch from the upper hysteresis branch to the lower when the excitation power was chopped with
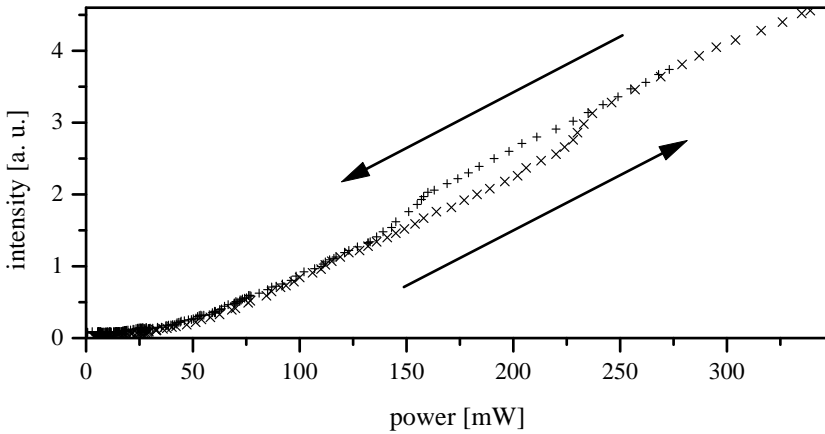
Figure D.1: Bistability in Yb(6%):Sc$_2$O$_3$

a dark-time of several milliseconds, which is considerably longer than the life-time of the ytterbium ions. This led to a completely new explanation for the IOB phenomenon in ytterbium-doped systems. The bistability occurs if an absorption line is excited that shows a strong temperature dependence of the main absorption wavelength. When this line is excited at its correct edge[1] and the local temperature in the crystal rises due to the absorbed excitation power the absorption line shifts and more excitation energy is absorbed which, in turn, leads to a rise in the cooperative fluorescence. When starting with high excitation powers the crystal is first heated strongly and does not reach the same temperature when the excitation power is lowered to a certain point, that it would have when the excitation power is raised slowly to that point from a low starting value. When the excitation power is interrupted for a short period the crystal does not have the time to cool down enough to switch back to the lower branch when the excitation is restarted. This model is able to explain the time dependent behaviour of the system as well as the very narrow excitation wavelength and temperature conditions that have to be met in order to observe bistability.

Intrinsic optical bistability has been observed in ytterbium-doped sesquioxides in cooperation with M. A. Noginov from Norfolk State University. Figure D.1 shows a bistability experiment conducted with Yb(6%):Sc$_2$O$_3$. The experiment was carried out at room temperature with a pumping wavelength of 973.8 nm which corresponds to the shoulder of the zero-line (see section 6.1). The hystere-

---

[1]depending on the direction of the thermally induced line-shift

sis behaviour of the bistability can clearly be seen between 150 mW and 230 mW excitation power. The fluorescence was detected at 487 nm. No intrinsic optical bistability was observed at other pumping or detection wavelengths.

The fact that switching between the upper and lower branch only takes place on a millisecond timescale disqualifies ytterbium-doped system for fast optical switching. Other materials however may show a faster time dependence, especially if one of the two early models [bow79, heh96] applies to the bistability in those systems. When using systems that apply to the model by Gamelin et al. optical switching cannot be achieved at the high frequencies required by the telecommunication market.

Bibliography

[ale78]   V. I. Aleksandrov, V. V. Osiko, A. M. Prokhorov and V. M. Tatarintsev
          Synthesis and Crystal Growth of Refractory Materials by RF Melting in a Cold Container
          1978 (North-Holland Publishing Company Current Topics in Materials Science, Volume I).

[all99]   All-Chemie Ltd. analysis of 4N Lu_2O_3 batch # 1854A (1999).

[and01]   K. Anduleit
          A holographic approach to point defect structures in inorganic crystals: Er doped Sc_2O_3
          to be published (2001).

[ash76]   N. W. Ashcroft, I. Mermin and N. David
          Solid State Physics
          Harcourt Brace College Publishers (1976).

[aul82]   B. F. Aull and H. P. Jenssen
          Vibronic Interactions in Nd:YAG Resulting in Nonreciprocity of Absorption and Stimulated Emission Cross Sections
          IEEE J. of Quant. Electr. **QE-18** (5), 925 (1982).

[bar57]   C. Bárta, F. Petru and B. Hájek
          Über die Darstellung des Einkristalls von Scandiumoxyd
          Die Naturwissenschaften **45**, 36 (1957).

[ber68]   M. F. Berard, C. D. Wirkus and D. R. Wilder
          Diffusion of Oxygen in Selected Monocrystalline Rare Earth Oxides
          J. of The Am. Cer. Soc. **51** (11), 643–647 (1968).

[blo66]   J. Blok and D. A. Shirley
          Systematic Variation of Quadrupole Crystal-Field Shielding in Rare-Earth Ethyl Sulfates
          Rhys. Rev. **143**, 278 (1965).

[blo72]   D. Bloor and J. R. Dean
          Spectroscopy of rare earth oxide systems: I. Far infrared spectra of the rare earth sesquioxides, cerium dioxide, and nonstochiometric praseodymium and terbium oxides
          J. Phys. C (Solid State) **5**, 1237 (1972).

[bog77]   G. A. Bogomolova, L. A. Bumagina, A. A. Kaminskii and B. Z. Malkin
          Crystal field in laser garnets with TR3+ ions in the exchange charge model
          Sov. Phys. Solid State **19**, 1428 (1977).

[bog76]   G. A. Bogomolova, D. H. Vylegzhanin and A. A. Kaminskii
          Spectral and lasing investigations of garnets with Yb^{3+} ions
          Sov. Phys. JETP **42**, 440 (1976).

[bol01]   A. Bolz
          Energietransfer in Ytterbium-dotierten Sesquoxiden
          Master's thesis, Institute of Laser-Physics, University of Hamburg, Germany (2001).

[bon00]   C. Bonner and M. A. Noginov
          private communication.

[bou82]   C. Boulesteix
          Defects and phase transformation near room temperature in rare earth sesquioxides
          In *Handbook on the physics and chemistry of rare earths*, editor K. A. Gschneider Jr. and L. Eyring, North-Holland Publishing Company, chapter 44, pages 321–386 (1982).

[bow79]   C. M. Bowden and C. C. Sung
          First- and second-order phase transitions in the Dicke model: Relation to optical bistability
          Phys. Rev. A **19**, 2392 (1979).

[bra67]   M. I. Bradbury and D. J. Newman
          cited from tro01
          Chem. Phys. Lett. **1**, 44 (1967).

[bra01]   K. L. Bray
           High Pressure Probes of Electronic Structure and Luminescence Properties of Transition Metal and Lanthanide Systems
           Topics in Current Chemistry **213**, 1 (2001).

[buc67]   R. A. Buchanan, K. A. Wickersheim, J. J. Pearson and G. F. Herrmann
           Energy Levels of Yb^{3+} in Gallium and Aluminum Garnets. I. Spectra
           Phys. Rev. **159**, 245 (1967).

[bun98]   C. Bungenstock et al.
           Study of the energy level scheme of Pr^{3+}:LaOCl
           J. Phys. Condens. Matter **10**, 9328–9342 (1998).

[bur62]   G. Burns
           Shielding and Crystal Fields at Rare-Earth Ions
           Phys. Rev. **128** (5), 2121–2130 (1962).

[bur72]   A. I. Burshtein
           Hopping Mechanism of Energy Transfer
           Sov. Phys. LETP **35** (5), 882 (1972).

[cha63]   N. C. Chang
           Fluorescence and Stimulated Emisson from Trivalent Europium in Yttrium Oxide
           J. Appl. Phys. **34**, 3500 (1963).

[cha82]   N. C. Chang, J. B. Gruber, R. P. Leavitt and C. A. Morrison
           Optical spectra, energy levels, and crystal-field analysis of tripositive rare earth ions in Y_2O_3. I. Kramers ions in C_2 sites
           J. Chem. Phys. **76** (8), 3877–3889 (1982).

[che90]   C. Chen, B. M. Wanklyn and P. Ramasamy
           The Flux Growth of Scandium Oxide Crystals
           J. of Crystal Growth **104**, 672 – 676 (1990).

[con51]   E. U. Condon and H. G. Shortley
           Theory of Atomic Spectra
           Cambridge University Press (1951).

[del80]   A. J. DeLai and C. P. Gazzara
           Growing doped single crystal materials
           US Patent No. 4,186,046 (Jan. 1980).

[del94] L. D. DeLoach, S. A. Payne, L. K. Smith, W. L. Kway and W. F. Krupke
Laser and spectroscopic properties of $Sr_5(PO_4)_3F$:Yb
J. Opt. Soc. Am. B **11**, 269 (1994).

[dex53] D. L. Dexter
A Theory of Sensitized Luminescence in Solids
J. Chem. Phys. **21**, 836 (1953).

[ein16] A. Einstein
Strahlungs-Emission und -Absorption nach der Quantentheorie
Verhandl. der Deutschen Physikalischen Gesellschaft **13/14**, 317 (1916).

[ein17] A. Einstein
Zur Quantentheorie der Strahlung
Phys. Z. **18**, 121 (1917).

[ell96] A. Ellens
Electron-phonon coupling of lanthanide ions in solids
Ph.D. thesis, Debye Institute, University of Utrecht (1996).

[ell97] A. Ellens, H. Andres, A. Meijerink and G. Blasse
Spectral-line-broadening study of the trivalent lanthanide-ion series I. Line broadening as a probe of the electron-phonon coupling strength
Phys. Rev. B **55**, 173 (1997).

[ell97b] A. Ellens, H. Andres, A. Meijerink and G. Blasse
Spectral-line-broadening study of the trivalent lanthanide-ion series. II. The variation of the electron-phonon coupling strength through the series
Phys. Rev. B **55**, 180 (1997).

[erd72] P. Erdös and J. H. Kang
Electronic Shielding of Pr^{3+} and Tm^{3+} in Crystals
Rhys. Rev. B **6**, 3393 (1972).

[fee01] FEE, Idar Oberstein, Germany.

[for69] H. Forest and G. Ban
Evidence for Eu^{+3} Emission from Two Symmetry Sites in Y_2O_3:Eu^{+3}
J. Electrochem. Soc. **116** (4), 474–478 (1969).

[for99] L. Fornasiero
Nd^{3+}- und Tm^{3+}-Dotierte Sesquioxide

Ph.D. thesis, Institute of Laser-Physics, University of Hamburg, Germany (1999).

[foe48]   T. Förster
            Zwischenmolekulare Energiewanderung und Fluoreszenz
            Annalen d. Phys. **2**, 55 (1948).

[fre62]   A. J. Freeman and R. E. Watson
            Theoretical Investigation of Some Magnetic and Spectroscopic Properties of Rare-Earth Ions
            Phys. Rev. **127**, 2058 (1962).

[gam00]   D. R. Gamelin, S. R. Lüthi and H. U. Güdel
            The role of Laser Heating in the Intrinsic Optical Bistability of Yb^{3+}-Doped Bromide Lattices
            J. Phys. Chem. B **104**, 11045–11057 (2000).

[gas70]   D. B. Gasson and B. Cockayne
            Oxide Crystal Growth using Gas Lasers
            J. Mat. Sci. **5**, 100–104 (1970).

[gie94]   A. Giesen et al.
            Scalable Concept for Diode-Pumped High-Power Solid-State Lasers
            Appl. Phys. B **58**, 365 (1994).

[gol97b]   P. Goldner, F. Pellé and F. Auzel
            Theoretical evaluation of cooperative luminescence rate in YB^{3+}:$CsCdBr_3$ and comparison with experiment
            J. Lumin. **72-74**, 901–903 (1997).

[gol97a]   P. Goldner, F. Pellé, D. Meichenin and F. Auzel
            Cooperative luminescence in ytterbium-doped $CsCdBr_3$
            J. Lumin. **71**, 137–150 (1997).

[goe96]   C. Görller-Walrand and K. Binnemans
            Rationalization of crystal-field parametrization
            In *Hanbbook on the Physics and Chemistry of Rare-Earths Vol. 23*, editor K. A. Gschneider Jr. and L. Eyring, North-Holland, Amsterdam, chapter 155, pages 121–283 (1996).

[gre87]   J. E. Greedan
            Rare Earth Elements and Materials
            In *Encyclopedia of Physical Science & Technology, Vol. 12*, editor R. A. Meyers, Academic Press Inc., Orlando, chapter 1, pages 18–39 (1987).

[gru85]   J. B. Gruber, R. P. Leavitt, C. A. Morrison and N. C. Chang
           Optical spectra, energy levels, and crystal-field analysis of tripositive
           rare earth ions in Y_2O_3. IV. C_{3i} sites
           J. Chem. Phys. **82** (12), 5373–5378 (1985).

[haj83]   J. Hajtó and I. Jánossy
           cited from gam00
           Philos. Mag. B **47**, 347 (1983).

[hak73]   H. Haken
           Quantenfeldtheorie des Festkörpers
           Teubner, Stuttgart (1973).

[heb76]   J. Heber
           The First and Second Nearest Neighbour Cr^{3+} Pairs in Ruby; I. Group
           Theoretical Treatment
           Z. Physik B **23**, 127–134 (1976).

[heb70]   J. Heber, K. H. Hellwege, U. Köbler and H. Murmann
           Energy Levels and Interaction between Eu^{3+}-ions at Lattice Sites of
           Symmetry C_2 and Symmetry C_{3i} in Y_2O_3
           Z. Physik **237**, 189–204 (1970).

[hee01]   S. Heer, M. Wermuth, K. Krämer and H. U. Güdel
           Upconversion excitation of Cr^{3+} ^2E emission in $Y_3Ga_5O_{12}$ codoped
           with Cr^{3+} and Yb^{3+}
           Chem. Phys. Lett. **334**, 293–297 (2001).

[heh93]   M. P. Hehlen and H. U. Güdel
           Optical spectroscopy of the dimer system $Cs_3Yb_2Br_9$
           J. Chem. Phys. **98** (1), 1768–1775 (1993).

[heh94]   M. P. Hehlen, H. U. Güdel, Q. Shu, J. Rai and S. C. Rand
           Cooperative Bistability in Dense, Excited Atomic Systems
           Phys. Rev. Lett. **73**, 1103 (1994).

[heh96]   M. P. Hehlen, H. U. Güdel, Q. Shu and S. C. Rand
           Cooperative optical bistability in the dimer system Cs_3Y-2Br_9:10%
           Yb^{3+}
           J. Chem. Phys. **104**, 1232 (1996).

[hei73]   W. Heitmann
           Reactively Evaporated Films of Scandia and Yttria
           Appl. Opt. **12**, 394 (1973).

[hen89]   B. Henderson and G. Imbusch
          Optical Spectroscopy of Inorganic Solids
          Clarendon Press, Oxford (1989).

[hen99]   F. Hentschel
          private communication
          Institute of Physical Chemistry, Univ. Hamburg (1999).

[her01]   Heraeus analysis of various Re powders (2001).

[her81]   C. C. Herrick and R. G. Behrens
          *Growth of large Uranite and Thoranite Single Crystals from the melt
          using a cold-crucible technique*
          J. Cryst. Growth **51**, 183 (1981).

[hoe66]   H. R. Hoekstra
          Phase Relationships in the Rare Earth Sesquioxides at High Pressure
          Inorg. Chem. **5**, 754 (1966).

[hoh99]   W. Hohenauer
          Ergebnisbericht zu Auftrag 26-99
          Seibersdorf, Austrian Research Centers (1999).

[hos64]   R. H. Hoskins and B. H. Soffer
          Stimulated Emission from Y_2O_3:Nd^{3+}
          Appl. Phys. Lett. **4** (1), 22 (1964).

[hur72]   J. P. Hurrel, Z. Kam and E. Cohen
          Theoretical Survey of the Sidebands of Sm^{2+} in BaF_2
          Phys. Rev. B **6**, 1999 (1972).

[hur68]   J. P. Hurrel, S. P. S. Porto, I. F. Chang, S. S. Mitra and R. P. Bauman
          Optical Phonons of Yttrium Aluminum Garnet
          Phys. Rev. **173**, 851 (1968).

[ign96]   I. V. Ignat'ev and V. V. Ovsyankin
          *Spectra of Electron-Vibrational f-f Transitions Tm^{2+}:CaF_2 and
          Tm^{2+}:SrF_2 Crystals*
          Opt. Spectroscopy **81**, 68 (1996).

[jor77]   C. K. Jørgensen and R. Reisfeld
          Lasers and Excited States of Rare Earths
          Springer, Berlin (1977).

[joh65]   L. F. Johnson, J. Geusic and L. van Uitert
          Coherent Oscillation from Tm^{3+}, Ho^{3+}, Yb^{3+} and Er^{3+} Ions in Yttrium Aluminum Garnet
          Appl. Phys. Let. **7**, 127 (1965).

[joh71]   L. F. Johnson and H. J. Guggenheim
          Infrared-Pumped Visible Laser
          Appl. Phys. Lett. **19** (2), 44–47 (1971).

[jud62]   B. Judd
          Optical absorption intensities of rare-earth ions
          Phys. Rev. **127**, 750 (1962).

[kam90]   A. A. Kaminskii
          Laser Crystals; Their Physics and Properties
          Springer Verlag, second edition (1990).

[kap62]   A. A. Kaplyanskii and P. P. Feofilov
          The spectra of divalent rare earth ions in crystals of alkaline earth fluorides
          Opt. Spect. **13**, 129 (1962).

[kis69]   P. Kisliuk, N. C. Chang, P. L. Scott and M. H. L. Pryce
          Energy levels of Chromium Ion Pairs in Ruby
          Phys. Rev. **184** (2), 367–374 (1969).

[kit83]   C. Kittel
          Einführung in die Festkörperphysik
          R. Oldenbourg Verlag, München, Wien, 6$^{\text{th}}$ edition (1983).

[kiz96]   P. Kizler, J. He, D. R. Clarke and P. R. Kenway
          Structural Relaxation around Substitutional Cr^{3+} Ions in Sapphire
          J. Am. Ceram. Soc. **79**, 3–11 (1996).

[kle67]   P. H. Klein and W. J. Croft
          Thermal Conductivity, Diffusivity, and Expansion of Y_2O_3, $Y_3Al_5O_{12}$, and LaF_3 in the Range $77°$-$300°K$
          J. Appl. Phys **38** (4), 1603–1607 (1967).

[koe71]   U. Köbler
          Optical Spectra of Eu^{3+} Ion Pairs in Y_2O_3
          Z. Physik **247**, 211 (1971).

[koe00]   S. Koelling
          Untersuchungsbericht ILP 6-2000
          Technical University Hamburg-Harburg (2000).

[kon65]   J. A. Konigstein
          Energy Levels and Crystal-Field Calculations of Trivalent Ytterbium Aluminum Garnet and Yttrium Gallium Garnet
          Teoret. Chim. Acta (Berl.) **3**, 271 (1965).

[kue92]   G. Künzler, B. Müller and W. Tews
          The Dependence of UV Stability of Y_2O_3-Eu^{3+}-Phosphors on the Composition
          Phys. Stat. Sol. A **130**, K279 – K283 (1992).

[kus69]   T. Kushida
          Linewidths and Thermal Shifts of Spectral Lines in Neodymium-Doped Yttrium Aluminum Garnet and Calcium Fluorophosphate
          Phys. Rev. **185**, 500 (1969).

[kus67]   T. Kushida and M. Kikuchi
          R, R', and B Absorption and Phonon-Induced Relaxations in Ruby
          J. Phys. Soc. Japan **23**, 1333 (1967).

[lak99]   LAKRIMAT project report (BMBF project no. 13N6749-2) (1999).

[lea82]   R. P. Leavitt, J. B. Gruber, N. C. Chang and C. A. Morrison
          Optical spectra, energy levels, and crystal-field analysis of tripositive rare earth ions in Y_2O_3. II. Non-Kramers ions in C_2 sites
          J. Chem. Phys. **76** (10), 4775–4788 (1982).

[lef62]   R. A. Lefever
          Flame Fusion Growth of C-Type Rare-Earth Oxides
          Rev. Sci. Instr. **33**, 1470 (1962).

[lis98]   K. Lisak and W. Hohenauer
          Thermophysikalische Charakterisierung von Y_2O_3, Sc_2O_3, Lu_2O_3, Yb(3%):Lu_2O_3 und Nd(0,5%):Lu_2O_3; Ergebnisbericht zu Auftrag 81-98
          Seibersdorf, Austrian Research Centers (1998).

[lis98b] K. Lisak and W. Hohenauer
          Thermophysikalische Charakterisierung von YAG Kristallen; Ergebnisbericht zu Auftrag 86;87-98
          Seibersdorf, Austrian Research Centers (1998).

[loh69]   E. Loh
          *Ultraviolet-absorption spectra of europium and ytterbium in alkaline
          earth fluorides*
          Phys. Rev. **84** (2), 184 (1969).

[lup99]   A. Lupei, V. Lupei, C. Presura, V. N. Enaki and A. Petraru
          *Electron-phonon coupling effects on Yb^{3+} spectra in several laser crys-
          tals*
          J. Phys. Condens. Matter **11**, 3769–3778 (1999).

[lup97]   Luptn, Schielke, Weigelt, Petermann, Fornasiero, Mix
          Deutsche Patentanmeldung Nr.: 197024653 (1997).

[mal95]   O. L. Malta
          The Theory of Vibronic Transitions in Rare Earth Compounds
          J. Phys Chem. Solids **56**, 1053 (1995).

[man63]   M. Mandel
          Paramagnetic resonance of Yb^{3+} in yttrium oxide
          Appl. Phys. Lett. **2** (10), 197–198 (1963).

[mcc64]   D. E. McCumber
          *Einstein relations connecting broadband emission and absorption spec-
          tra*
          Pys. Rev. **136** (4A), 954 (1964).

[mcc63]   D. E. McCumber and M. D. Sturge
          Linewidth and Temperature Shift of the R Lines in Ruby
          J. Appl. Phys. **34** (6), 1682–1684 (1963).

[mcd66]   N. T. McDevitt and A. D. Davidson
          *Infrared Lattice Spectra of Cubic Rare Earth Oxides in the Region 700
          to 50 cm^{-1}*
          J. of the Opt. Soc. of America **56** (5), 636–638 (1966).

[mcm68]   W. R. McMahon and D. R. Wilder
          Hemispherical Spectral Emittance of Selcted Rare Earth Oxides
          J. of The Am. Cer. Soc. **51** (4), 187–192 (1968).

[mes90]   A. Messiah
          Quantenmechanik, volume 2
          Walter de Gruyter & Co., Berlin, third edition (1990).

[mix95]   E. Mix
          *Spektroskopie und Lasereigenschaften ytterbiumdotierter Kristalle und
          Fluorid-Phosphat-Gläser*
          Master's thesis, Institute of Laser-Physics, University of Hamburg, Ger-
          many (1995).

[mix99]   E. Mix
          *Kristallzüchtung, Spektroskopie und Lasereigenschaften Yb-dotierter
          Sesquioxide*
          Ph.D. thesis, Institute of Laser-Physics, University of Hamburg, Ger-
          many (1999).

[moh00]   J. Mohr
          Lasereigenschaften und Spektroskopie Holmium-dotierter Sesquioxide
          Master's thesis, Institute of Laser-Physics, University of Hamburg, Ger-
          many (2000).

[moo68]   R. M. Moon, W. C. Koehler, H. R. Child and L. J. Raubenheimer
          Magnetic Structures of Er_2O_3 and Yb_2O_3
          Phys. Rev. **176** (2), 722–731 (1968).

[moo70]   H. W. Moos
          Spectroscopic relaxation processes of rare earth ions in crystals
          J. Lumin. **1 and 2**, 106 (1970).

[mor65]   A. H. Morrish
          The Physical Principles of Magnetism
          John Wiley & Sons, Inc., New York (1965).

[mue01]   V. Müller
          *Charakterisierung und Optimierung von hochdotierten Yb:YAG
          Laserkristallen*
          Master's thesis, Institute of Laser-Physics, University of Hamburg, Ger-
          many (2001).

[nak70]   E. Nakazawa and S. Shionoya
          Cooperative Luminescence in $YbPO_4$
          Phys. Rev. Lett. **25** (25), 1710–1712 (1970).

[nig67]   Y. Nigara
          Measurement of the Optical Constants of Yttrium Oxide
          Japanese J. Appl. Phys. **7** (4), 404–408 (1968).

[nor96]   Northern Analytical Laboratory, Inc. analysis of 5N Sc_2O_3 Boulder Scientific Company batch # BSC-5549 (1996).

[ofe62]   G. Ofelt
Intensities of crystal spectra of rare-earth ions
J. Chem. Phys. **37**, 511 (1962).

[oka94]   Y. Okano, Y. Tsuji, D. H. Yoon, K. Hoshikawa and T. Fukuda
Internal radiative heat transfer in Czochralski growth of LiTaO_3 single crystal
J. Crys. Growth **141**, 383–388 (1994).

[ovs87]   V. V. Ovsyankin
Spectroscopy of Collective States and Cooperative Transitions in Disordered Rare-Earth Activated Solids
In *Spectroscopy of Solids Containing Rare Earth Ions*, editor A. A. Kaplyanskii and R. M. Macfarlane, Elsevier Science Publishers B. V., chapter 7, pages 343–480 (1987).

[pau30]   L. Pauling and M. D. Shappell
The Crystal Structure of Bixbyite and the C-Modification of the Sesquioxides
Zeitschr. f. Kristallographie **75**, 128–142 (1930).

[pay92]   S. A. Payne, L. L. Chase, L. K. Smith, W. L. Kway and W. F. Krupke
Infrared Cross-Section Measurements for Crystals Doped with Er^{3+}, Tm^{3+} and Ho^{3+}
IEEE J. of Quant. Electr. **28** (11), 2619 (1992).

[pet98]   V. Peters
Spektroskopie und Lasereigenschaften Erbium- und Praseodymdotierter Hochschmelzender Oxide
Master's thesis, Institute of Laser-Physics, University of Hamburg, Germany (1998).

[pie00]   L. van Pieterson, M. Heeroma, E. de Heer and A. Meijerink
Charge Transfer Luminescence of Yb^{3+}
J. Lumin. **91**, 177–193 (2000).

[pie74]   E. Pietsch, editor
Gmelins Handbuch der Anorganischen Chemie, volume Seltenerdelemente Teil C1
Springer Verlag, Berlin, Heidelberg, New York, 8th edition (1974).

[pir67]   R. K. Pirinchieva
          Absorption and emission spectra of Er^{3+} in Sc_2O_3
          Opt. Spektrosk. **23**, 96–101 (1967).

[pla76]   W. Platz and J. Heber
          The First and second Nearest Neighbour Cr^{3+} Pairs in Ruby; II. Spectra
          and Energy Levels of the First Nearest Neighbours
          z. Physik B **24**, 333–341 (1976).

[ray63]   D. K. Ray
          Investigations into the Origin of the Crystalline Electric Field Effects on
          Rare Earth Ions; II. Contributions from the Rare Earth Orbitals
          Proc. Phys. Soc. **82**, 47–57 (1963).

[rei77]   R. Reisfeld and C. K. Jørgensen
          Lasers and Excited States of Rare Earths
          Inorganic Chemistry Concepts. Springer-Verlag (1977).

[rek99]   S. Rekhi, L. D. Dubrovinsky and S. K. Saxena
          Temperature- induced ruby fluorescence shifts up to a pressure of
          15GPA in an externally heated diamond anvil cell
          High Temperatures - High Pressures **31**, 299–305 (1999).

[roe92]   Römpp
          Chemielexikon
          Falbe, Regitz (publ.), Thieme Verlag, Stuttgart, 9th edition (1992).

[rot60]   R. S. Roth and S. J. Schneider
          Phase Equilibria in Systems Involving the Rare-Earth Oxides
          J. Research NBS **64A**, 309 (1960).

[sch70]   F. Schmid and D. Viechnicki
          Growth of Sapphire Disks from the Melt by a Gradient Furnace Technique
          J. of The Am. Cer. Soc. **53** (9), 528–529 (1970).

[sch70b] G. Schnaack and J. A. Konigstein
          Phonon and Electron Raman Spectra of Cubic Rare-Earth Oxides and
          Isomorphous Ytrrium Oxide
          J. Opt. Soc. Am. **60**, 1110 (1970).

[sch75]   H. J. Schugar, E. I. Solomon, W. L. Cleveland and L. Goodman
          Simultaneous Pair Electronic Transitions in Yb_2O_3
          J. Am. Chem. Soc. **97** (22), 6442–6450 (1975).

[sil01]   Silicon-Strategies online magazine
          http://www.siliconstrategies.com/story/OEG20000410S0002.

[sob79]   I. I. Sobelman
          Atomic Spectra and Radiative Transitions
          Springer-Verlag, Berlin (1979).

[sta99]   Stanford Materials Corporation analysis of 5N Sc_2O_3 batch # OX21-5N
          AB00117/991007 (1999).

[ste66]   R. M. Sternheimer
          Shielding and Antishielding Effects for Various Ions and Atomic Systems
          Phys. Rev. **146** (1), 140–160 (1966).

[sum94]   D. S. Sumida and T. Y. Fan
          *Effect of radiation trapping an fluorescence lifetime and emission cross
          section measurements in solid-state laser media*
          Opt. Lett. **19** (17), 1343–1345 (1994).

[sve93]   O. Svelto
          Priciples of Lasers
          Plenum Press, New York, third edition (1989).

[szo93]   A. Szöke
          *Holographic Methods in X-ray Crystallography. II. Detailed Theory and
          Connection to Other Methods of Crystallography*
          Acta Crystallographica A **49**, 853–866 (1993).

[szo97]   A. Szöke
          Holographic Microscopy with a Complicated Reference
          Journal of Imaging Science and Technology **41** (4), 332–341 (1997).

[tip66]   H. Tippins
          Absorption Edge Spectrum of Scandium Oxide
          J. Phys. Chem. Solids **27**, 1069–1071 (1966).

[tro01]   T. Tröster
          Optical studies of non-metallic compounds under pressure
          In *Handbook on the Physics and Chemistry of Rare Earths*, editor K. A.
          Gschneider Jr. and J.-C. G. Bünzli, North-Holland, Amsterdam, vol-
          ume 33 (2001, to be published).

[val00]   R. Valiente, O. Wenger and H. U. Güdel
          New photon upconversion processes in Yb^{3+} doped $CsMnCl_3$ and

RbMnCl$_3$
Chem. Phys. Lett. **320**, 639–644 (2000).

[var61]   F. Varsanyi and G. H. Dieke
Ion-pair resonance mechanism of energy transfer in rare earth crystal fluorescence
Phys. Rev. Lett. **7**, 442–443 (1961).

[vie74]   D. Viechnicki and F. Schmid
Crystal growth using the Heat Exchanger Method (HEM)
J. of Crystal Growth **26**, 162–164 (1974).

[vle37]   J. H. van Vleck
The Puzzle of Rare Earth Spectra in Solids
J. Phys. Chem. **41**, 67 (1937).

[vor82]   Y. K. Voron'ko, V. V. Osiko and I. A. Shcherbakov
Luminescence of Laser Crystals
Izvestiya Akademii Nuak SSR. Seria Fizicheskaya **46** (5), 970–978 (1982).

[web82]   M. J. Weber
Lasers and Masers
In *CRC Handbook of Laser Science and Technology, Volume 1*, CRC Press Inc., Boca Raton, Florida (1982).

[wes92]   G. A. West and N. S. Clements
A Comparison of the Eu^{3+} Temperature Dependent Emission Lifetimes in Sc$_2$O$_3$, Y$_2$O$_3$, and Gd$_2$O$_3$ Host Crystals
J. Lumin. **54**, 245–248 (1992).

[wil88]   K. T. Wilke and J.Bohm
Kristallzüchtung
Verlag Harry Deutsch, Thun, Frankfurt a. M., second edition (1988).

[win81]   G. Winkler
Magnetic Garnets
F. Veiweg & Sohn Verlagsgesellschaft mbH, Braunschweig (1980).

[woo63]   D. L. Wood
Energy Levels of Yb^{3+} in Garnets
J. Chem. Phys. **39**, 1671 (1963).

[yen64]   W. M. Yen, W. C. Scott and A. L. Schawlow
           Phonon-Induced Relaxation in Excited Optical States of Trivalent
           Praseodymium in LaF$_3$
           Phys. Rev. **136**, A271 (1964).

[yok67]   M. Yokota and O. Tanimoto
           cited from [bur72]
           J. Phys. Soc. Japan **22**, 779 (1967).

[zac28]   W. Zachariasen
           Über die Kristallstruktur von Bixbyit, sowie vom künstlichen Mn$_2$O$_3$
           Z. Krist. **67**, 455 (1928).

[zie71]   J. P. van der Ziel
           Optical Spectrum of Cr^{3+} Pairs in LaAlO$_3$
           Phys. Rev. B **4** (9), 2888–2905 (1971).

[zie69]   J. P. van der Ziel and L. G. van Uitert
           Magnon-Assisted Optical Emission in YCrO$_3$ and LuCrO$_3$
           Phys. Rev. **179** (2), 343–351 (1969).

Publications

Publications in Journals

L. Fornasiero, E. Mix, V. Peters, K. Petermann, and G. Huber
New Oxide Crystals for Solid State Lasers
Crystal Research and Technology **34** 2, pp. 255-260, (1999)

V. Peters, E. Mix, L. Fornasiero, K. Petermann, S. A. Basun, and G. Huber
Efficient laser operation of $Yb^{3+}:Sc_2O_3$ and spectroscopic characterization of Pr^{3+} in cubic sesquioxides
Laser Physics **10** No. 2, pp. 417-421, (2000)

K. Petermann, G. Huber, L. Fornasiero, S. Kuch, E. Mix, V. Peters, and S. A. Basun
Rare earth doped sesquioxides
Journal of Luminescence **87-89**, pp.973-975, (2000)

L. Fornasiero, E. Mix, V. Peters, K. Petermann, and G. Huber
Czochralski growth and laser parameters of RE^{3+}-doped Y_2O_3 and Sc_2O_3
Ceramics International **26**, pp. 589-592, (2000)

K. Petermann, L. Fornasiero, E. Mix, and V. Peters
High melting Sesquioxides: Crystal growth, Spectroscopy, and Laser Experiments
Optical Materials, to be published, (2001)

V. Peters, A. Bolz, K. Petermann, and G. Huber
Growth of High-melting Sesquioxides by the Heat Exchanger Method
J. of Crystal Growth, to be published, (2001)

International Conference Contributions

L. Fornasiero, E. Mix, V. Peters, K. Petermann and G. Huber
Czochralski Growth and Laser Parameters of RE^{3+}-doped Y_2O_3 and Sc_2O_3
Proceedings of the 9th Int. Conference on Modern Materials & Technologies, Florence, Italy, oral presentation, (1998)

E. Mix, L. Fornasiero, V. Peters, K. Petermann and G. Huber
High Temperature Czochralski Growth of Yttrium Oxide and Scandium Oxide
Proceedings of the 12th Int. Conference on Crystal Growth, Jerusalem, Israel, poster presentation, (1998)

V. Peters, L. Fornasiero, E. Mix, A. Diening, K. Petermann and G. Huber
Spectroscopic Characterization and Diode-Pumped Laser Action at 2.7μm of Er:Lu$_2$O$_3$
Proceedings CLEO-Europe, Glasgow, United Kingdom, technical digest CFF10, (1998)

L. Fornasiero, E. Mix, V. Peters, E. Heumann, K. Petermann, and G. Huber
Efficient laser operation of Nd:Sc$_2$O$_3$ at 966nm, 1082nm, and 1486nm
Conference on Advanced Solid-State Lasers, Boston, USA, technical digest pp. 88-90, (1999)

L. Fornasiero, N. Berner, B.-M. Dicks, E. Mix, V. Peters, K. Petermann, and G.Huber
Broadly tunable laser emission from Tm:Y$_2$O$_3$ and Tm:Sc$_2$O$_3$ at 2μm
Conference on Advanced Solid-State Lasers, Boston, USA, technical digest pp. 390-392, (1999)

V. Peters, E. Mix, L. Fornasiero, K. Petermann, S. A. Basun, and G. Huber
Efficient laser operation of Yb^{3+}:Sc$_2$O$_3$ and spectroscopic characterization of Pr^{3+} in cubic sesquioxides
8th International Laser Physics Workshop, Budapest, Hungary, technical digest 4.20, (1999)

K. Petermann, G. Huber, E. Mix, V. Peters, and S. A. Basun
Rare earth doped sesquioxides
International Conference on Luminescence and Optical Spectroscopy of Condensed Matter, Osaka, Japan, technical digest B04-6, (1999)

K. Petermann, L. Fornasiero, E. Mix,and V. Peters
High-melting sesquioxides: Crystal growth, spectroscopy, and laser experiments
Proceedings of the 2nd International Symposium on Laser, Scintillator and Non-linear Optical Materials, Lyon, France, oral presentation, (2000)

M. A. Noginov, G. B. Loutts, C. Steward, B. Lucas, D. Fider, V. Peters, G. Huber, and C. M. Bowden
Spectroscopic study of Yb doped oxide crystals for intrinsic optical bistability
Conference on Nonlinear Optics: Materials, Fundamentals, and Applications, Kaua'i-Lihue, USA, oral presentation, technical digest OSA TOPS Vol. 46 p. 405, (2000)

G. Huber, V. Peters, and K. Petermann
New Solid-State Lasers Based on Rare-Earth Doped Sesquioxides
Conference on Lasers and Electro-Optics Europe, Nice, France, invited paper, technical digest CFH3, (2000)

V. Peters, E. Mix, K. Petermann, G. Huber, and M. A. Noginov
Identification of Electronic Stark-Levels in Yb^{3+}-Doped Sesquioxides by Pair Spectroscopy
Conference on Lasers and Electro-Optics Europe, Nice, France, technical digest CFH5, (2000)

M. Larionov, A. Giesen, K. Contag, V. Peters, E. Mix, L. Fornasiero, K. Petermann, and G. Huber
Thin Disk Laser Operation and Spectroscopic Characterization of Yb-doped Sesquioxides
Conference on Advanced Solid-State Lasers, Seattle, USA, technical digest pp. 405-407, (2001)

V. Peters, A. Bolz, K. Petermann, and G. Huber
Growth of High Melting Sesquioxides by the Heat Exchanger Method
13[th]International Conference on Crystal Growth, Kyoto, Japan, technical digest 31p-S12-16, (2001)

K. Petermann, V. Peters, and A. Bolz
Growth Methods for High-Melting Sesquioxides
French-German Crystal Growth Meeting, Seeheim-Jugenheim, oral presentation, (2001)

V. Peters, K. Petermann, A. Bolz, G. Huber, K. Contag, M. Larionov, and A. Giesen
Ytterbium-doped sesquioxides as host materials for high-power laser applications
Conference on Lasers and Electro-Optics Europe, Munich, Germany, technical digest #213, (2001)

National Conference Contributions

V. Peters, L. Fornasiero, E. Mix, A. Diening und K. Petermann
Spektroskopie und Lasereigenschaften von Yb^{3+}- und Er^{3+}-dotiertem Sc_2O_3
Verhandl. DPG (IV) **33**, Frühjahrstagung Konstanz, oral presentation Q41.4, (1998)

V. Peters, L. Fornasiero, E. Mix, K. Petermann, and G. Huber
Effiziente Lasertätigkeit in $Nd:Sc_2O_3$ und $Yb:Sc_2O_3$
Verhandl. DPG (IV) **34**, 63. Physikertagung Heidelberg, oral presentation Q31.3, (1999)

V. Peters, E. Mix, L. Fornasiero, K. Petermann, and G. Huber
Spektroskopische Untersuchungen an Yb^{3+}-dotierten Sesquioxiden unter hohen Drücken
Verhandl. DPG (IV) **35**, Frühjahrstagung Bonn, poster presentation Q40.1, (2000)

A. Bolz, V. Peters, K. Petermann, and G. Huber
Energy transfer in Yb^{3+}-doped Sesquioxides
Verhandl. DPG (IV) **36**, Frühjahrstagung Berlin, poster presentation Q31.16, (2001)

J. Mohr, M. Mond, V. Peters, E. Heumann, K. Petermann, and G. Huber
Spectroscopy and continous wave lasing of $Yb,Ho:Sc_2O_3$ and $Tm,Ho:Sc_2O_3$ at 2.1μm
Verhandl. DPG (IV) **36**, Frühjahrstagung Berlin, oral presentation Q33.4, (2001)

V. Müller, A. Bolz, V. Peters, and K. Petermann
Spektroskopische Untersuchungen und Optimierung der Kristallqualität von hochdotierten Yb:YAG Laserkristallen
Verhandl. DPG (IV) **36**, Frühjahrstagung Berlin, oral presentation Q33.5, (2001)

Meetings, Seminars, Summer Schools

V. Peters
Spektroskopie und Lasereigenschaften Er^{3+}- und Pr^{3+}-dotierter hochschmelzender Oxide
Seminar über Festkörperlaser, Hamburg, oral presentation, (1998)

V. Peters
Comparison of spectroscopic properties of erbium in yttria, scandia, and lutetia
NATO Advanced Study Institute 52nd SUSSP Summer School in "Advances in Lasers and Applications", St. Andrews, United Kingdom, poster presentation (1998)

V. Peters, L. Fornasiero, E. Mix, K. Petermann, and G. Huber
Kristallzüchtung hochschmelzender Oxide
Arbeitskreistagung DGKK "Kristalle für Laser und Nichtlineare Optik", Köln, oral presentation, (1999)

E. Mix, L. Fornasiero, V. Peters, K. Petermann, and G. Huber
$Yb:Lu_2O_3$ - Ein neues Lasermaterial mit hoher Wärmeleitfähigkeit
10. Norddeutscher Lasertag, Hamburg, poster presentation, (1999)

V. Peters
Sesquioxides as efficient laser host materials
1st Workshop of the Graduiertenkolleg "Felder und lokalisierte Atome - Atome und lokalisierte Felder", Travemünde, oral presentation, (1999)

V. Peters
Spektroskopie Yb3+-dotierter Sesquioxide
Seminar über Festkörperlaser, Hamburg, oral presentation, (2000)

V. Peters
Spectroscopy of Ytterbium-doped sesquioxides
2nd Workshop of the Graduiertenkolleg "Felder und lokalisierte Atome - Atome und lokalisierte Felder", Schwerin, oral presentation, (2000)

A. Bolz, V. Peters, and K. Petermann
Energietransfer in Yb-dotierten Kristallen
11. Norddeutscher Lasertag, Hannover, poster presentation, (2000)

Curriculum Vitae

Personal Data

Date of Birth:	September 8th, 1973
Place of Birth:	Hamburg, Germany
Nationality:	German

Education and Qualifications

Mar. 1999 - Sep. 2001	Ph.D. studies at the Institute of Laser-Physics, University of Hamburg, Germany on the growth and spectroscopy of ytterbium-doped sesquioxides funded by a scholarship from the Deutsche Forschungsgemeinschaft (German Science Community) under the supervision of Prof. Dr. G. Huber
Sep. 1998	Attending the summer-school SUSSP52 "Advances in Lasers and Applications" at the University of St. Andrews, UK
Jun. 1997 - Aug. 1998	Diploma thesis at the Institute of Laser-Physics, University of Hamburg, Germany on growth and laser characteristics of erbium- and praseodymium-doped sesquioxides
Oct. 1993 - Feb. 1999	Physics studies, University of Hamburg, Germany. Minors: economics, computer-science. Qualification obtained: Diplom-Physiker (MSc equivalent)
1992 - 1993	Supervision of the computer-science-workgroup for the 11th grade of the Gymnasium im Schulzentrum Henstedt-Ulzburg
1990 - 1991	High School for the Engineering Professions, Houston, Texas, USA
1984 - 1990 and 1991 - 1993	Gymnasium im Schulzentrum Henstedt-Ulzburg, Germany (grammar school equivalent). Sets in mathematics and physics, qualification obtained: Abitur (A-levels equivalent).

Acknowledgements

... the entire Festkörperlaser-group for the outstanding working climate and all the work and non-work related discussions.

... the technical staff of the group "F", Günter Roschewski, Robert Fischer, Silke Frömmig, and Renate Seiffert, for their help with all kinds of problems.

... Dr. Peter Rogin for his support in enhancing the crystal growth control software.

... Peter Kappen for his time consuming, though unfortunately unsuccessful, attempt to get a usable measurement of the ligand relaxation around a dopant ion.

... Silke Kölling for the chemical analysis of various crystals.

... Barbara Cornelisen for the microprobe measurements.

... Frank Hentschel for performing the Raman measurements.

... last but not least my friends and family for their constant support outside of work, which helped me a lot in finishing this thesis.